Ionic Liquids

in a Multiscale Study

Dissertation

zur Erlangung des Grades
"Doktor der Naturwissenschaften"
im Promotionsfach Chemie

am Fachbereich Chemie, Pharmazie und Geowissenschaften
der Johannes Gutenberg-Universität in Mainz

Katharina Wendler geb. Scholze
geb. in Dresden

Mainz, den 31. Januar 2012

Tag der mündlichen Prüfung:

Mainz, den 26. März 2012

Erstbetreuer:	Professor Dr. K. Kremer
Zweitbetreuer:	Professor Dr. J. Gauß

D77 Dissertation an der Johannes Gutenberg-Universität Mainz

I hate reality but it's still the best place to get a good steak.

Woody Allen

List of publications

Parts of this thesis are published:

1. K. Wendler, S. Zahn, F. Dommert, R. Berger, C. Holm, B. Kirchner and L. Delle Site
   Locality and Fluctuations: Trends in imidazolium-based Ionic Liquids and beyond
   J. Chem. Theory Comput. **7**, *2011*, 3040–3044 (Letter).

2. K. Wendler, F. Dommert, Y. Y. Zhao, R. Berger, C. Holm and L. Delle Site
   Ionic liquids studied across different scales: A computational perspective
   Faraday Discuss. **154**, *2012*, 111–132.

3. S. Zahn, K. Wendler, L. Delle Site and B. Kirchner
   Depolarization of water in protic ionic liquids
   Phys. Chem. Chem. Phys. **13**, *2011*, 15083–15093.

4. N. V. Pogodina, E. Metwalli, P. Müller-Buschbaum, K. Wendler, R. Lungwitz, S. Spange, J. L. Shamshina, R. D. Rogers, and C. Friedrich
   Peculiar Behavior of Azolium Azolate Energetic Ionic Liquids
   J. Phys. Chem. Lett. **2**, *2011*, 2571–2576.

5. F. Dommert, K. Wendler, R. Berger, L. Delle Site, and C. Holm
   Force fields for studying structure and dynamics of ionic liquids – a critical review of recent developments
   ChemPhysChem, DOI: 10.1002/cphc.201100997.

6. K. Wendler, M. Brehm, F. Malberg, B. Kirchner, and L. Delle Site
   Short time dynamics of ionic liquids studied by AIMD based powerspectra
   submitted.

Contents

Abstract

Despite the overwhelming interest in ionic liquids, a rational design and application of them is hindered by a lack of fundamental understanding. Classical molecular dynamics provide a powerful tool for studying the underlying molecular mechanisms, but the quality of available force fields is still too low for a generally reliable description.
Hence in this thesis, the balance of molecular interactions in ionic liquids is characterized in order to understand the properties of ionic liquids and to help a rational force field design within the multiscale approach. Therefore, several neat imidazolium ionic liquids, mixtures with small solutes, and a protic ionic liquid were studied by *ab-initio* methods. This *ab-initio* molecular dynamics study of their liquid phases is unique in its width and allows for new systematic insight. Furthermore, liquid phase properties were compared to those of ion pairs, both in their ground state structures and at temperatures above 0 K. Special focus is on the molecular electrostatic properties as they are of high influence on the quality of classical force fields and can be studied explicitly only by *ab-initio* methods.
It emerged in this work that the Coulomb interaction played a key role and led to unique characteristics of the molecular electrostatic properties for all ionic liquids studied. In general, the ion net charges were found to be reduced, the molecular dipole moment distributions were very broad. Further, the electrostatic properties were demonstrated to be local on the molecular size scale and, as a consequence, on the few picosecond time scale. On this local scale, electronic polarization was shown to be decisive for the molecular electronic structure. The electrostatic properties of the ions were found to be highly sensitive to the phase state and its composition, *i.e.* the presence of small solute molecules.
The chemical specificity, *e.g.* the likeliness to form dispersive contacts or hydrogen bonds, was shown to have a crucial influence on the ionic liquids' fine structures. At temperatures around 400 K, the cation anion orientation was demonstrated to be influenced more strongly by hydrogen bonding than by dispersion. Longer alkyl sidechains, in contrast, tended to interact *via* dispersion which led to a segregation of the sidechains.
The interactions' balance was also studied in terms of power spectra based on *ab-initio* molecular dynamics simulations of the liquid phase. These were demonstrated to offer a new way for comparison to experiment and an insight into the fast dynamics inherently linked to electronic effects. For instance, the hydrogen bond strength could be evaluated by observed wavenumbers shifts.

Zusammenfassung

Trotz des hohen Interesse an Ionischen Flüssigkeiten wird das zielgerichtete Design und die Anwendung Ionischer Flüssigkeiten durch fehlendes grundlegendes Verständnis erschwert. Prinzipiell können die molekularen Mechanismen mit klassischer Molekulardynamik beschrieben werden, aber die Qualität der vorhandenen Kraftfelder reicht noch nicht für eine allgemein zuverlässige Beschreibung aus.
Deshalb wird in dieser Arbeit die Balance der molekularen Wechselwirkungen in Ionischen Flüssigkeiten studiert, um die Eigenschaften dieser zu verstehen und die Kraftfeldentwicklung im Rahmen des Multiskalenansatzes zu systematisieren. Es wurden reine Imidazolium-basierte Ionische Flüssigkeiten, Mischungen mit kleinen Molekülen und eine protische Ionische Flüssigkeit mit *ab-initio* Methoden untersucht. Somit ist diese *ab-initio* Molekulardynamikstudie einzigartig in ihrer Breite und erlaubt neue systematische Einblicke. Weiterhin wurden Eigenschaften der Flüssigphase mit denen von Ionenpaaren sowohl im Grundzustand als auch bei Temperaturen über 0 K verglichen. Im Fokus stehen die molekularen elektrostatischen Eigenschaften, weil diese großen Einfluss auf die Genauigkeit von Kraftfeldern haben und explizit nur mit *ab-initio* Methoden beschrieben werden können.
Es wurde in dieser Arbeit gezeigt, dass Coulomb-Wechselwirkungen eine Schlüsselrolle einnahmen und zu einzigartigen Charakteristika der molekularen Eigenschaften Ionischer Flüssigkeiten führten. So waren die Ionen-Nettoladungen stets reduziert, die molekularen Dipolmomentverteilungen sehr breit. Die elektrostatischen Eigenschaften waren allgemein lokal auf einer molekularen Größenskala und als Folge auch auf einer Zeitskala von wenigen Pikosekunden, wobei die elektronische Polarisation entscheidend für die elektronische Struktur war. Die elektrostatischen Eigenschaften der Ionen hingen stark vom Phasenzustand und seiner Zusammensetzung, zum Beispiel der Anwesenheit kleiner gelöster Moleküle, ab.
Für andere molekulare Eigenschaften, wie die Neigung zu dispersiven Kontakten oder Wasserstoffbrücken, wurde gezeigt, dass sie einen entscheidenden Einfluss auf die Feinstruktur Ionischer Flüssigkeiten hatten. Bei Temperaturen um 400 K wurde die Kation-Anion-Ausrichtung stärker von Wasserstoffbrücken als von Dispersion bestimmt. Dahingegen wechselwirkten längere Alkylseitenketten eher dispersiv.
Das Gleichgewicht der Wechselwirkungen zeigte sich auch in Leistungsspektren, die sich aus *ab-initio* Molekulardynamiksimulationen der Flüssigphase ergaben. Diese boten einen neuen Weg für den Vergleich zum Experiment und für einen Einblick in die schnelle Dynamik Ionischer Flüssigkeiten, die inhärent mit elektronischen Effekten verbunden ist. Zum Beispiel konnte die Wasserstoffbrückenstärke durch Wellenzahlverschiebungen bewertet werden.

Chapter 1

Introduction

Ionic liquids (ILs) have sparked widespread interest due to their peculiar properties and the resulting possibility of manifold applications. [1,2] In the future development, a profound understanding of the ruling principles in ILs will be advantageous. It is the scope of this work to further clarify the balance of molecular interactions. In the following, ILs will be introduced shortly in Chapter 1.1. Especially, the present interactions (see Chapter 1.2) and the recent state of atomistic theoretical approaches will be discussed (see Chapter 1.3).

1.1 Ionic liquids

ILs are defined as low melting salts with a melting point below 100 °C. Those which melt below room temperature are distinguished as room temperature ILs and are of special interest in applications. For instance, they offer tailor-made high-potential solutions in chemical reactions as catalysts, [3, 4] or in separation processes due to their adaptable solubility and very low vapor pressure. [5] As they consist of ions and have rather large electrochemical windows, they are tested as electrolytes in *e.g.* fuel cells. [6] Moreover, ILs dissolve cellulose and permit to reshape and process the most abundant organic raw material using less energy and chemicals and increasing the process' sustainability. [7] The very low vapor pressure of ILs minimizes also the risk of atmospheric pollution by ILs and adds to the operational safety of a given process. [5]
Chemically, ILs are designed by combining two ions. The ions on which the here studied ILs are based are given in Figure 1.1: the cations 1,3-dimethylimidazolium (MMIM), 1-ethyl-3-methylimidazolium (EMIM), 1-butyl-3-methylimidazolium (BMIM), and monomethyl ammonium (MMA) and the anions chloride (Cl), thiocyanate (SCN), dicyanamide (DCA), tetrafluoroborate (BF_4), 5-aminotetrazolate (5AT), 4-nitroimidazolate (4NI), and nitrate (NO_3). Each of the ions can be varied independently, *e.g* the cations by substituting linear alkyl chains with functionalized, branched, or aromatic units. In this sense, the number of possible ILs is huge. [5] As a consequence, ILs can have very diverse properties and might even be immiscible. For instance, EMIM DCA is significantly less viscous than EMIM Cl or EMIM SCN. As a low viscosity is desirable in many applications, EMIM DCA is a promising IL. BMIM 5AT and BMIM 4NI

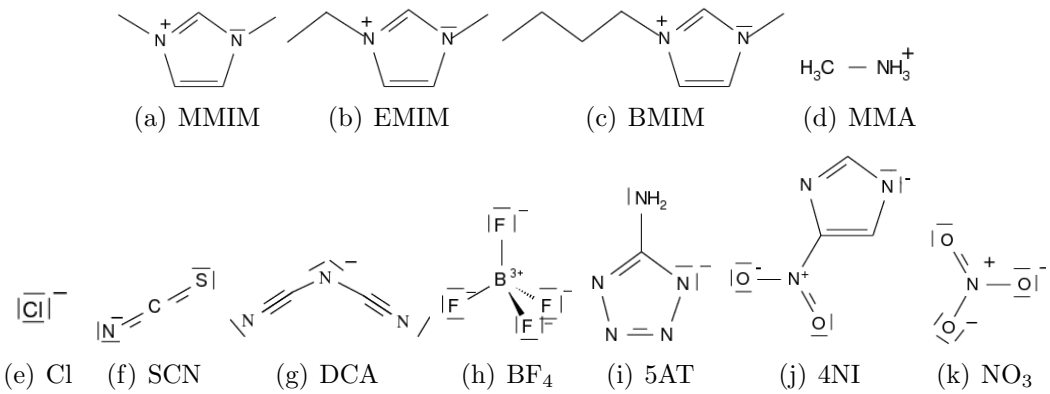

Figure 1.1: Schematic presentation of one mesomeric Lewis structure of the ions on which the here considered ionic liquids are based: (a) to (d) cations and (e) to (k) anions.

are so-called energetic ILs and may be of use as fuels.
The properties of a specific IL can hardly be predicted due to the IL's complex behavior. ILs are suggested to behave as supercooled liquids close to their glass transition [4, 8–11] Indeed, dynamical heterogeneity is observed in ILs by different experimental techniques as dielectric relaxation spectroscopy, [12] optical Kerr effect studies, [13] and rheology [9, 10] as well as in simulations. [8, 14–19] Furthermore, evidence for microstructures was found by rheology and small angle X-ray scattering (SAXS). [10] Hence, the liquid phase of ILs seems rather heterogeneous in structure and dynamics and this needs to be better understood for the development of a predictive model.

1.2 Interactions in ionic liquids

The physical and chemical properties of any substance depend on the balance of the molecular interactions, their relative strength and their directionality. For instance, the molecules may or may not participate in hydrogen bonds. Such preferred conformations or orientations are often connected to some partial charge transport. Certain parts of the molecules might gain or loose electron density and, thus, become activated for reactions. For instance, a high acidity might be favorable in some catalytic reactions whereas it needs to be avoided in others. If the balance of the molecular interactions is understood, ILs can be designed such that certain interactions are strengthened or weakened to fit the requirements of an application. Similarly, in any model, the effect of these molecular interactions has to be reproduced as the model will fail otherwise. Thus, a principal understanding of the interactions' balance is crucial for any model, no matter if it is a classical force field or an equation of state. In this sense, fundamental theoretical studies are particularly needed for the interpretation and prediction of experimental results. [1, 20–25]
In ILs, the different physical and chemical interactions have been identified with

Coulomb [26–29] and Van der Waals interactions [26, 30–33] as well as hydrogen bonds. [32–42] Coulomb interactions are strong and long-ranged whereas Van der Waals forces and hydrogen bonds are short-ranged and weaker. On the one side, the Coulomb interactions dominate in simple salts like sodium chloride in which Van der Waals interactions are negligible in comparison. In many simple salts, ions are monoatomic and do not possess any internal vibrational or rotational degrees of freedom and entropy plays a minor role. On the other side, neutral molecular solvents, as *e.g.* water, are characterized by a certain balance between Van der Waals forces and hydrogen bonding. In ILs, all three kinds of interactions play a crucial role and this might be the reason for their unique properties and for the difficulties in developing force fields which can describe this subtle balance.
Experimentally, the influence of these interactions was discussed in Refs. [4,40,43–47]. For instance, a microsegregation in polar and apolar domains was proposed if the ions were composed of polar and apolar parts, *e.g.* polar imidazolium rings and apolar alkyl sidechains of imidazolium cations. This means that the anions and imidazolium rings were close together in a domain dominated by Coulomb interactions and hydrogen bonding. In this, the role and character of hydrogen bonding is still discussed. [18,32,41,42,48,49] Meanwhile, sidechains longer than the propyl sidechain clustered together interacting *via* dispersion. If small molecules are solvated in such ILs, they could be found in either polar or apolar domains [50] or at the boundaries between both, depending on their own polarity. In this way, ILs might dissolve a broader range of solutes than conventional solvents. To evaluate the solvation process and the IL's polarity, probe molecules are dissolved in the ILs and their ultraviolett-visible (UV-vis), electron paramagnetic resonance (EPR), nuclear magnetic resonance (NMR), or infrared (IR) spectra is studied. Depending on the kind and strength of interactions, the signals in the spectra will be shifted. For UV-vis, appropriate solvatochromic probes allow the determination of the Kamlet-Taft parameters which characterize the hydrogen bond donating ability (α), the hydrogen bond accepting ability (β) and the dipolarity or polarizability (π^*). Around the probe molecules, the IL structure equilibrates. Depending on its properties, the probe might either be surrounded by anions or cations, by polar or apolar domains. That might explain the partially contradicting results on Kamlet-Taft parameters with different probes. [4] In general, ILs were found to have rather similar Kamlet-Taft parameters as short chain alcohols. A different measure for the polarity, the dielectric constant, finds ILs to be rather apolar with dielectric constants between 10 and 20. The apparent discrepancy, not found for molecular solvents, can be explained by a time scale separation of processes. [4] The measurements of the dielectric constant are carried out at finite frequencies as ILs are conductive. As a consequence, the standard measurements give a short-circuit and the zero frequency dielectric constant can be obtained only by extrapolation. [12, 51] At finite frequencies, however, a full reordering and equilibration of the IL's structure is not possible, only the dipole moments can relax at these frequencies. As the molecules are rather bulky, the number of ions, *i.e.* dipole moments, per volume is low. The dipole moment density is approximately about one seventh compared to the one of water and, so is the dielectric constant. [52] Hence, for ILs, certain concepts, developed for molecular solvents, seem not easily transferable. Due to the many processes on different time and length scales, ILs appear to have a high complexity.

1.3 Theoretical studies of ionic liquids

A powerful theoretical tool of study, at molecular as well as statistical thermodynamical level, is computer simulation. Especially, classical molecular dynamics (MD) simulations have the potential to allow for a basic molecular understanding of the dynamical processes and yet describe the essential overall behavior as a liquid. The numerous MD studies, [8, 15, 19, 34, 39, 53–74] however, were restricted to few specific ILs due to the lack of reliable, transferable force fields. Moreover, many force fields in current literature have problems in reproducing experimental data for both dynamic and static properties. [25, 57, 75] As the quality of the force fields determines the accuracy of the MD studies, the force field development is the most challenging aspect in the MD approach to ILs at the moment. Mostly, force fields are based on reference data of isolated ions' ground states and, thus, might fail to describe the cooperativity of the bulk phase. To compensate for this, the parameters were often fitted to further experimental data. [59] A more systematic approach is the multiscale approach (see Chapter 2.6) which intends to transfer information from one scale to the next consistently.
In the process of the parametrization of a classical force field setup, *ab-initio* studies are mostly employed in order to obtain atomic partial charges. However, since these are not physical observables, the assignment of charges to atomic species depends strongly on the assignment schemes which should be chosen with particular care. For instance, whereas force fields with natural population analysis (NPA) [76, 77] or restrained electrostatic potential (RESP) [78] based partial charges described a similar spacial ordering of the ions in the bulk phase, a force field based on partial charges assigned with the shared electron number (SEN) method [79–81] gave completely different spacial distributions. [74] Typically, criteria of assignment of charges based on fitting the electrostatic potential as RESP or CHELPG [82] are employed. These methods, however, cannot be applied to the bulk phase. By employing the Blöchl method to the bulk phase [38, 83, 84], the effective charges were found to differ from those for isolated ions or ion pairs. Regarding this difference, the study of the electronic structure of the bulk phase seems needed for the force field development. As a technique for electronic structure calculations, the density functional theory (DFT) approach represents a suitable compromise between accuracy and efficiency, at least for systems in the liquid phase. In general, DFT proved to be a valuable tool in treating complex molecular liquids and solutions, [85–87] even though DFT suffers from two limitations due to the approximations in the exchange-correlation functional (see also Chapter 2.2).

In general, DFT can give unphysical charge transfer due to the delocalization, or self-interaction, error [93] leading to artifacts in the molecular electrostatic properties. Hence, the DFT data should be compared to post Hartree-Fock reference data. In fact, while ionic dipole moments were consistent between DFT and MP2, [94] MP2 gave ion net charges whose absolute values were also reduced, but about 12 % higher than those of DFT. MP2 is a common computational compromise for including electron correlations and the MP2 results were found to be within 2 % of the more accurate coupled cluster approach with single and double excitations (CCSD) benchmark data [38, 83, 84] and, thus, to be rather trustworthy. However, similar partial charges as that of MP2 were obtained by using hybrid functionals such as BHandHLYP [83]

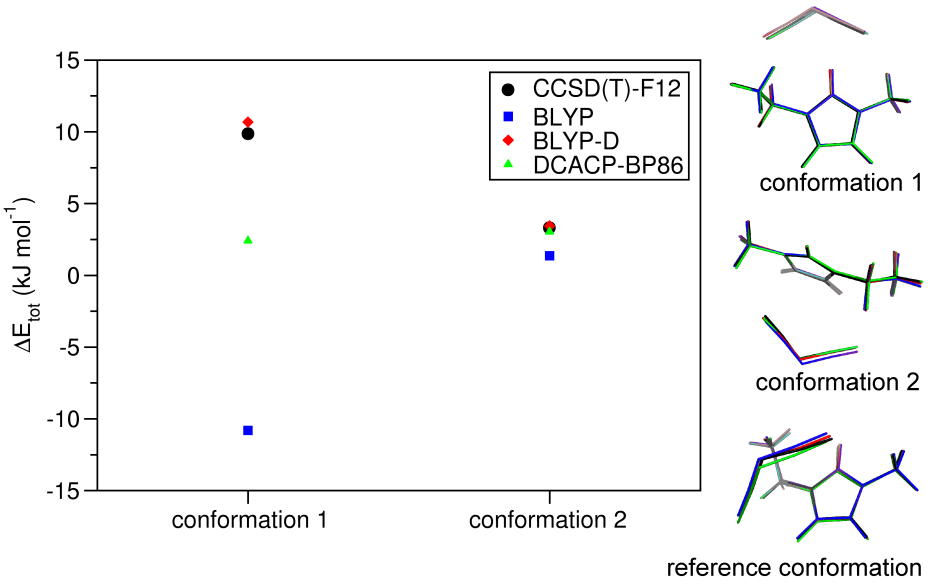

Figure 1.2: Relative total energies (in kJ/mol) of two EMIM DCA ion pair conformations with respect to the more stable reference conformation regarding the total CCSD(T)-F12/aug-cc-pVDZ energy (based on a MP2/TZVPP optimized structure) as well as by BLYP, BLYP-D, and $BP86_{DCACP}$ with a plane wave basis set with a kinetic energy cutoff of 35 E_h which are typical setups in CPMD AIMD simulations. In the inset, the optimized structures are compared: MP2 (black), BLYP (blue), BLYP-D (red), DCACP-BP86 (green).
The CCSD(T)-F12 energies [88] were calculated with Molpro (2008.1), [89] the MP2 geometry optimization [90] was conducted with TURBOMOLE [91], the DFT calculations were done with CPMD. [92]

suggesting that the use of hybrid density functionals might be advantageous in partial charge assignment.
Another intrinsic limitation of the DFT approach is the lack of accuracy in describing dispersion interactions. Still, a reasonable agreement was found between DFT and post Hartree-Fock methods as MP2 [94–103] and to coupled cluster approach with single, double, and perturbative triple excitations CCSD(T) benchmark data [97, 104, 105], even though DFT often gave the wrong energetic order of ion pair conformations. Mostly, the ion pair binding energies, relative total energies or equilibrium distances of isolated ion pairs were compared between DFT and MP2. The hybrid Becke three parameter Lee Yang Parr functional [106] B3LYP was shown to be unreliable for ILs [90, 96, 97, 102, 104, 107] as it gave the wrong energetic order of ion pair conformations compared to MP2 as well. [96, 102, 107] In general, hybrid functionals did not perform much better than generalized gradient-corrected functionals (GGA) as the Perdew Burke Ernzerhof one (PBE) [90]. They were affected by the same limitation of semilocality in the context of reproducing dispersion interactions. [108]
Only the inclusion of a dispersion correction was reported to enable a reliable DFT de-

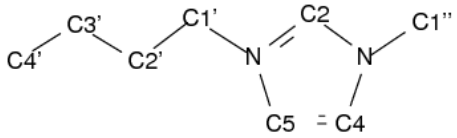

Figure 1.3: Nomenclature of the carbon atoms in imidazolium ions for the example of BMIM.

scription of ion pairs in the gas phase [90,104]. For instance, the equilibrium interionic distances of an ion pair or that of ion pairs were shifted significantly below the electrostatic equilibrium distance by induction and dispersion. [30, 31] Furthermore, the dispersion component of the ion pair binding energy correlated well with conductivity and viscosity of several ILs, [109] showing the importance of dispersion. In general, setups as the Becke Lee Yang Parr [110, 111] functional with Grimme dispersion correction [112–114] BLYP-D or the Becke Perdew functional [110, 115] with DCACP pseudopotentials [116, 117] $BP86_{DCACP}$ were identified as reliable, giving the correct energetic order of ion pair conformations (for details to the dispersion corrections see Chapter 2.2). Additionally, non-empirical functionals describing Van der Waals interactions have been found to improve the prediction of *e.g.* crystal volumes. [118]
Still, the best performing DFT setup depends on the specific ionic liquid system. In fact, BLYP-D failed in predicting ion pair binding energies for Cl or BF_4 based ion pairs accurately. [104] However, it performed well for ion pairs with larger anions as DCA or bis(trifluoromethylsulfonyl)imide in which dispersion was more decisive. [104] For illustration, one example of three EMIM DCA ion pair ground state conformations is given in Figure 1.2. The conformations obtained with the three functionals and MP2 differed mainly in the interionic orientation whereas the cation structure was nearly exactly the same for all setups. In the stacked conformations, computational setups which included dispersion gave a slightly lower interionic distance. While the conformational variations were small, the energy ordering was qualitatively different. BLYP predicted conformation 1 to be more stable than the reference conformation, but the two dispersion corrected DFT setups found the reference conformation to be the most stable consistent with MP2 and CCSD(T)-F12. As a conclusion, dispersion-corrected functionals are in principle capable of a reliable description, but a systematic comparison to post Hartree-Fock reference data seems mandatory to identify an adequate DFT setup for a specific IL.
In order to improve the force field predictive power, AIMD simulations of the bulk phase are almost a necessary tool to provide data for a robust parametrization as the bulk properties differ from the ones of the gas phase. Several AIMD simulations have been presented in literature, for instance of neat imidazolium based ILs, [34,37,107,119–123] mixtures with water [124,125], and mixtures with $AlCl_3$ [126] as well as of ammonium based ILs. [33, 73, 125] In the NVT ensemble, the density functional dependence of radial distribution functions was small for dimethylimidazolium chloride MMIM Cl (compare [34, 107, 119–121]). However, in isobaric-isothermal simulations, in which the density was not restricted to the experimental one, the obtained density was influenced by the specific functional used. [73, 108] Recently, DFT setups with dispersion corrections, BLYP-D [this work] or DCACP-

BP86, [33, 125] have been applied as they were shown to improve the description of gas phase ion pairs. In general, the structural properties found in AIMD were different from the ones in classical molecular dynamics. In the former, the cation cation stacking was more likely and the hydrogen bond at the imidazolium C^2H hydrogen (see Figure 1.3) was stronger than in the latter. [34, 107, 122] Crucially for force field development, the electrostatic properties of the ions were different from the ones in the gas phase. [38, 83, 84, 120] Thus, AIMD simulations of the bulk phase rather than static ion pair calculations should be considered in the force field development.

1.4 Outline

Ab-initio methods allow the study of small systems without any system specific parametrization. In this way, the ruling principles of the molecular interactions and their balance can be elucidated. This understanding helps *e.g.* in the design of ILs in a way optimized for a specific application or in the study of reaction mechanisms, but also for classical MD studies. In this spirit, this work is focused on the discussion of these molecular interactions and their balance in a molecular scale. First, the results of the often examined reference state, the ground state structures of isolated ion pairs, will be discussed and compared to isolated ion pairs at finite temperature (see Chapter 3). Second, the impact of Coulomb interaction will be studied in the bulk liquid phase and it will be shown how the strong Coulomb interactions led to common properties of the ILs (see Chapter 4). Third, the influence of more local and directional interactions, as hydrogen bonding or dispersion, will be discussed (see Chapter 5). Further, power spectra will be introduced as a possibility to study the short time dynamics of ILs in Chapter 5.

Chapter 2

Methodology

A valuable insight into the molecular interactions can be gained if the electronic scale is described explicitly. For instance, the formation and breakage of bonds and mutual polarization effects can occur. Also, no *a-priori* assumptions about the specific interactions of the molecules are needed. The most common electronic structure methods are density functional theory (DFT) and quantum chemical approaches as Hartree-Fock (HF) or post Hartree-Fock (post HF) methods. Whereas the accuracy or computational demand of these methods differs, they all give approximations to the solution of the time independent electronic Schrödinger equation of many-body systems:

$$\hat{H}\psi(\underline{\mathbf{r}}) = E\psi(\underline{\mathbf{r}}) \tag{2.1}$$

$$\hat{H} = \hat{T} + \hat{V}_{\text{el,el}} + \hat{V}_{\text{nuc,el}} \tag{2.2}$$

$$= -\sum_{i=1}^{n} \frac{\triangle_i}{2} + \sum_{i=1}^{n}\sum_{j\geq i}^{n} \frac{1}{|\mathbf{r_i} - \mathbf{r_j}|} - \sum_{I=1}^{N}\sum_{i=1}^{n} \frac{1}{|\mathbf{R_I} - \mathbf{r_i}|} \tag{2.3}$$

in which n is the number of electrons, N number of nuclei, $\mathbf{r_i}$ position of the i-th electron, $\mathbf{R_I}$ position of the I-th nucleus, $\hat{T}$ kinetic energy operator of the electrons, $\hat{V}_{\text{el,el}}$ potential energy operator of the electron electron repulsion, and $\hat{V}_{\text{nuc,el}}$ potential energy operator of the nuclei electron attraction. Mostly and also in this work, several approximations are applied: In the context of the Born-Oppenheimer approximation, [127] the atoms are treated classically. Also, relativistic effects are neglected completely. Further, the basis set is composed of a finite number of orthogonal functions and, hence, the complete, infinite, basis set is truncated. Additionally, the wavefunctions are assumed to be products of one-electron wavefunctions and the effect of electron correlation is considered in different extent by the applied methods. In general, two kinds of electron correlation are distinguished: Coulomb correlation and Fermi (or exchange) correlation. The Coulomb correlation is based on the mutual repulsion of electrons which decreases with the reciprocal distance between two electrons. The Fermi correlation is due to the indistinguishability of the electrons and the antisymmetry of Fermionic wavefunctions. Whereas all HF based quantum chemical methods include the Fermi correlation due to the construction of Slater determinants, the original HF formalism neglects the Coulomb correlation completely. In so-called

post HF methods, this correlation is included in different ways, mostly implicitly by considering more than one determinant. For DFT, both types of correlations have to be included implicitly by choosing an appropriate approximate functional. [128–131]

2.1 Post Hartree-Fock methods

The Coulomb correlation energy is typically less than 1 % of the total energy. However, it is higher than chemical reaction energies and, hence, decisive. In the following, two post Hartree-Fock (post HF) methods used within this work are shortly introduced. More details are given in *e.g.* [128, 132, 133].
In an application of the Rayleigh-Schrödinger perturbation theory, the correlation is treated as perturbation in the Møller-Plesset perturbation theory which is mostly considered in second order (MP2):

$$\hat{H} = \hat{H}_0 + \lambda \hat{H}' \tag{2.4}$$

$$\hat{H}_0 = \sum_{i=1}^{n} \hat{f}(i) \tag{2.5}$$

$$\hat{H}' = \sum_{i=1}^{n} \sum_{j \geq i}^{n} \frac{1}{|\mathbf{r_i} - \mathbf{r_j}|} - \sum_{i=1}^{n} \sum_{j \geq i}^{n} [\hat{j}_j(i) - \hat{k}_j(i)] \,. \tag{2.6}$$

The unperturbed Hamiltonian $\hat{H}_0$ is chosen as the sum the one-electron Fock operators $\hat{f}(i)$ and the perturbed Hamiltonian $\hat{H}'$ gives the difference between the true interelectronic repulsions and an average potential, the Hartree-Fock interelectronic potential, consisting of the Coulomb integrals $\hat{j}_j(i)$ and the exchange integrals $\hat{k}_j(i)$. The sum of the zeroth- and first-order MP2 energies is the Hartree-Fock energy. The second-order energy correction $E^{(2)}$ gives a first contribution of the correlation effects:

$$E^{(2)} = \sum_{s \neq 0}^{n} \frac{|\langle \Phi_0^{(0)} | \hat{H}' | \Phi_s^{(0)} \rangle|^2}{E_0^{(0)} - E_s^{(0)}} \tag{2.7}$$

in which $\Phi_0^{(0)}$ is the Hartree-Fock determinant and $\Phi_s^{(0)}$ is an unperturbed Slater determinant. Such an unperturbed Slater determinant Φ_{ij}^{ab} contains electrons in virtual orbitals unoccupied in the HF determinant. For instance, two electrons can change from orbitals i and j, occupied in the HF determinant, to orbitals a and b, unoccupied in the HF determinant. This is denoted as double excitation. According to the Slater-Condon rules, only these doubly excited determinants give an non-zero contribution in the integral for $E^{(2)}$ and the MP2 correlation correction is:

$$E^{(2)} = \sum_{b=a+1}^{\infty} \sum_{a=n+1}^{\infty} \sum_{i=j+1}^{n} \sum_{j=1}^{n-1} \frac{|\langle ab|r_{12}^{-1}|ij\rangle - \langle ab|r_{12}^{-1}|ji\rangle|^2}{\varepsilon_i + \varepsilon_j - \varepsilon_a - \varepsilon_b} \,. \tag{2.8}$$

in which ε_i is the orbital energy of orbital i. In general, MP2 leads to a qualitative improvement compared to HF without immense computational effort as it captures

most of the correlation energy.
A different approach is the coupled cluster theory in which an exponential ansatz is chosen for the wavefunction:

$$|\psi\rangle = e^{\hat{T}}|\Phi_0\rangle\,. \tag{2.9}$$

$\hat{T}$ is an excitation operator that produces a linear combination of excited Slater determinants of all possible excitations of electrons from occupied to virtual orbitals. Φ_0 is a Slater determinant and, commonly, the Hartree Fock one. If $\hat{T}$ is truncated after the second term: $\hat{T} = \hat{T}_1 + \hat{T}_2$, the method is called coupled cluster with single and double excitations (CCSD) as $\hat{T}_1$ is the operator for single excitations and $\hat{T}_2$ for double excitations. Due to the exponential form of the operator

$$e^{\hat{T}} = 1 + \hat{T} + \frac{\hat{T}^2}{2} + \cdots = 1 + \hat{T}_1 + \hat{T}_2 + \frac{\hat{T}_1^2}{2} + \hat{T}_1\hat{T}_2 + \frac{\hat{T}_2^2}{2} + \cdots\,, \tag{2.10}$$

the wavefunction contains also determinants with higher excitations as *e.g.* quadruple substitutions which are the most important after double substitutions. [128] Even though the treatment of these higher excitations is only approximate, their contribution is captured in a good manner. Often, CCSD with a perturbative treatment of triple excitations (CCSD(T)) is used as it is more accurate than CCSD, but the computational effort is significantly less than for CCSDT. Coupled-cluster methods are generally the preferred choice if highly accurate results are needed. [134]

2.2 Density Functional Theory

Density functional theory is another very popular approach in *ab-initio* studies. Its advantage is that the density depends only on three coordinates in contrast to the electronic wavefunction depending on $3n$ degrees of freedom in which n is the number of electrons. It is based on the two Hohenberg-Kohn theorems. [135] The first theorem states that the external potential and, thus, the ground state properties of a many-electron system are uniquely determined within a trivial additive constant by the electron density $\rho(r)$. The constrained Levy-Lieb search [136–138] which includes the minimum energy requirement leads to the fact that any density corresponds exactly to one wavefunction. The second theorem states that for any trial density $\tilde{\rho}(r)$ such that $\tilde{\rho}(r) \geq 0$ and $\int \tilde{\rho}(r)dr = n$, the ground state energy is larger or equal to the true ground state energy: $E_0 \leq E_v[\tilde{\rho}]$. Unfortunately, the energy functional is not yet known even though certain components can be assigned or approximated. Kohn and Sham [139] introduced the following partitioning:

$$E_v[\rho] = T_s[\rho] + V_{\mathrm{el,el}}[\rho] + E_{\mathrm{xc}}[\rho] + \int V_{\mathrm{ext}}\rho(r)dr \tag{2.11}$$

in which $T_s[\rho] = T_s[\{\phi_i[\rho]\}]$ is the kinetic energy function of the non-interacting, non-uniform electron system with a density $\rho(r)$ and the one-electron orbitals ϕ_i, $V_{\mathrm{el,el}}$ is the Hartree energy of non-interacting electrons, V_{ext} is the external potential given by *e.g.* the nuclei, and E_{xc} is the exchange correlation functional. Basically, the

density $\rho(r)$ of an interacting many-electron system in the potential V_{ext} can be determined by solving the Kohn-Sham equation of a fictitious one-electron system in an effective potential $V_s = \frac{\partial V_{\text{el,el}}[\rho]}{\partial \rho} + \frac{\partial E_{\text{xc}}[\rho]}{\partial \rho} + V_{\text{ext}}$. The exchange correlation functional E_{xc} shall describe both the exchange correlation and the Coulomb correlation of interacting electrons, but a general form is unknown. While several approximation exist, it is still subject of intense research. To increase the accuracy of the calculated exchange correlation energy, the functional E_{xc} might be changed from one $E_{\text{xc}}[\rho]$ with a local-density approximation (LDA) [140] to one $E_{\text{xc}}[\rho, \bigtriangledown\rho]$ with a generalized gradient approximation (GGA) [129] or one $E_{\text{xc}}[\rho, \bigtriangledown\rho, \bigtriangledown^2\rho]$ with a meta-GGA to so-called hybrid functionals which include the exact Hartree-Fock exchange to a certain extent. [106, 141, 142]
Due to the approximations in the exchange correlation functionals, a spurious electronic self-interaction occurs and dispersion cannot be described by standard DFT. Typically, the self-interaction error [143] manifests itself in significant underestimation of electronic band gaps and an over-delocalization of electronic states. The latter is most evident in systems with an odd number of electrons or with significant contribution from strongly localized states. The ILs studied within this work consist of main group elements, mainly carbon, nitrogen, and hydrogen, and the ions have an even number of electrons. Thus, artificial delocalization due the self-interaction error can be expected to affect charge distribution over the ions uniformly, yielding the accurate topology of the electron density. In order to describe dispersion, several approaches are established as specific functionals or empirical corrections. Within this work, two empirical dispersion corrections were used: The Grimme dispersion correction [112–114] describes the dispersive energy by damped interatomic potentials of the form $C_6\, R^{-6}$. As a consequence, the electron density is not changed by this correction, but the energies and forces. The dispersion-corrected atom-center potentials DCACP [144] consist of optimized nonlocal higher angular momentum dependent terms and give a changed electron density. DCACP increase the computational cost more than the Grimme dispersion correction, but give a different electron density than the standard pseudopotentials and likely different partial charges.
For computational efficiency, plane wave basis sets rather than atom-centered localized ones are often used as they allow for solving the eigenvalue equation *via* a Fast Fourier transform and their representation is independent of the ionic positions of the nuclei. Also, they do not exhibit basis set superposition errors. The accuracy of the plane wave basis $\psi_i(r) = \sum_G c_{i,G} e^{\mathrm{i}Gr}$ of electron i is determined solely by $G = k + g$ in which k is the vector in the Brillouin zone and g the vector of the Fourier space. For computational capability, the plane wave basis sets is mostly truncated at an energy cutoff in the kinetic energy of $E_{\text{kin}} = \frac{1}{2}|G|^2 \leq E_{\text{cutoff}}$. In *ab-initio* molecular dynamics, only the Γ point at which $k = (0, 0, 0)$ is considered [145] and, thus, the wavefunction is real. However, the electron density of an atomic core cannot be represented by a reasonable amount of plane waves. That is why pseudopotentials are introduced which describe the nucleus and the inner shell electrons. For most functionals and atoms, pseudopotentials were derived and are available.

2.3 Wavefunction localization schemes

In general, the electron density is distributed continuously over the whole system and a sophisticated analysis has to be conducted in order to assign local electronic properties to an atom or a molecule. Such an analysis can be done in various ways, leading to different results. In this work, several methods were used and are introduced shortly in the following.

2.3.1 Maximally localized Wannier functions

The Wannier functions [146–148] are an alternative representation of (plane wave) basis sets and can be obtained from these by unitary transformations. Although the Wannier functions are non-unique in principle, a protocol to obtain well defined functions has been introduced. [149] The resulting functions are called "maximally localized" Wannier functions and are those used in this work. Within this localization algorithm, the second moment of the Wannier functions around their centers is minimized. The charge center of a maximally localized Wannier function corresponds to the classical location of an electron pair. [150] Hence, it can provide an insight into the chemical bond structure [150] as well as it sheds light on the local polarization. For instance, molecular electric dipole moments can be calculated based on the nuclei charges and the Wannier centers (see *e.g.* [151] for water). For this, the Wannier centers are assigned to the closest nuclei and its molecule and each molecule has an integer net charge.

2.3.2 Bader charge analysis

The Bader criterion [152] is based on topological partitioning of the electron density ρ into atomic volumes. These volumes are determined by the separatrix surfaces $\vec{\bigtriangledown}\rho \cdot \vec{n} = 0$ in which $\vec{n}$ is the normal vector to the surface. This means that the flux of the gradient of the electron density through the interatomic surfaces vanishes at any point of the surface. [153] In this way, the surfaces divide the space in distinct volumes, each of them being assigned to an atom or to a molecule. Such, the topological defined charge of an subunit can be evaluated. [154] The approach is also known as atoms in molecules. [152]

2.3.3 Blöchl charge assignment method

In the Blöchl approach, [155] it is assumed that the interaction between separated charge densities can be expressed entirely through their multipole moments. It can be shown that the electrostatic interactions can be treated efficiently in the reciprocal representation for systems with periodic boundary conditions. Thus, the fitting in the Blöchl method is done in reciprocal space in contrast to common electrostatic potential fitting procedures like RESP or CHELPG in which the fitting is carried out in real space. Fitting in real space demands to exclude regions close the atoms. The

Blöchl approach being performed in the reciprocal space does not suffer from this problem and, hence, can be easily applied to bulk systems. The Blöchl method fits charge densities by projecting it on atom-centered Gaussians and, so, describes the effective charge of an ion. Hence, the net charge of ions might deviate from the integer value. If the electric dipole moment shall be calculated by using partial charges of Blöchl, the charge of the ion might be rescaled to the integer value. Otherwise, there is a prefactor in the electric dipole formula if compared to the Wannier electric dipole moment which describes ions with integer charges. This can be done by dividing each Blöchl partial charge by the net charge of the ion. The so-obtained partial charge set gives an ion net charge of $\pm$ 1 e and is denoted here as rescaled Blöchl charges.

2.3.4 Natural population analysis and natural bond orbitals

The natural based population analysis (NPA) is based on natural atomic orbitals which are localized one-center orbitals of an atom A in the molecular environment. The natural atomic charge q_A of the atom A given by NPA is:

$$q_A = Z_A - \sum_{k=1}^{K} p_k^{(A)} \tag{2.12}$$

in which Z_A is the nuclear charge of atom A, $p_k^{(A)}$ is the population of orbital k, and K is the number of orbitals localized at atom A. In contrast to the similar Mulliken analysis, [156] natural populations satisfy the physical restriction for closed shells: $0 \leq p_k^{(A)} \leq 2$.
In the natural bond orbital (NBO) approach, the electron density is contracted into the few-centers orbitals with an occupation number close to two which are called Lewis-type NBO. [157, 158]. In order to calculate properties like the energy of a donor–acceptor interaction, off-diagonal elements of the Fock matrix are used to perturb the natural bond orbitals. All possible interactions between filled Lewis-type NBO and empty non-Lewis-type NBO are examined and their energetic importance E_2 is estimated by second-order perturbation theory:

$$E_2 = \Delta E_{\mathrm{ij}} = q_{\mathrm{i}} \frac{F(\mathrm{i},\mathrm{j})^2}{\epsilon_{\mathrm{j}} - \epsilon_{\mathrm{i}}} \,. \tag{2.13}$$

q_{i} is the donor orbital occupancy, ϵ_{i} and ϵ_{j} are diagonal elements of the Fock matrix and, thus, orbital energies, and $F(\mathrm{i},\mathrm{j})$ is the off-diagonal NBO Fock matrix element. [159] These interactions lead to loss of occupancy from the localized NBO of the idealized Lewis structure into the empty orbitals, they are referred to as delocalization corrections to the zeroth-order natural Lewis structure. [76, 159]

2.3.5 Shared electron number

Qualitatively, bond strengths are often associated with the number of bond electrons in a Lewis structure. The charge-density analysis by Davidson [79], Roby [160], and

Heinzmann and Ahlrichs [161] defines a two-center shared electron number (SEN) which provides a quantitative measure for the strength of a covalent bond. [161, 162] The two-center SEN is defined as: [161]

$$\sigma = N_{\mathrm{A}} + N_{\mathrm{B}} - N_{\mathrm{AB}} \quad . \tag{2.14}$$

N_{X} is the occupation number of atom X and N_{AB} is the atom pair occupation with

$$N_{\mathrm{X}} = trDP_{\mathrm{X}} \qquad P_{\mathrm{X}} = \sum_{\nu} |\varphi_\nu\rangle\langle\varphi_\nu| \tag{2.15}$$

$$N_{\mathrm{AB}} = trDP_{\mathrm{AB}} \qquad P_{\mathrm{AB}} = \sum_{\nu,\mu} |\varphi_\nu\rangle(S^{-1}_{\nu,\mu})\langle\varphi_\mu| \tag{2.16}$$

in which D is the molecular one-electron density operator, P the projector onto the space of occupied self-consistent-field atomic orbitals and φ_ν are the atomic orbitals of a certain atom A.
Reiher, Sellmann, and Hess [163] firstly applied the SEN approach to intermolecular, non-covalent hydrogen bonds. They found a linear relationship:

$$E_\sigma = a\sigma \tag{2.17}$$

in which E_σ is the hydrogen bond energy and σ is the two-center SEN. The SEN approach was applied for many different systems [102,163–167]. Later, a new parametrization allowing for an intercept as well as donor and acceptor atom specific parameters was introduced [165] and extended. [168] The SEN was demonstrated to be a rather reliable single descriptor for the detection and evaluation of hydrogen bonds in the ground state structures.

2.4 Car-Parrinello molecular dynamics

In molecular dynamics (MD) simulations, particles are moved normally according to Newton's laws and, thus, the forces acting on them. On the *ab-initio* molecular dynamics (AIMD) scale, the forces acting on the nuclei, modeled as classical particles, are calculated based on Kohn-Sham DFT by

$$F_I = - \bigtriangledown_{R_I} \left[E_\upsilon[\{\phi_i[\rho]\}] + V_{\mathrm{nuc,nuc}}(\underline{R})\right] \tag{2.18}$$

in which $E_\upsilon[\rho]$ is the Kohn-Sham energy functional (see Chapter 2.2) and $V_{\mathrm{nuc,nuc}}$ is the Coulomb potential of the nucleus nucleus repulsion. In Born-Oppenheimer MD, the electron density is optimized at any time step to describe the electronic ground structure as the Born-Oppenheimer approximation assumes that the electronic structure equilibrates instantaneously if the nuclei positions change. Born-Oppenheimer MD is very tedious due to the high number of necessary minimization steps in the electronic ground state calculation. Thus, Car and Parrinello proposed to treat the electron wave functions $\phi_i(r,t)$ as classical particles whose dynamics should be similar

to the ones of the nuclei. [169] The resulting extended Lagrangian is:

$$\mathcal{L}_{\mathrm{CP}}(\{\phi_i\},\{\dot{\phi}_i\},\underline{R},\underline{\dot{R}}) = \frac{1}{2}\sum_{I=1}^{N} M_I \dot{R}_I^2 + \frac{1}{2}\sum_{i=1}^{n} \mu\langle\dot{\phi}_i|\dot{\phi}_i\rangle - E_v[\{\phi_i\},\underline{R}]+ \tag{2.19}$$

$$+\sum_{i,j}\Lambda_{ij}(\langle\phi_i|\phi_i\rangle - \delta_{ij})\,. \tag{2.20}$$

Therein, μ is the fictitious mass assigned to the $\{\phi_i(r,t)\}$ treated as classical particles, M_I is the mass of the nucleus I. Hence, the first two terms describe the kinetic energies of the nuclei and the electrons. The last term guarantees the orthonormality of the wavefunctions. The Euler-Lagrange formalism gives the following equations of motions:

$$M_I\ddot{R}_I = -\frac{\partial E_v[\{\phi_i\},\underline{R}]}{\partial R_I} + \sum_{i,j}\Lambda_{ij}\frac{\partial}{\partial R_I}\langle\phi_i|\phi_i\rangle \tag{2.21}$$

$$\mu\,|\ddot{\phi}_i\rangle = -\frac{\partial E_v[\{\phi_i\},\underline{R}]}{\partial\langle\dot{\phi}_i|} + \sum_{j}\Lambda_{ij}\,|\phi_j\rangle\,. \tag{2.22}$$

Thus, the electronic degrees of freedom are associated with a fictitious temperature $\propto \sum_{i=1}^{n}\mu\langle\dot{\phi}_i|\dot{\phi}_i\rangle$. If μ is zero, the electronic subsystem is at its instantaneous minimum energy and, hence, at the Born-Oppenheimer surface, but the maximally possible timestep $\Delta t_{\max}$ is zero. $\Delta t_{\max}$ is inversely proportional to the highest frequency in the system and proportional to μ, *i.e.*

$$\Delta t_{\max} \propto \left(\frac{\mu}{E_{\mathrm{cutoff}}}\right)^{\frac{1}{2}} \tag{2.23}$$

in which E_{cutoff} is the energy cutoff in the kinetic energy of the plane wave basis set expansion (see Chapter 2.2). μ should be chosen with care as a large time step Δt is desirable for fast sampling of the phase space. For the accuracy of the simulation, adiabaticity and, thus, a decoupling of the electronic and nuclear motions is necessary. This is regulated by the value of μ as the electronic frequencies are inversely proportional to μ and the lowest possible electronic frequency $\omega_{\mathrm{min,e}}$ is $\propto (\frac{E_{\mathrm{gap}}}{\mu})^{\frac{1}{2}}$. The gap energy E_{gap} is energy difference between the highest occupied orbital and the lowest unoccupied orbital. As a consequence, systems with rather low or zero E_{gap} energies have to be treated rather carefully within the CPMD approach. For system with a large E_{gap} energy, the fictitious mass μ is chosen typically in the range of 300 a.u. to 1500 a.u. and time step Δt is about 0.05 fs to 0.24 fs. [145] In this work, μ was 400 a.u. and Δt 0.1 fs.

2.5 Classical molecular dynamics

Analog to AIMD, particles are moved according to Newton's laws, but the forces acting on the atoms are not obtained explicitly from the electronic structure as in AIMD. Instead empirical potentials are used to describe the effect of the mean electronic structure. Whereas intramolecular potentials are often expressed by harmonic

potentials for bonds, angles, and dihedrals, the intermolecular Van der Waals interactions are described by Lennard-Jones pair potentials and the electrostatic interactions by Coulomb's law. For all these potentials, parameters as the equilibrium bond length, equilibrium angle or dihedral, partial charges or Lennard Jones σ and ϵ values are derived from *ab-initio* calculations of mostly ground state structures of single molecules. Another approach is to fit the parameters such that the resulting force field gives the experimental value of certain properties as *e.g.* (crystal) structures, density, conductivity, viscosity, or heat of vaporization.
Another important aspect is that the system should be described in an ensemble comparable to the experimental setups. Experiments are mostly conducted at constant temperature rather than constant system energy which is preserved by the MD algorithms. For a simulation at constant temperature, a thermostat is needed to sample the correct ensemble. A standard approach which was also employed in this work is the Nosé-Hoover approach. [170, 171] For this global thermostat, the heat bath is integrated into the system by an artificial variable associated with an artificial mass. The extended Lagrangian results:

$$H_{\text{Nose}}(\underline{P}, \underline{R}, p_s, s) = \sum_{I=1}^{N} \frac{P_I^2}{2M_I s^2} + U(\underline{R}) + \frac{p_s^2}{2Q} + 3NkTln(s) \tag{2.24}$$

in which N is the number of atoms, Q is mass of the artificial variable, and p_s its momentum. For this Hamiltonian, the microcanonical ensemble average of the complete system including the artificial variable is equal to the canonical ensemble average of the real system's Hamiltonian. [172] However, thermostats can introduce artifacts and it is not trivial to obtain a canonical distribution by using the corresponding algorithms. Hence, depending on the specific simulation problem, thermostats such as velocity rescaling, Berendsen or Langevin ones as well as dissipative particle dynamics might be advantageous compared to the Nosé-Hoover approach.

2.6 Multiscale approach

The multiscale approach aims at a fundamental understanding of the ILs' properties on different levels of theory as well as various length and time scales. This knowledge shall enable a possibly predictive description of ILs without the necessity of experimental data. In order to reach such a reliable description on all scales, it is important to transfer the electrostatic and the structural properties consistently from one scale to another.
The levels of theory considered in this approach so far are the quantum based methods in which electrons are considered explicitly and classical atomistic models in which each molecule is described by a set of atomistic parameters. Quantum chemical calculations can treat only relatively small systems, but at an electronic level. Instead rather large systems can be described by classical MD, even though less accurately. The quantum description in this work was accessed on two different levels: post HF and DFT. While the former can provide explicit, systematically improvable information, the latter are more approximate, but have the potential to give a robust description of the electron density. Given the accuracy of post HF calculations, these

can be taken to gauge the quality of the DFT calculations as discussed in Chapter 1.3. Further, the DFT results on the bulk phase or DFT and post HF results on cluster ground state structures can be compared to classical MD observations. In this way, the consistency between all methods can be evaluated systematically.
By studying ILs on different length and time scales by the appropriate level of theory, an insight in the interplay of processes on many scales can be gained. The effect of temperature and entropy or cooperativity can be discussed by comparing ground state structure and finite temperature studies or by increasing the number of molecules. When going from an isolated ion to clusters to the liquid phase, the degree of complexity increases as the number of possible intermolecular interactions increases and cooperative effects may emerge. Indeed, the interactions present in clusters and in the liquid phase lead to a quantitative change of the electrostatic properties of the ions compared to isolated ions. [38, 94, 120, 121] Hence, the study of clusters of increasing size is one possibility to elucidate how this change emerges from the ions' interactions. Furthermore, large scale phenomena as conductivity can be only described by classical MD simulations. But their physical origin might be understood only if short ranged and fast polarization or relaxation processes are considered on an *ab-initio* level. In particular, the focus of this work was on the calculation of two quantities that are essential in modeling: atomic partial charges and molecular electric dipole moments. Classically, the electrostatic properties can be expressed by the molecule's multipole moments. Thus, classical force field parameters should represent the electric monopole and dipole properties found in quantum chemical calculations. Two main aspects which have to be considered by an accurate partial charge parametrization are charge transfer and polarization. In the former case, if charge transfer occurs, electron density is shifted from the anion to the cation *e.g. via* orbital overlap in hydrogen bonds and, thus, the net ion charges are physically reduced. This process is likely to be connected to a polarization of the molecule. In the latter case of polarization, an ion can be described as interacting effectively with its neighbors by an apparently reduced charge. A polarizable ion might have a charge of 1 e, but, in mean, it seems to influence its neighbors like a non-polarisable ion with an reduced charge below 1 e. Thus, whereas charge transfer is connected to a topological shift of electron density leading to reduced net ion charges, the mean effect of polarization can be modeled by reduced charges even if the net ion charges might still be physically at integer values. These phenomena can be studied only on the *ab-initio* scale, for the classical studies, they are set *a-priori* by the chosen model.

Chapter 3

Gas phase: a reference state

The balance between Coulomb and dispersive interactions and hydrogen bonds is discussed vividly in current research. [4,40,173,174] The simplest systems that may help to clarify basic principles are single ion pairs, although, these systems lack cooperativity which might be decisive in liquid phases. [175] However, the interactions present in a single ion pair already lead to a quantitative change in the electrostatic properties of the ions compared to isolated ions. [38, 94, 120, 121] Moreover, these small systems can be studied by accurate post-HF methods. For this reason, single ion pairs are often used as reference systems for gauging more approximate methods such as DFT with post-HF results (see Chapters 1.3 and 2.6).
In this chapter, the balance of the interactions will be studied first for ion pairs in their ground state structure (see Chapter 3.2) and second for the structure of an isolated ion pair at 400 K (see Chapter 3.3). In this way, the influence of temperature and entropy can be examined without the impact of cooperative effects.

3.1 Computational details

All calculations of static ground state structures were performed with the TURBOMOLE 6.2 package. [91, 176] We used DFT in combination with the dispersion corrected BLYP-D functional [110, 111, 113] as well as MP2. [177–179] The TZVP [180] and def2-TZVPP [181] basis sets were employed as implemented in the TURBOMOLE 6.2 package. All calculations were combined with the resolution of identity technique. The optimized structures were obtained by sequential geometry optimization with increasingly computationally demanding setups, *i.e.* BLYP-D/TZVP, BLYP-D/def2-TZVPP, MP2/TZVP, and finally MP2/def2-TZVPP.
Interaction energies were counterpoise-corrected by the procedure introduced by Boys and Bernardi. [182] The intrinsic interaction energies were calculated according to the supramolecular approach by subtracting the energies of the unrelaxed ions from the total cluster energy:

$$E = E_{\mathrm{AB}}(\vec{R_{\mathrm{A}}} + \vec{R_{\mathrm{B}}}) - E_{\mathrm{A}}(\vec{R_{\mathrm{A}}}) - E_{\mathrm{B}}(\vec{R_{\mathrm{B}}})\,, \tag{3.1}$$

in which $\vec{R_{\mathrm{A}}}$ and $\vec{R_{\mathrm{B}}}$ are the coordinates of ions A and B in the ion pair.
The NPA [76,77] and the SEN analysis [79–81,163] were carried out with the TURBO-

MOLE 6.2 implementation. Electrostatic potentials were calculated with the TURBOMOLE 6.2 package and visualized by the free software GOPENMOL. [183]
AIMD simulations of single ion pairs at 400 K were performed by using the CPMD approach [169] and the BLYP-D setup and corresponding pseudopotentials were used. This BLYP-D DFT setup was tested to reproduce the energetic order of ion pair conformations found by MP2. Kohn-Sham orbitals were expanded in a plane wave basis with a kinetic energy cutoff of 35 E_h (70 Ry) and the fictitious electron mass was 400 m_e. For isolated ion pairs in a simulation box of $(0.2\ \text{nm})^3$, a timestep of 0.1 fs and standard Nosé-Hoover thermostats [170, 171] were applied. The simulations were started from the MP2 optimized structures obtained before. The equilibration time was chosen to be 10 ps. To ensure better sampling, for each IL, simulations were started from more than one optimized structure: three simulations of a total 197 ps (77.6 ps, 62.9 ps, and 55.6 ps) for EMIM DCA and two simulations of a total 152 ps (76.1 ps and 76.4 ps) for BMIM 5AT. The probability as a function of angle and distance was calculated by TRAVIS [184] and plotted with Mathematica.
For an easier reading, as all energies presented here are negative, the discussion will refer to the absolute value of the energies $|E|$ in the following chapters.

3.2 Ground state structure

In order to study the interplay between different interactions, several ion pairs of ILs, varying in the sidechain length of the imidazolium cation and in the anion, were studied. The longer the sidechain of the imidazolium cation is, the more dominant dispersive interactions are. Here, 1,3-dimethylimidazolium (MMIM), 1-ethyl-3-methylimidazolium (EMIM), and 1-butyl-3-methylimidazolium (BMIM) were considered. For the anions, simple inorganic anions such as chloride (Cl), thiocyanate (SCN), dicyanamide (DCA), and tetrafluoroborate (BF_4) were chosen. Chloride and tetrafluoroborate are spherically shaped whereas thiocyanate and dicyanamide are more rod-like. The basicity and, thus, the hydrogen bond acceptor strength decrease from chloride, thiocyanate, dicyanamide to tetrafluoroborate. [40] Furthermore, two larger organic anions were considered in the study: 5-aminotetrazolate (5AT) and 4-nitroimidazolate (4NI). Structurally, these ions are rather similar to the imidazolium cation as they consist also of five-membered nitrogen rich aromatic rings. Therefore, the preferred conformations might change significantly compared to the inorganic anions.
In general, two important configurations [97] out of many local minima were considered: a configuration having a hydrogen bond at the most acidic C^2H position (for nomenclature see Figure 1.3) (denoted with **hb**) and a stacked conformation in which the anion is located above the imidazolium ring (denoted with **st**). These two conformations differ in the relative contributions of the molecular interactions more than other local minima. For this reason, these two conformations might be especially suitable for gaining some insight into the interaction balance without studying the full potential energy surface. As the potential energy surface is said to be very flat, [30, 31, 49] ions will move easily away from energy minima at finite temperature anyway.
Therefore, the initial structures were set up in **hb**- and **st**-like conformations and the

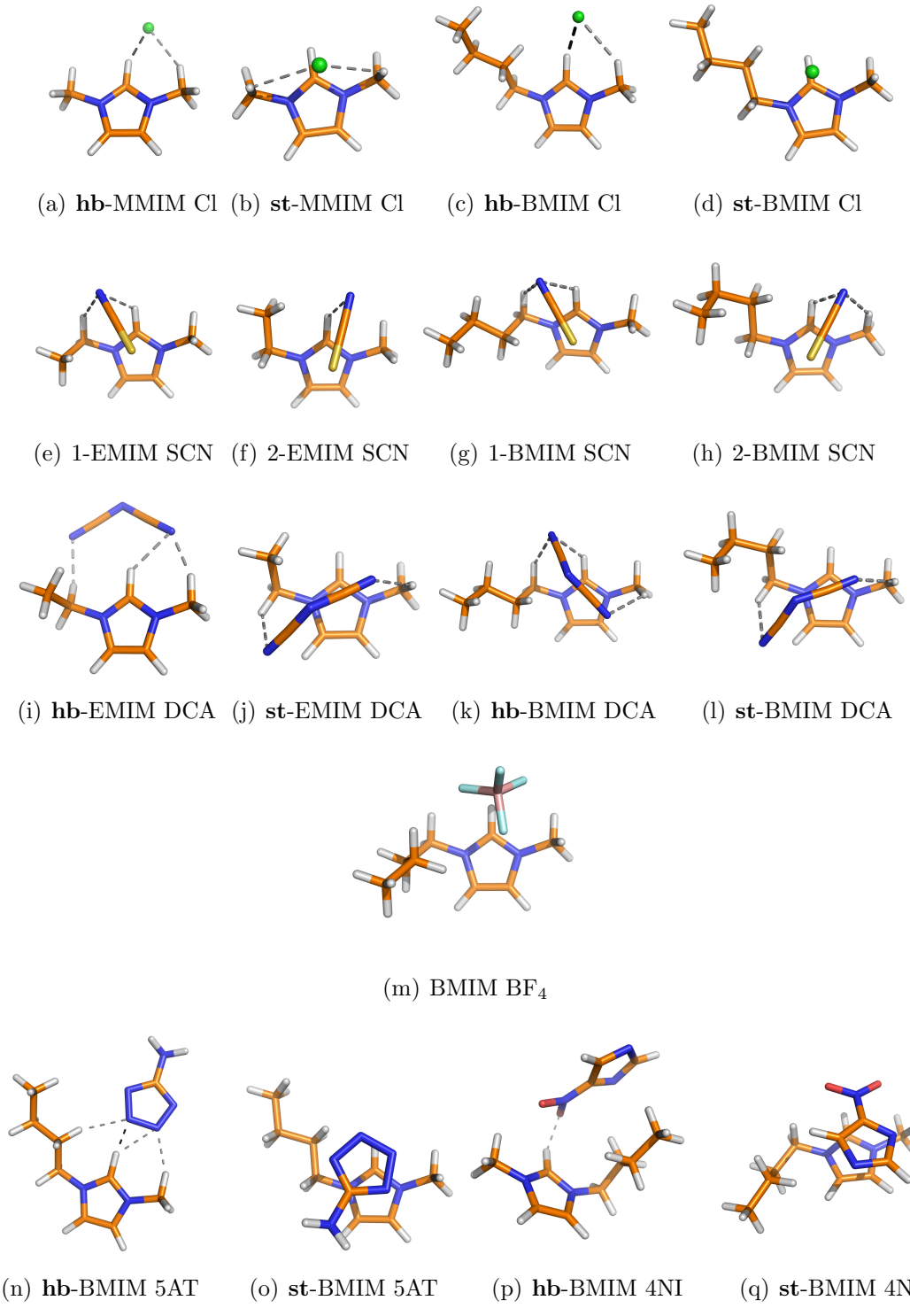

(a) **hb**-MMIM Cl (b) **st**-MMIM Cl (c) **hb**-BMIM Cl (d) **st**-BMIM Cl

(e) 1-EMIM SCN (f) 2-EMIM SCN (g) 1-BMIM SCN (h) 2-BMIM SCN

(i) **hb**-EMIM DCA (j) **st**-EMIM DCA (k) **hb**-BMIM DCA (l) **st**-BMIM DCA

(m) BMIM BF_4

(n) **hb**-BMIM 5AT (o) **st**-BMIM 5AT (p) **hb**-BMIM 4NI (q) **st**-BMIM 4NI

Figure 3.1: Schematic structures of the ion pairs studied (blue: N, green: Cl, light blue: F, orange: C, purple: B, red: O, white: H, yellow: S).

final ion pair conformations are given in Figure 3.1 in the MP2/def2TZVPP optimized structure. In general, the structures were very similar for ion pairs having the same anion. The sidechain did not appear to have a significant influence as the ions

were close to the imidazolium ring rather than to the sidechain. In some cases, the hydrogen bonded position was not kept during the optimization procedure and the anion moved in a stacked position, as for EMIM SCN, BMIM SCN and BMIM DCA. Therefore for EMIM SCN and BMIM SCN, the hydrogen bonded stacked conformations are called 1 and 2. **hb**-BMIM DCA still had a hydrogen bond to the C^2H hydrogen which was not found in **st**-BMIM DCA. A BMIM DCA conformation similar to **hb**-EMIM DCA was found to be stable with a B3LYP/6-31+G(p,d) setup [95] as well as with BLYP-D/def2-TZVPP here. Only during the geometry optimization with MP2/def2-TZVPP, the anion was transferred in a stacked position due to the influence of dispersion. However, sometimes dispersion is overestimated by MP2.
In the following chapters, the three different interactions present and their relative influence will be discussed.

3.2.1 Coulomb interactions

Intuitively, the Coulomb interactions should dominate the energetics and structure of ion pairs since the monopole monopole interaction is the first term in the multipole expansion. Indeed, this was verified here and also for other ILs considered in the literature [48, 98, 105]. In general, the interaction energies were very high due to the presence of Coulomb interactions. They were between −341 kJ/mol and −418 kJ/mol for MP2 and between −282 kJ/mol and −384 kJ/mol for HF (see Table 3.1). These energies were much larger than the interaction energies of uncharged molecules which are mostly well below −100 kJ/mol. As a rough estimate, **hb**-MMIM Cl could be approximated very coarsely by its monopole structure which consisted of two charges of 0.75 e [84] at the centers of charge of the ions at a distance of 250 pm. The associated Coulomb energy would be 310 kJ/mol which was well within the range of the observed interaction energies. Zahn *et al.* [31] found by the symmetry-adapted perturbation theory (SAPT) analysis that electrostatic interaction accounts for about 80 % of the total interaction energy of the MMIM Cl ion pair at the equilibrium distance.
The optimized conformations were characterized by minimal charge separation (see also Refs. [48, 98]). In all cases, the anion oriented itself in such a way that the negative charged part was closest to the N-C^2-N part of the imidazolium ring where the positive charge was located. For instance, the negatively charged tetrazolate ring was above the imidazolium ring in **st**-BMIM 5AT instead of the amino group (see Figure 3.1). In **st**-BMIM 4NI, the negatively charged nitro group was closer to the N-C^2-N part of the imidazolium ring than the imidazolate ring. The interaction energies calculated with both HF and MP2 were the largest for the smallest anion Cl whose charge separation distance to the cation was the lowest. Thus, the Coulomb energy was the largest in these Cl ion pairs compared to ion pairs with other anions. However, often the electron density and, hence, the Coulomb interactions are mapped on atomistic partial charges in order to design classical models. Already in ion pairs, the ion net charges were found to be reduced below the formal integer charges (see Table 3.1 and Ref. [38,44,74,83,84,96,102,107]). This reflected that the electron densities of the ions overlapped and charge transfer occurred (see also Chapter 3.2.3). Hence, there were physical reasons for ion net charges below the integer values. The NPA

Table 3.1: Intrinsic interaction energy E_{int} and sum of estimated hydrogen bond energies $E_{\text{hb,sum}}$ in kJ/mol as well as the net charge of the cation q_{cation} obtained with NPA in units of e.
Single point energies are given in Table A.1.

	$E_{\text{int,HF}}$	$E_{\text{int,MP2}}$	$\Delta E = E_{\text{int,MP2}} - E_{\text{int,HF}}$	$E_{\text{hb,sum}}$	q_{cation}
hb-MMIM Cl	−383	−409	−26.2	−190 *	0.82
st-MMIM Cl	−384	−419	−34.5	−30	0.84
hb-BMIM Cl	−381	−409	−27.9	−180 *	0.82
st-BMIM Cl	−376	−412	−35.9		0.85
1-EMIM SCN	−327	−384	−56.9	−30	0.95
2-EMIM SCN	−331	−386	−54.2	−25	0.94
1-BMIM SCN	−324	−385	−61.1	−28	0.94
2-BMIM SCN	−324	−382	−57.5	−39	0.94
hb-EMIM DCA	−319	−354	−35.8	−80	0.94
st-EMIM DCA	−306	−369	−62.8	−31	0.97
hb-BMIM DCA	−306	−371	−64.8	−40	0.97
st-BMIM DCA	−300	−370	−69.9	−32	0.96
BMIM BF_4	−340	−366	−26.0		0.97
hb-BMIM 5AT	−355	−388	−32.9	−160 *	0.87
st-BMIM 5AT	−332	−410	−78.1		0.94
hb-BMIM 4NI	−294	−341	−47.7	−44	0.92
st-BMIM 4NI	−282	−377	−94.5		0.95

* One of hydrogen bonds is connected to an energy exceeding the energy range for which the SEN method was parametrized.

based ion net charges (see Chapter 2.3.4) were below ±1 e in any case, but were especially low for the chloride containing ion pairs. Chloride was the strongest hydrogen bond acceptor considered here. Regarding this, the extended charge transfer might be understandable and was consistent with known results for MMIM Cl [102, 107] as well as BMIM Cl. [96] In general, the hydrogen bonded conformations were associated with lower net charges. The NPA net charges for **hb**-MMIM Cl were consistent with the Bader analysis. [84] Other methods, such as CHELP, RESP or Blöchl (see Chapter 2.3.3) assigned lower net charges to the ions. [74, 83, 84, 107] However, these methods fit the electrostatic potential and, thus, include polarization effects in the partial charge description. They describe the effective monopole structure rather than the electron density distribution of the ions. NPA and Bader methods (see Chapter 2.3.2) instead assign the electron density to atoms and, hence, can capture the charge transfer only. However, the presence of charge transfer meant that the interactions between the ions were not purely ionic, there was some covalent character. Thus, even though electrostatics were the dominant interaction, other interactions such as dispersion or hydrogen bonding played a role.

3.2.2 Dispersion

As discussed in Chapter 1.3, the inclusion of dispersion interactions is important in order to reproduce the right energetic order of the ground state structures of single ion pairs. [30, 84, 90, 104, 105, 185] Dispersion influences the mutual orientation of the ions if they are close to each other and the centers of charge distance and, thus, the Coulomb forces do not vary much anymore. Indeed, dispersion was shown to shorten the interionic distance. [30, 90] As elsewhere, [90, 104, 105, 185] the difference between the interaction energies calculated with HF and MP2 will be taken as estimate of the dispersion energy even though it captures additional effects. However, correlated methods that are more accurate than MP2 did not lead to results significantly different from MP2. [104, 105] Thus, MP2 seemed to describe the dispersion corrections with sufficient accuracy.
In general, dispersion gave a significant contribution to the total interaction energy of the studied ion pairs and was decisive for the more stable conformations (see Table 3.1). The dispersion energies ranged from −26 kJ/mol to −95 kJ/mol, accounting for 7 % to 25 % of the total MP2 interaction energy (see Table 3.1). Similarly for pyrrolidinium-based ILs, values of −26 kJ/mol to −43 kJ/mol accounting for 7 % to 14 % of the total MP2 interaction energy were reported. [104] Furthermore, the energy difference between **hb**-MMIM Cl and **st**-MMIM Cl was consistent with literature [102, 107, 119] as well as the almost degenerate energies of the BMIM Cl conformations [96] for which the actual energy ordering depended crucially on the applied method, DFT, MP2, or CCSD(T), and the basis set. [186] The stacked conformations were not only connected to higher dispersion energies, but also to higher total interaction energies except for BMIM DCA. As **hb**-BMIM DCA was also in a stacked orientation (see Figure 3.1), **hb**-BMIM DCA and **st**-BMIM DCA had about the same total interaction energy.
The magnitude of the observed dispersion seemed to be connected rather closely to the anion size. The small chloride and the less basic BF_4, having a localized hard electron density, gave the lowest dispersion contribution of about 30 kJ/mol. For rod-like SCN and DCA anions, dispersion dominated the mutual orientation of the ions. The SCN and DCA anions were always stacked above the ring, except for **hb**-EMIM DCA. A position of the anion in front of C^2H in the imidazolium planei (for nomenclature see Figure 1.3) was not a local minima for all the other SCN and DCA ion pairs. The dispersion energy was about −60 kJ/mol and, thus, 17 % of the total interaction energy. The aromatic anions 5AT and 4NI had significant dispersion interactions to the cation in the stacked conformation. For **st**-BMIM 4NI, the dispersion energy was about −94.5 kJ/mol which was about 25 % of the total MP2 interaction energy. This might indicate $\pi - \pi$ interactions which could be hardly described by DFT and, by this, restrict the applicability of AIMD for this IL. However, the 5AT and 4NI anions were also larger than the SCN or DCA anions. Thus, the higher dispersion contribution might be in agreement with the larger size and not necessarily connected to a different interaction mechanism.
The dispersion energy was rather insensitive to the sidechain length as, for instance, the dispersion contribution for BMIM Cl conformations was less than 2 kJ/mol and, thus, only about 5 % higher than for MMIM Cl (see Table 3.1). This is explained by the fact that the anions were closer to the imidazolium ring than to the sidechain in

order to maximize the Coulomb interaction (see Chapter 3.2.1). The anion did not interact differently with a longer sidechain than with a short sidechain. Indeed, only the structures of **hb**-EMIM DCA and **hb**-BMIM DCA were significantly disparate. The dispersion interaction was more influential in **hb**-BMIM DCA as the anion moved to a stacked position. For **hb**-BMIM 4NI, the charged nitro group formed a hydrogen bond to the C^2H hydrogen meanwhile the anion was not in plane with the cation as for **hb**-BMIM 5AT. In this way, the dispersive interaction was increased as the anion's imidazolate ring was close the cation's sidechain. Altogether, it can be concluded that dispersion was decisive in the ground state structure of isolated ion pairs. Nevertheless, for all but the SCN based ion pairs and **hb**-BMIM DCA, a stable hydrogen bonded conformation in which the ions were not stacked was found. This indicates the importance of hydrogen bonding which will be discussed next.

3.2.3 Hydrogen bonds

While the influence of hydrogen bonds and their definition is still widely discussed, [32, 48, 96, 102, 173] the energy contribution of hydrogen bonds is difficult to capture. Here, the hydrogen bond energy was estimated by using the shared electron number (SEN) approach [79, 80, 163, 168] (see Chapter 2.3.5) which enables the detection of hydrogen bonds without any arbitrary cutoffs. However, the method was developed for uncharged molecules [168] for which the interaction energy was identified with the hydrogen bond energy. This interaction energy was fitted as a linear function of the SEN between the hydrogen bond acceptor and the hydrogen (see also Chapter 2.3.5). Therefore, the SEN approach gives an estimate of the hydrogen bond energy connected to covalent bonding detected by the SEN.
Another criterion often applied to identify hydrogen bonds is the Van der Waals cutoff distance. It states that the distance between a hydrogen and the hydrogen acceptor atom has to be lower than the sum of the Van der Waals radii of the hydrogen and the acceptor atom. [187] This implies the following cutoff distances: $r_{H\cdots F} = 257$ pm, $r_{H\cdots N} = 265$ pm, $r_{H\cdots O} = 262$ pm, and $r_{H\cdots Cl} = 285$ pm. [188, 189] Meanwhile, this criterion is criticized for being too restrictive. [187] If hydrogen bonds are seen to be connected to charge transfer, the evaluation of the minimal electron density at the hydrogen bond axis might be useful. The higher this minimal density is, the more covalent and, thus, stronger the intermolecular bond appears.
While most ion pairs had hydrogen bonds of similar strength than between uncharged molecules with hydrogen bond energies between -28 kJ/mol and -40 kJ/mol, chloride and 5AT formed very strong hydrogen bonds. The distance and minimal density criteria agreed with the SEN based results. The three ion pairs **hb**-MMIM Cl, **hb**-BMIM Cl, and **hb**-BMIM 5AT were bound very strongly. All formed twofold hydrogen bonds, in which one acceptor binds to two hydrogen atoms. Only one of these bonds, the hydrogen bond to the C^2H group, was connected to a SEN of more than 0.1 e which is unusually high for hydrogen bonds with carbon as hydrogen donor. Furthermore, the minimal electron density at these intermolecular bond axes had a rather high value. It was about 0.05 e/bohr^3 while it was between 0.01 e/bohr^3 and 0.02 e/bohr^3 for the other hydrogen bonds. Only, the single hydrogen bond of **hb**-BMIM 4NI was characterized by a medium minimal electron density of about 0.03 e/bohr^3. Dispersive

contacts of ions in stacked conformation had a electron density minimum of about 0.01 e/bohr^3 or less. Only for **st**-MMIM Cl and **st**-BMIM Cl, the density minimum was at roughly 0.035 e/bohr^3 and, thus, comparable to stronger hydrogen bonds. Regarding these numbers, the minimal density seemed not a good criterion to differ between dispersion and medium or weak hydrogen bonds. The three strong hydrogen bonds had also hydrogen acceptor distances which were typical for strong hydrogen bonds as 187 pm in **hb**-BMIM 5AT and about 193 pm in the chloride ion pairs. In liquid water, for comparison, the hydrogen bond length is about 197 pm in the ground state structure of water dimers about 195 pm. Hence, all three approaches, SEN, minimal density, and distance, were consistent. For chloride ion pairs, the charge transfer and interionic molecular overlap was found to be significant also by Hunt *et al.* [96] However, all hydrogen bonds detected with SEN obeyed the Van der Waals cutoff distance criterion. The bond lengths of H$\cdots$N and H$\cdots$O hydrogen bonds were between 210 pm and 244 pm, H$\cdots$Cl ones extended up to 276 pm. Still, there were some hydrogen acceptor atom contacts which had a distance below the cutoff criterion and had a density minimum like hydrogen bonds, but were not identified as hydrogen bonds by SEN method. Especially, for BMIM BF_4, the SEN did not describe a hydrogen bond but the shortest two C^{2}H$\cdots$F distances were 220 pm and 229 pm, respectively, and the minimal density was about 0.016 e/bohr^3 and 0.014 e/bohr^3. Thus, these two hydrogen bond descriptors would imply that there were hydrogen bonds. That may hint at some inconsistencies and shows the difficulties in establishing a hydrogen bond criterion. All in all, the three methods proposed that were several typical hydrogen bonds present in the ion pairs. Only in three ion pairs, there was one very strong hydrogen bond.

Additionally, the directionality of the hydrogen bond is important as it is proposed to be linked to the diffusion properties of the liquid [30, 173, 174] or the melting point. [41,42] For ground state ion pair conformations of MMIM Cl, an energy barrier of about 8 kJ/mol was observed if the anion moved from the stacked to the hydrogen bonded position. [30] Thus, an energy barrier would be expected as well for BMIM 5AT which formed equally strong hydrogen bonds. Unfortunately, the assignment of an activation energy was not possible within this study as the ions had so many degrees of freedom and the reaction coordinates remained unknown. However, it was apparent that there was an energy barrier: any geometry optimization of an initial structure in which the anion was in front of the C^2 led to a C^{2}H hydrogen bonded configuration. Despite the similar aromatic structure, such an energy barrier was not detected for BMIM 4NI. Additionally, initial BMIM 5AT monomer structures close to the C^{4}H or C^{5}H-hydrogen bonded conformations were transformed to stacked conformations during geometry optimization and, therefore, they were not stable. In this way, for BMIM 5AT, only the C^{2}H hydrogen bonded conformation appeared rather stable with respect to a stacked conformation. One might speculate that this is connected to the experimental observation of strong intermolecular interactions and intermediate range order in BMIM 5AT not present in BMIM 4NI. [10]

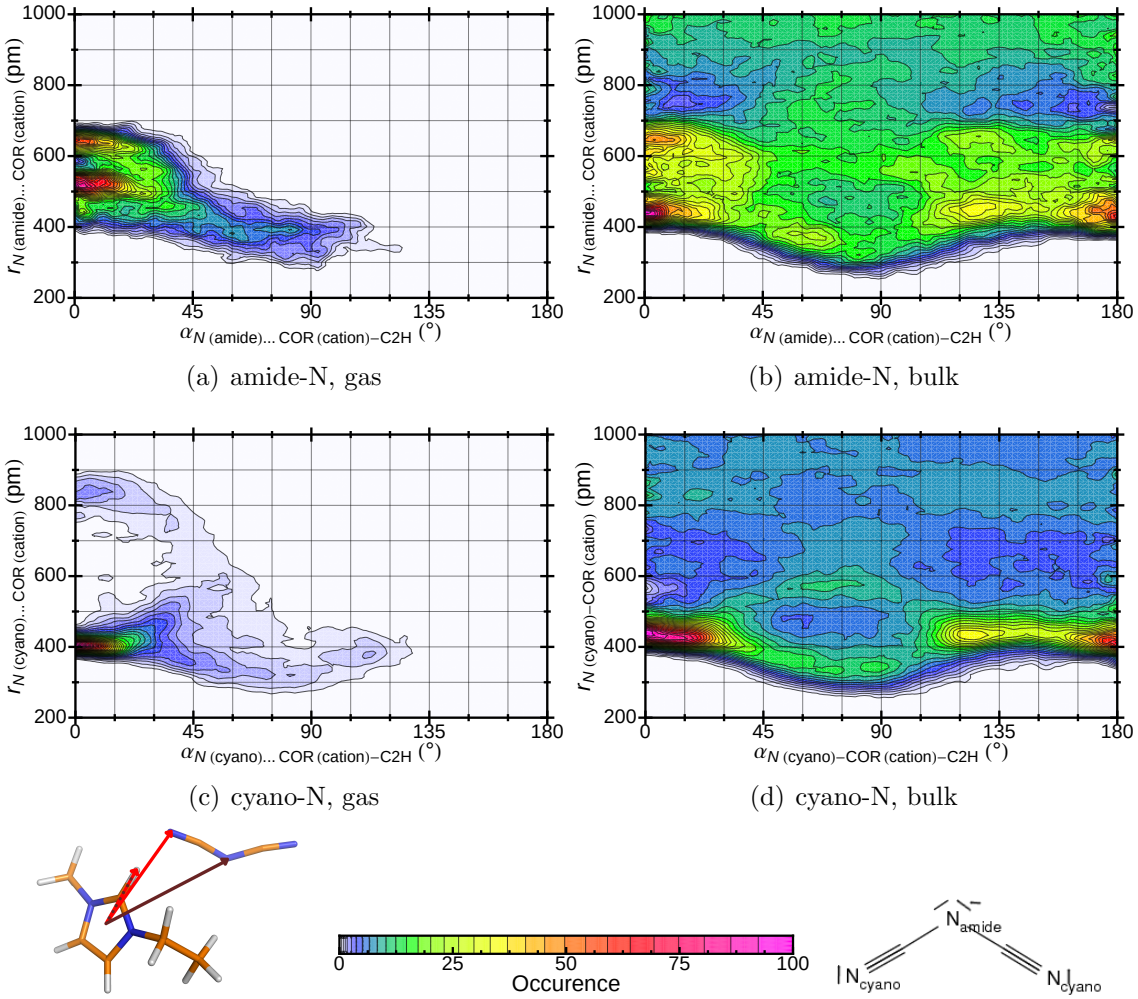

(a) amide-N, gas

(b) amide-N, bulk

(c) cyano-N, gas

(d) cyano-N, bulk

Figure 3.2: Projection of the normalized probability distribution of finding an ion pair with an intermolecular angle $\alpha_{\mathrm{N(anion)\cdots COR(cation)-H^2}}$ (between an anion nitrogen atom, the cation's COR and the C^2H hydrogen atom) at the intermolecular distance $r_{\mathrm{N(anion)\cdots COR(cation)}}$ (between the anion nitrogen atom and cation's COR). a) and (c) give the distribution for an EMIM DCA ion pair in the gas phase at 400 K, and (b) and (d) for 30 EMIM DCA ion pairs in the liquid-like bulk phase at 400 K. For (a) and (b), the amide nitrogen atom was chosen as reference whereas for it was the cyano nitrogen atoms for (c) and (d) (compare to schematic presentations). The probability was normalized such that the highest probability value is equal to 100 and the color scheme ranges from white (low) to violet (high).

3.3 Finite temperature structure

In the liquid phase, which most experiments study, the properties are influenced by cooperativity of many interacting ions as well as by temperature. Both effects cannot be captured by ground state structures. Even zero point vibrations present at 0 K are often not included in the ground state studies as *e.g.* in [31, 32, 48, 90, 96, 97, 105, 186]

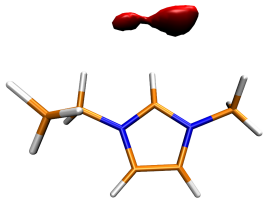

Figure 3.3: Isosurface of the spacial distribution function of the anion around the cation for one EMIM DCA ion pair at 400 K at an isovalue of 160 nm^{-3}. The reference plane is defined by the N-C^2-N group of the imidazolium ring.

or Chapter 3.2. Hence, it might be useful to separate the effect of cooperativity, studied in chapter 4, and temperature by studying single ion pairs at finite temperature. Furthermore, such an investigation can shed light on the gas phase properties of ILs which are also important for some applications, experiments, or theory. [95, 190–193] Entropically, the formation of ion pairs was favored over network structures at higher temperatures [194] and, at temperatures above 500 K, even the formation of single ions occurred. [195] Also, it is discussed that entropy effects may partially explain why the ground state properties of single ion pairs do not always correlate with observed physical properties of the liquid phase. [185] Therefore, the gas phase structure of single ion pairs of EMIM DCA and BMIM 5AT was investigated at 400 K by AIMD. The results will be discussed with respect to the relative influence of the three main interactions in analogy to the discussion of the ground state structures in the previous Chapter 3.2.

As for the ground state structures, Coulomb interactions were decisive as the ions were always close to each other and, hence, formed an ion pair in the gas phase at 400 K. Furthermore for both EMIM DCA and BMIM 5AT, the anion was close to the positively charged N-C^2-N part of the imidazolium ring. Thus, the angle α between the anion center of reference, the center of the imidazolium ring, and the C^2H hydrogen was nearly always below 90 ° (see Figures 3.2 and 3.4). Hence, the distance between the ions' centers of charge was kept small.

In the ground state structures, dispersion was dominant compared to hydrogen bonds. The stacked ion pair ground state conformations were found to have higher interaction energies and total energies than hydrogen bonded structures (see Chapter 3.2.2). A hydrogen bonded EMIM DCA ion pair was about 10 kJ/mol less stable than a stacked pair. However, at finite temperature, for instance 400 K, 1 kT equals about 3.3 kJ/mol. Thus, as several degrees of freedom are excited, small energy barriers can be overcome and conformations with higher energies can be occupied. The energy difference between stacked and hydrogen bonded conformations should allow for an exchange between the two conformations during a simulation at 400 K. Indeed, the transition from a stacked initial structure to a hydrogen bonded conformation was observed during the simulations of EMIM DCA and BMIM 5AT.

In general, the ion pairs at 400 K were much more influenced by hydrogen bonding than by dispersion interactions which might be due to the higher entropy of the hydroden bonded ion pair conformation. For EMIM DCA, one of the cyano nitrogen atoms of the anions was fixed rather tightly to the strong hydrogen bond position in

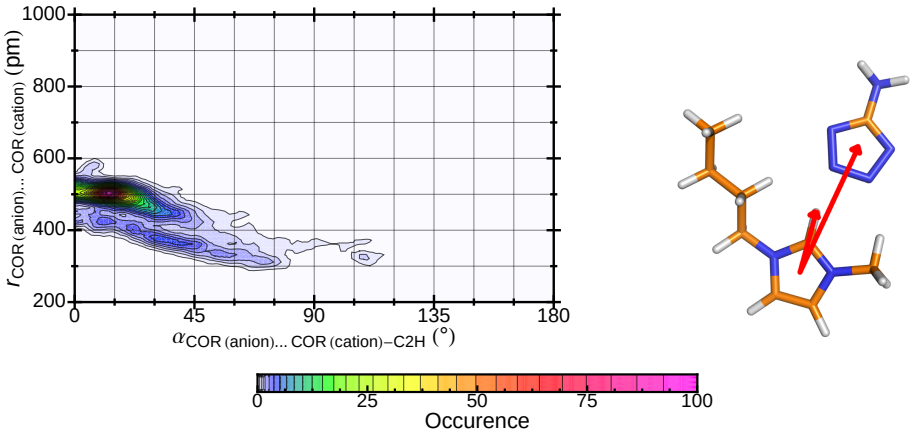

Figure 3.4: Projection of the normalized probability distribution of finding an ion pair with an intermolecular angle $\alpha_{COR(anion)\cdots COR(cation)-H^2}$ (between the anion's COR, cation's COR and the C^2H hydrogen atom) at the intermolecular distance $r_{COR(anion)\cdots COR(cation)}$ (between the anion's COR and the cation's COR) for a BMIM 5AT ion pair in the gas phase at 400 K. The probability was normalized such that the highest probability value is equal to 100 and the color scheme ranges from white (low) to violet (high).

front of the C^2H hydrogen (see Figure 3.2 (c)). The other cyano nitrogen moved more freely and did not give rise to a second clear peak in the histogram. The amide nitrogen was highly likely to be in front of C^2H hydrogen (see Figure 3.2 (a)), although at larger distances than the cyano nitrogen. That means that, mostly, the anion was hydrogen bonded to the C^2H hydrogen *via* a cyano nitrogen and the anion pointed roughly linearly away from the cation. The amide nitrogen was hardly ever observed in a stacked conformation. This is also reflected in the spacial distribution function of the anion with respect to the cation (see Figure 3.3). There, it is shown that the anion was most likely in two non-stacked positions where two-folded hydrogen bonds could be formed similar to the situation in the ground state structure **hb**-EMIM DCA (compare Figure 3.1).

If the properties of single ion pairs are correlated to liquid phase data, it is implicitly assumed that the short range order of the liquid phase is similar to that of single ion pairs. Hence, for evaluating this hypothesis, the liquid phase data is shown as well in Figure 3.2 (b) and (d). It is obvious that the cation-anion conformations were more diverse in the liquid phase. Compared to the gas phase, the stacked conformation was more likely in the liquid phase and the anion was also found in C^4H or C^5H hydrogen bond positions not occupied by the gas phase ion pair. Furthermore, the most likely distance of both $r_{N(amide)\cdots COR(cation)}$ and $r_{N(cyano)\cdots COR(cation)}$ was about 420 pm in the liquid phase whereas, in the gas phase, the most likely distance $r_{N(cyano)\cdots COR(cation)}$ was about 400 pm and, thereby, lower than the distance to the less basic nitrogen $r_{N(amide)\cdots COR(cation)}$ of about 510 pm. This showed that different conformations were sampled in the liquid phase than in the gas phase, but these conformations still resembled the found ground state structures.

For BMIM 5AT, two configurations are separated clearly in the histogram 3.4: the

hydrogen bonded conformation at lower angles and larger distances and the stacked one at larger angles and smaller distances. Again, the hydrogen bonded conformation was more occupied. In the ground state, the stacked conformation **st**-BMIM 5AT had a distance $r_{COR(anion)\cdots COR(cation)}$ of 309 pm and an angle $\alpha_{COR(anion)\cdots COR(cation)-H^2}$ of 61.9 °. Such a configuration did not have a significant probability at 400 K.
A possible explanation for the increased influence of hydrogen bonding is that the free energy surface was very shallow in stacked orientations dominated by dispersion whereas the hydrogen bond was characterized by a steeper local free energy minimum. If the anion formed a hydrogen bond to the acidic C^2H hydrogen, only the hydrogen bond acceptor atom of the anion was rather fixed in position which led to very high normalized probabilities of these positions (compare Figures 3.2 and 3.4). The other atoms of the anion could move freely and the entropy of the ion pair was rather high. If the anion adopted a stacked position above the imidazolium ring, several atoms of the anion had to be close to the imidazolium ring. Thus, the entropy was very much reduced. Also, vibrations and small motions led to a strong decrease in the dispersion interactions as these evolve with r^{-6}. [185] Hydrogen bonding has an electrostatic energy component which decreases more slowly with r^{-1} and was proposed to decay overall with about $r^{-3.8}$. [168] Since the dispersion interactions decay the fastest when ion pairs leave the ground state structure, their influence on the finite temperature structure seemed to be the lowest. Furthermore, entropy might favor the hydrogen bonded conformation in which the anion can move freely.

3.4 Conclusion

In this chapter, the balance of electrostatic, dispersion, and hydrogen bond interactions was examined for single ion pairs which are widely studied model systems. It was shown that the Coulomb interaction was the strongest contribution to the interaction energy of ion pairs in their ground state and at finite temperature. In the ground state, dispersion proved decisive as stacked conformations were associated with higher interaction energies. However at 400 K, the hydrogen bonded structures were more likely to occur. Therefore, temperature and, possibly, entropy changed the relative importance of the interactions. For this reason, correlating static ground state structure properties and liquid phase data is a tedious task, especially, since often only anion cation pairs are considered. By this, the contribution of pairs of equally charged ions are neglected. These possibly interact differently by *e.g.* π-π stacking or dispersion between long side chains. [185]
In the liquid phase, ions are surrounded by numerous other ions and cooperative effects come into play. The ions experience dispersion and Coulomb forces from many directions and may be involved in several hydrogen bonds. Hence, the directionality of the interactions, which is characteristic for an ion pair, is lost in liquid phase to some extent. Due to this complexity in the bulk phase, the contribution of the interactions, as discussed here for single ion pairs, might lead to a different scenario in the liquid phase. This is studied within the next chapters: In Chapter 4, the focus is on the electrostatic interactions which give general characteristics of ILs. Subtle differences, caused by hydrogen bonding and dispersion interactions, are discussed in Chapter 5.

Chapter 4

Liquid phase: electrostatics and common properties

The correct parametrization of the molecular electrostatic properties is decisive for the success of classical force fields. [38,55,63,67,192,196,197] For this, *ab-initio* molecular dynamics (AIMD) simulations offer an elegant way to access the electrostatic properties of a liquid-like phase as the electron structure is described explicitly and effects of *e.g.* polarization are captured. Mostly, the focus in force field development is on the two first quantities in the multipole expansion: atomic partial charges and molecular electric dipole moments. Hence, in the following, the electric monopole and dipole structure found in AIMD simulations will be discussed (see Chapters 4.2 to 4.4). Another crucial question in force field development is the influence of polarization which is discussed in Chapters 4.5 and 4.6.
On the whole, ILs appear to be systems convenient for AIMD studies as there are indications for a strong screening of effective interactions [119] and, hence, small systems should capture the decisive effects. If this is valid, the properties of small systems should be identical to the ones found for larger systems, system size effects in simulations should be small. In this way, the study of rather small bulk systems, *e.g.* of about 30 ion pairs could describe the thermodynamic state point within reasonable accuracy and without loss of generality. Furthermore, it is proposed that solvent fluctuations show fast subpicosecond processes. [14] In this subpicosecond regime, the anion stays close to a certain cation, but fluctuates around it. This means that the local structure should adapt sufficiently fast to reach equilibrium at times easily accessible to AIMD. In the following, these assumptions will be tested systematically by studying electrostatic properties in various systems of different size (see Chapters 4.2 and 4.3), their time dependence (see Chapter 4.3), and their range of correlations (see Chapter 4.4).
In general, system sizes being representative of the liquid phase are accessible by DFT, but they are computationally prohibitive for post HF methods. However, the highly accurate electronic structure given by post HF methods may not be necessary for understanding larger bulk scale properties. As the consistency between DFT and MP2 results [38, 84, 90, 94, 104] indicated a basic agreement in the electron structure described by the methods, DFT might give the essential statistical and thermodynamic properties.

4.1 Computational details

Car-Parrinello molecular dynamics [169] (CPMD) simulations were performed to study liquid phase properties of several ILs by using the CPMD package. [92] This work includes some of the largest *ab-initio* simulations of ILs ensuring extensive sampling and equilibration. In all simulations, the Kohn-Sham orbitals were expanded in a plane wave basis with an kinetic energy cutoff of 35 E_h (70 Ry), the fictitious electron mass was 400 m_e. Periodic boundary conditions, a timestep of 0.1 fs (4 a.u.) and standard Nosé-Hoover thermostats [170, 171] for atoms and electrons were applied. The BLYP functional [110, 111] with Troullier-Martins pseudopotentials, derived using the BLYP functional, and an empirical dispersion correction [113] were employed unless otherwise specified. This setup has been recommended in literature. [90, 104] Additionally, further checks were done for this work by studying three one ion pair clusters of EMIM DCA, ion pair conformations of other ILs (see Chapter 3), small clusters of MMIM Cl [84], and six adducts of one EMIM DCA ion pair and a sulfur dioxide molecule. The ground state structures and relative single point energies found by the BLYP-D DFT setup were in qualitative agreement with those obtained by MP2/def2-TZVPP level of theory. For the MMAN ion pairs, DCACP-BP86 pseudopotentials [117] which were tested accurately for this system in previous work were used instead. [33] Unless otherwise specified, the simulations were started from an equilibrated snapshot of a classical MD simulation [198] and the equilibration time was chosen to be five ps. An overview of the systems is given below:

1. eight ion pairs MMIM Cl, 425 K, $(1.162\ \mathrm{nm})^3$, 79.82 ps with the PBE setup of the 30 MMIM Cl system; [121]
2. eight ion pairs EMIM Cl, 400 K, $(1.215\ \mathrm{nm})^3$, 106.0 ps with the PBE setup of the MMIM Cl systems;
3. 30 ion pairs BMIM Cl, 400 K, $(2.021\ \mathrm{nm})^3$, 22.85 ps;
4. eight ion pairs EMIM SCN, 400 K, $(1.264\ \mathrm{nm})^3$, 67.83 ps;
5. 32 ion pairs EMIM SCN, 400 K, $(2.006\ \mathrm{nm})^3$, 6.41 ps; (started from an *ab-initio* trajectory [37] snapshot);
6. 48 ion pairs EMIM SCN, 400 K, $(2.297\ \mathrm{nm})^3$, 1.08 ps (0.5 ps equilibration);
7. 30 ion pairs BMIM SCN, 400 K, $(2.134\ \mathrm{nm})^3$, 16.44 ps;
8. eight ion pairs EMIM DCA, 400 K, $(1.311\ \mathrm{nm})^3$, 63.50 ps;
9. eight ion pairs EMIM DCA and two SO_2 molecules, 400 K, $(1.332\ \mathrm{nm})^3$, 59.70 ps;
10. 30 ion pairs EMIM DCA, 400 K, $(2.037\ \mathrm{nm})^3$, 43.98 ps;
11. 30 ion pairs EMIM DCA, 333 K, $(2.011\ \mathrm{nm})^3$, 16.34 ps;
12. 64 ion pairs EMIM DCA, 400 K, $(2.623\ \mathrm{nm})^3$, 4.06 ps (0.5 ps equilibration);
13. 30 ion pairs BMIM DCA, 400 K, $(2.174\ \mathrm{nm})^3$, 15.48 ps;

14. 30 ion pairs BMIM DCA, 600 K, $(2.174\ \mathrm{nm})^3$, 11.74 ps (started from the last timestep of the simulation at 400 K);

15. eight ion pairs MMAN, 400 K, $(1.019\ \mathrm{nm})^3$, 84.02 ps with the DCACP-BP86 setup of the 48 MMAN system; [33]

16. 48 MMAN ion pairs for which 100 snapshots were randomly selected for analysis from the trajectory of Ref. [33] (DCACP-BP86 setup, 400 K, box of 1.8115 nm x 1.9761 nm x 1.7723 nm, 19.35 ps).

Furthermore, the data of a recent 30 MMIM Cl pair simulation [121] and of a simulation of 48 MMAN and four water molecules [125] were analyzed here in order to allow for a broader comparison and the study of dipole moments in water mixtures of ILs. The two larger systems of 48 EMIM SCN ion pairs and 64 EMIM DCA ion pairs were done to test on possible system size dependence of the electrostatic properties, as *e.g.* the distributions of the molecular dipoles or correlation ranges. As up to around 1500 atoms and nearly 4400 electrons were included in these systems, the computational effort was immense and allowed only for short simulation times. Still, there were indications that an equilibrated electron structure was reached at least within the simulation time of the 64 EMIM DCA system. Already, for the initial configurations, taken from a well equilibrated classical simulation, [198] the interatomic forces were smaller than 0.003 a.u. = 0.003 E_h/bohr after a wavefunction optimization. This implied that the initial MD based configuration provided a reasonable overall liquid structure also for the quantum description. As a further test, ten uncorrelated classical configurations of 64 EMIM DCA ion pairs were considered to sample statistically the liquid structure found in the classical MD and possible long time effects. After performing a wave function optimization, the largest force acting on an atom was again below 0.004 E_h/bohr for each of these configurations. In a similar study of ILs in literature, configurations obtained from classical samples connected to forces as high as 0.1 E_h/bohr were considered as equilibrated on the quantum scale. [122] Thus, the classical guess of initial structures seemed very close to the AIMD equilibration state here. Furthermore, the resulting electronic structures of the ten configurations were found to give molecular dipoles obeying the same dipole distribution as found in the short 64 EMIM DCA simulation. Thus, the short simulation time seemed sufficient to sample the decisive electron structure states and to provide a preliminary test of size effects, especially since quantities linked directly to the dynamic properties of the system were not considered for the 48 EMIM SCN and 64 EMIM DCA data.
The dipole moments were calculated using the maximally localized Wannier analysis (see Chapter 2.3.1 and Refs. [146, 199–201]) every 500th timestep. This electron density localization was carried out as implemented in CPMD. In general, DFT and Wannier center based dipole moments were found to be consistent with experimental values for single molecules in the gas phase. [151, 202] Here, the dipole moment of imidazolium ions was calculated with respect to the geometric center of the five imidazolium ring atoms (COR), the dipole moment of all other ions with respect to the geometric center of all atoms (COG). Furthermore, analog analysis was done for other reference centers as the geometric center for the imidazolium cations or the center of mass. Qualitatively, the same trends were found. For clarity, only data based on the above described reference centers will be presented here.

Table 4.1: Cation net charges q_{eff} in units of e obtained *via* Blöchl analysis [198].

No. ion pairs	MMIM Cl	EMIM Cl	EMIM SCN	EMIM DCA	MMAN
≈ 30	0.63±0.13		0.56±0.22	0.67±0.19	0.55±0.29
8	0.64±0.16	0.61±0.16	0.56±0.25	0.70±0.19	0.56±0.27
No. ion pairs		BMIM Cl	BMIM SCN	BMIM DCA	
30		0.62±0.21	0.60±0.24	0.71±0.19	

For 100 snapshots per system, the Blöchl analysis (see Chapter 2.3.3 and Ref. [155]) was done as in Ref. [83] by the group of Prof. Holm. [198] As implemented in the CP2K package [203], an Gaussian plane wave (GPW) approach [204], TZV2P basis sets, and pseudopotentials in the Goedecker-Teter-Hutter format [205, 206] were used with the same functionals as in the corresponding CPMD simulation.
For the IL SO_2 mixtures, some ground state structures were studied for comparison to the bulk phase AIMD simulation: The geometries of the six SO_2 EMIM DCA adducts were optimized as the ion pairs in the previous chapter (see Chapter 3.1), by sequential geometry optimization with increasingly computationally demanding setups, *i.e.* BLYP-D/TZVP, BLYP-D/def2-TZVPP, MP2/TZVP, and finally MP2/def2-TZVPP. The SEN analysis (see Chapter 2.3.5 and Refs. [79–81, 163]) was carried out with the TURBOMOLE 6.2 implementation, the NBO analysis (see Chapter 2.3.4) by the Gaussian 09 program. [207] The spacial distribution function was calculated on basis of the AIMD simulation with TRAVIS. [184]

4.2 Monopoles

The monopole monopole interaction is the first term in the multipole expansion and is expected to dominate the behavior of ions as discussed for ion pairs (see Chapter 3). Furthermore, the assignment of partial charges and, thus, also the net ion charge are crucial in the force field development. Commonly, these parameters of a force field are chosen based on *ab-initio* studies of ground state structure of ion pairs. From a conceptual point of view, it is important to compare such monopole structures to the ones obtained in the liquid phase which is characterized by cooperative and temperature effects. Most force fields are developed for simulation of the bulk phase and their parameters should describe the liquid phase molecular electrostatic properties rather than those of small clusters in their ground state.
In general, the ion net charges found by the Blöchl method were reduced, reflecting the influence of polarization and, possibly, charge transfer. The charge reduction emerged as a general characteristic of ILs and the reduced net charges laid between about 0.56 e for MMAN and EMIM SCN to 0.71 e for BMIM DCA. Hence, the Blöchl method provided a justification of the arbitrarily reduced net charges used in several force fields. [15,53,58,61,63,71,208] The net ion charges in the BMIM ILs increased in the same order as for the EMIM ILs, from 0.60 e for BMIM SCN, 0.62 e for BMIM Cl to 0.71 e for BMIM DCA. In all three cases, the net charge was above the one of the

corresponding EMIM IL.
In fact, the effective net charge of an ion can be linked to the corresponding electronic dielectric constant ϵ_{el} as $\epsilon_{\mathrm{el}} = (\frac{q}{q_{\mathrm{eff}}})^2$ [209] if it is a result of polarization. Then, the difference between the external and internal field can be described by the factor ϵ_{el} or q_{eff}. The molecular dynamics electric continuum (MDEC) theory [210, 211] formalizes this aspect and it was successfully applied to water. [211] Since ϵ_{el} is related to the refractive index n by $\epsilon_{\mathrm{el}} = n^2$, a comparison of the found reduced charges to experimental refractive indices was possible. For instance for EMIM DCA, the reduced charge of 0.67 e at 400 K corresponded to an electronic dielectric constant $\epsilon_{\mathrm{el}} = (\frac{q}{q_{\mathrm{eff}}})^2 \approx 2.2$ which gave a refractive index of $n = \sqrt{\epsilon_{\mathrm{el}}} \approx 1.5$ being in close agreement with the value of 1.49 given by the extrapolation of an experimentally obtained fit function. [212] For BMIM DCA, an electronic dielectric constant of 2.13 was reported for 298 K. [12] The corresponding experimental refractive index of 1.46 at 298 K was lower than that of EMIM DCA of 1.51. [212] Consistently, the net ion charge was higher in BMIM DCA than in EMIM DCA and a refractive index of about 1.40, lower than for EMIM DCA, was obtained for BMIM DCA. BMIM Cl was observed to have a refractive index of 1.55 at 298 K [213] and the net charge based refractive index calculated here was 1.62 at 400 K. Therefore, the refractive index of BMIM Cl was higher than the one of BMIM DCA both in experiments and according to the Blöchl ion net charges. Additionally, the refractive index of EMIM SCN was found to be higher than that of EMIM DCA in experiments, 1.536 at 342 K [214] compared to 1.500 at 400 K for EMIM DCA. [212] Qualitatively, the Blöchl net ion charges predicted also a higher refractive index for EMIM SCN, but the refraction based on a net charge of 0.56 e would be 1.8 and, thus, much too high. This might be due to the fact that the Blöchl method describes not pure polarization effects of separated charges, but also possible charge transfer. This different mechanism also leads to reduced net charges and was observed not only in theoretical studies, [44, 74, 107] but also in experiments. [44, 46, 215] However, the charge transfer found for single ion pairs in their ground state structure was very similar for EMIM SCN and EMIM DCA (see Table 3.1). Thus, this should not explain the differences between the Blöchl net charges with respect to the experimental values. Anyway, experimental values of ϵ_{el} measured by dielectric spectroscopy were also not consistent with experimental refractive indices. [12] The properties of an IL depend crucially on the concentration of impurities and, thus, a quantitative relationship between theory and experiments might not be expected.

The monopole structure fluctuated strongly as the standard deviations of the ion net charges were very high. All net charges were equal within the standard deviation (see Table 4.1). In this sense, the effective electrostatic properties of the cations seemed rather similar independently of the IL's composition. The large variance of the net charge implied that the local situation of the ions differed very much. There seemed to be environments in which the ions were highly polarized and others in which the polarization or charge transport was low. The dependence of the ion net charge on the configuration was already observed for single ion pairs (see Table 3.1 and Refs. [20,84,94,102]). Additionally, the effective monopole structures were the same in the eight ion pairs systems and the larger systems (see Table 3.1). Thus, even though the monopoles varied greatly, the processes evoking this variation seemed rather local, dominated by only the closest neighbors.

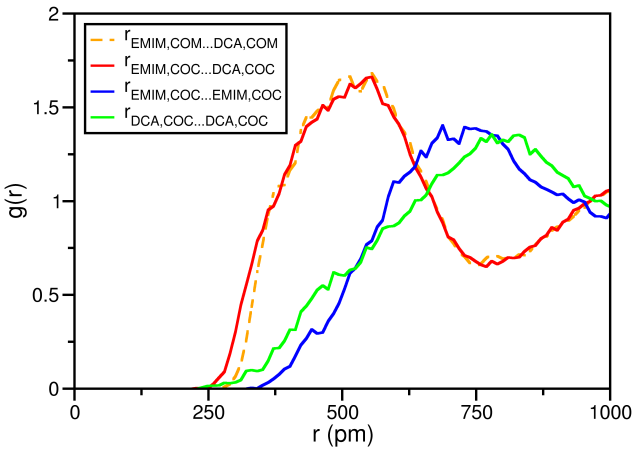

Figure 4.1: Radial distribution function of the distances between the centers of charge $r_{\mathrm{X,COC...Y,COC}}$ of anions and cations (red), cations and cations (blue) as well as anions and anions (green) in the 30 EMIM DCA system at 400 K. For comparison, the RDF of the distance between the centers of mass of anions and cations $r_{\mathrm{EMIM,COM...DCA,COM}}$ is given (orange). The simulation box size was $(2037\ \mathrm{pm})^3$.

As a rule, polarization can be described formally by the translation of the center of charge. [216] Due to bulky shape of the ions, they can arrange in different ways. For instance, the distance between two ions' centers of charge (COC) can vary for ions with the same distance between their centers of mass (COM). If radial distribution functions (RDFs) of these distances are compared, the influence of Coulomb interactions on the mutual orientation can be assessed. As shown in Figure 4.1, distances below 300 pm were more likely for COC distances than for COM distances. This implied that the ions orientated in a way to minimize the charge separation and, thus, maximize the Coulomb interactions. At higher distances, such a difference was not found anymore. Still, a longer range order was found: the anions seemed to be closer to the cations than equally charged ions were to each other as the first maximum in the RDF was at a lower distance. Such an order, however, can be explained solely by excluded volume conditions even if the ions interacted directly only with their nearest neighbors.

In summary, polarization was found to be significant in ILs, giving rise to reduced net charges and a preferred COC distance. The questions arise if the mechanisms leading to such a large variation are the same as in the gas phase (see Chapter 3) and how extended the region is which influences the electrostatic properties of an ion. Theses issues will be addressed in the next chapters.

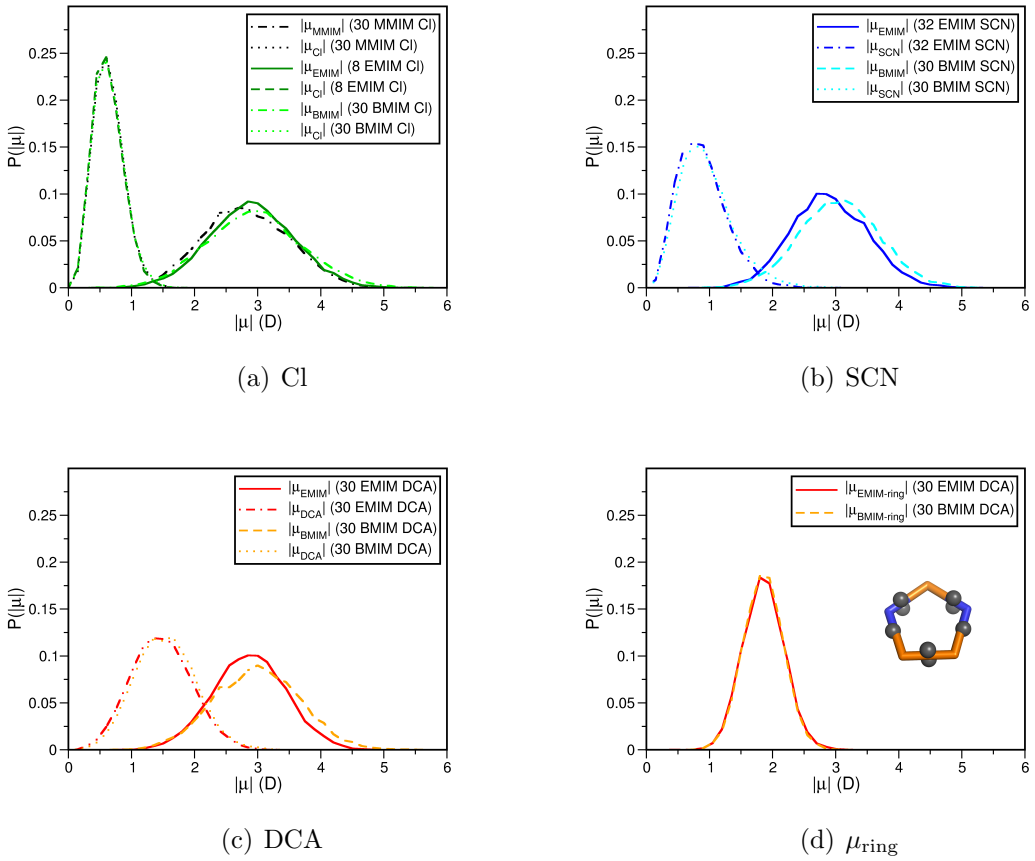

(a) Cl (b) SCN

(c) DCA (d) μ_{ring}

Figure 4.2: Dipole moment distributions for imidazolium IL systems with different sidechain length having as anion (a) Cl, (b) SCN, and (c) DCA. In (d), the dipole moment of the imidazolium ring consisting of five atoms and 10 electrons (see inset) is plotted for EMIM DCA (400 K) and BMIM DCA.

4.3 Dipole moments

In general, the electric dipole moment of an ion is not defined uniquely as it depends on the arbitrary reference center with respect to which it is calculated:

$$\vec{\mu}_{\text{refB}} = \vec{\mu}_{\text{refA}} + q_{\text{ion}}\vec{R}_{\text{refB}\cdots\text{refA}}\,. \tag{4.1}$$

This implies that the absolute value of ionic dipoles does not have a physical quantitative meaning and cannot be determined by experiments. Furthermore, the reference center of an ion can be chosen to be the center of charge (COC) and, then, the dipole moment of the ion is exactly 0. As a consequence, for ions having a charge of 1 and a dipole moment $\vec{\mu}_{\text{refB}}$, the vector $\vec{R}_{\text{refB}\cdots\text{COC}}$ pointing from the center of reference (refB) to the COC is equal to the dipole moment $\vec{\mu}_{\text{refB}}$ as

$$\vec{\mu}_{\text{refB}} = q_{\text{ion}}\vec{R}_{\text{refB}\cdots\text{COC}} \quad (\vec{\mu}_{\text{refA}} = \vec{\mu}_{\text{COC}} = 0)\,. \tag{4.2}$$

Mostly, ions in ILs carry a single charge formally. Hence, in literature, the dipole moment of such ions is also denoted as charge arm [216, 217] instead as dipole moment

Table 4.2: Electronic dipole polarizabilities in bohr^3 of several ions based on B3LYP/def2-TZVP [88].

ion	static	
	isotrop	anisotrop
Cl	10.25	0.00
SCN	38.60	36.94
DCA	45.22	48.45
NO_3	23.72	15.58
MMA	19.27	2.32
MMIM	65.66	35.17
EMIM	77.64	39.16
BMIM	101.99	37.71

in order to avoid misleading associations. Obviously, the ionic dynamics are sensitive to the distance between the COC and the COM. [217] An external electric field will produce a torque on an ion as well as imparting a net impulse to the ion's COC. Consequently, this charge arm (or dipole moment for single charged ions) with respect to the COM appeared *a-priori* to be relevant to dynamical properties as viscosity or solvation dynamics. [217] It couples the rotational motion to Coulomb interactions. [218] The charge arm is said to not affect the total strength of the interactions which remains solely dependent on the distance between the COC. [218]
In this work, the dipole moment shall be employed to describe the molecular electronic structure rather than dynamical aspects. Thus, not the COM is chosen as reference center for the rather large and asymmetric imidazolium ions, but the geometric center of the imidazolium ring (COR). The imidazolium ring is the most polarizable part of the cation and the COC of the whole ion is also close to the imidazolium ring, normally somewhere near the N-C^2-N part. Especially, with increasing sidechain length, the position of the COM changes significantly while the COR is unchanged and the COC is shifted only slightly. Hence, the COR is an adequate reference center to study the dipole moment as indicator for the overall charge distribution or displacement. Moreover, the dipole moment, being a vector, is also an indicator of local molecular packing. In this way, it sums up electronic and steric influences and describes the interplay of charge and shape. Hence, it represents a suitable descriptor for the variation of the ion's electrostatic properties upon local liquid configurational changes. Additionally, the evaluation of dipole correlations along the whole system provides information about the effective range of electronic interactions.

4.3.1 Fluctuations

In general, the dipole moment distributions were found to be very broad for several ILs including a protic one. This can be interpreted as the result of a highly fluctuating electronic structure of the ions. In particular, the dipole moment distributions

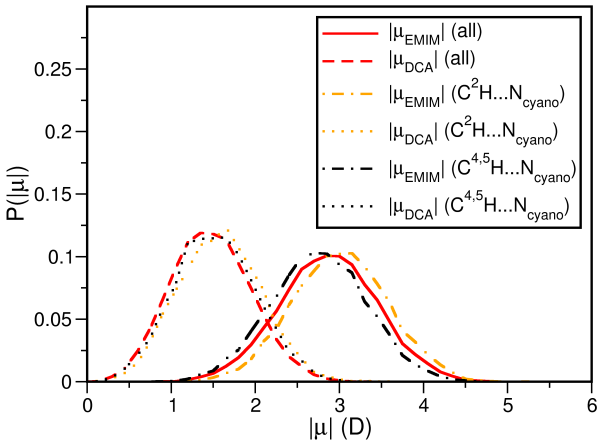

Figure 4.3: Dipole moment distributions of all ions (red) and hydrogen bonded ions (purple and orange) in 30 EMIM DCA (400 K). The chosen hydrogen bond cutoffs were a distance $r_{\mathrm{C^2\cdots N_{cyano}}}$ below 350 pm and an angle $\alpha_{\mathrm{H-C^2\cdots N_{cyano}}}$ below 30 °.

were broader than the dipole moment distribution of a non IL like water. [151] Figure 4.2 gives the dipole moment distributions of MMIM Cl, EMIM Cl, EMIM SCN, EMIM DCA, BMIM Cl, BMIM SCN, and BMIM DCA. The dipole moment distribution of MMAN is shown in Figure 4.5 (d). The dipole moment distribution of the 30 MMIM Cl system was consistent with literature. [120, 121]

In all imidazolium based ILs, the cations MMIM, EMIM, and BMIM had essentially the same dipole moment distribution (see Figure 4.2). The differences were mainly due to the influence of the sidechain orientation as the dipole moment of the whole ion changed significantly depending on the sidechain orientation. If for one specific cation the relative positions of the Wannier center and, hence, the electronic structure were kept as found in the liquid phase simulation and only the sidechain was rotated artificially, the dipole moment of this cation varied by 2 D (see Figure A.1). If only the most polarizable part, the five imidazolium ring atoms and the corresponding ten Wannier centers, was considered, its dipole moment μ_{ring} was found to be independent of the length and orientation of the sidechain (see Figure 4.2 (d)): These dipole moment distributions of the imidazolium cation rings in EMIM DCA and BMIM DCA were found to be identical. Also, the anions' dipole moment distributions did not depend on the sidechain length of the counterion (see Figure 4.2 (a) to (c)). Thus, the influence of the sidechain on the general electronic structure seemed to be small if changing from MMIM or EMIM to BMIM.

If, instead of the cation, the anion was varied, the effect on the counterion's dipole moment distribution was slightly higher. For instance, in EMIM DCA, the EMIM dipole moment distribution was less broad than in EMIM Cl while the mean dipole moment varied only by 0.03 D (compare Figure 4.2 (a) and (b) as well as Table A.2). The same is true for BMIM DCA and BMIM Cl, for which the standard deviation was about 0.13 D larger than for BMIM DCA. It may be concluded that the anion seemed to have a larger influence on the electrostatic properties of imidazolium based ILs

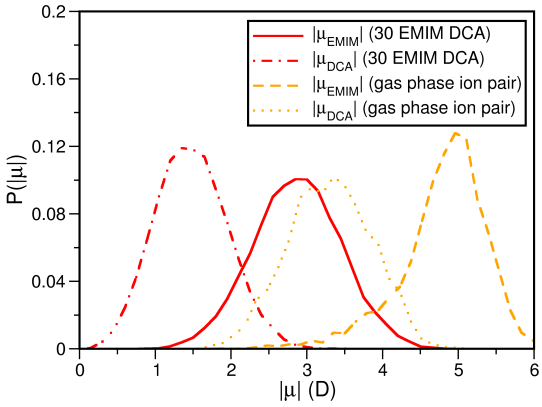

Figure 4.4: Dipole moment distribution of 30 EMIM DCA ion pairs in the liquid phase (red) compared to the one of one EMIM DCA ion pair in the gas phase (orange, see Chapter 3.1). The temperature was in both cases 400 K.

than the specific cation. The dipole moment distributions of the anions themselves were rather different which is easily explained as the anions differ structurally much more than the imidazolium based cations.
The spread of dipole moment distribution is a measure of the adaptability of the electronic structure of an ion. The gas phase polarizability is also a quantity which describes this property. In this way, a connection between the two quantities might be possible. If such a correlation existed, the cooperative interplay of the liquid phase would not have a decisive influence. Roughly, the spread of the distributions increased with the increasing size of the anion and an increasing polarizability, at least for the imidazolium based ILs. However, the polarizability of Cl was about 25 % of that of SCN (see Table 4.2 and Figure 4.5), the spreads of distributions differed about 50 %. For SCN and DCA, the difference in the spread of the distribution and the polarizability were both about 15 %. Thus, there seemed to be no direct quantitative relationship. Furthermore, the polarizability of NO_3 was smaller than the one of SCN while the dipole moment distribution was much broader. The counterion of NO_3 was not an imidazolium cation, but MMA which had a much lower polarizability while having a slightly higher mean dipole moment than EMIM. The imidazolium cations had very similar dipole moment distributions despite their considerable deviating gas phase polarizabilities. Hence, it appeared that the gas phase polarizabilities were not a good estimator for the width of the molecular dipole moment distributions in liquid phase. This means that all these systems were characterized by strong electrostatic fluctuations depending on the complex balance between steric and electronic interactions in the IL's liquid phase. The question arising is what caused the fluctuations.

These large fluctuations were found to be the product of very local, but diverse molecular packing. Similar to the findings for net ion charges in ion pairs (see Section 3), the mean dipole moments of EMIM cations involved in a hydrogen bond at the most acidic C^2H proton were higher than the dipole moments of other cations (see Figure 4.3). The same occurs also for the anion dipole moments. Thus, this

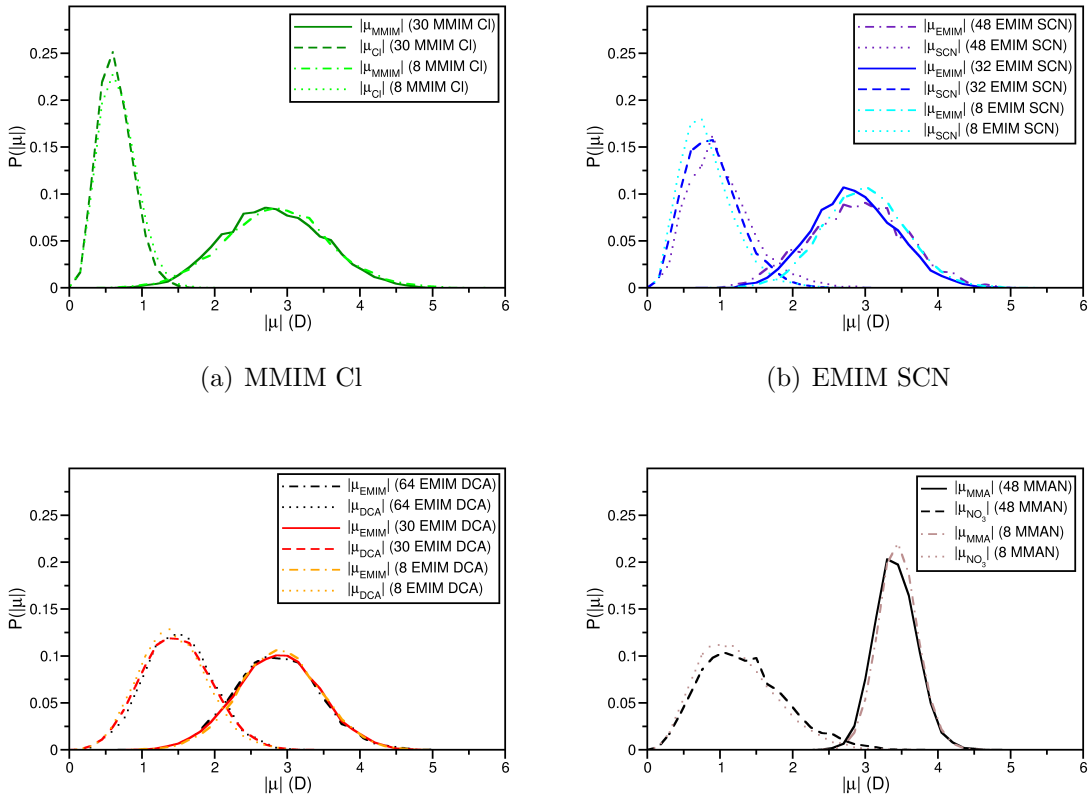

(a) MMIM Cl

(b) EMIM SCN

(c) EMIM DCA

(d) MMAN

Figure 4.5: Dipole moment distributions for large ($\geq$ 30 ion pairs) and small (eight ion pairs) IL systems of (a) MMIM Cl, (b) EMIM SCN, (c) EMIM DCA (400 K), and (d) MMAN.

hydrogen bond was connected to an additional polarization. If the cation formed a hydrogen bond *via* a C^4H or C^5H hydrogen, its mean dipole moment was slightly decreased. That is easily understandable as the dipole moment of the cation pointed approximately in the direction of the C^2 carbon. The additional polarization by a C^4H or C^5H hydrogen bond was in the opposite direction and the absolute dipole moment decreased. The dipole moment distribution of anions forming a C^4H or C^5H hydrogen bond were less shifted to higher values than the one of anions bonding to the C^2H hydrogen. This is in agreement with the lower acidity of the C^4H or C^5H hydrogen atoms. While the mean dipole moments of hydrogen bonded ions were slightly changed, the dipole moment distribution stayed as broad as the distribution of all ions. This implied that while these hydrogen bonds provided a preferential tendency to change the ion's dipole moment, the environment was still dominant in determining the width of the dipole moment distribution. In contrast to hydrogen bonding, neither the overall numbers of close cations or anions nor the magnitude of dipole moments of adjacent ions did have influence on the dipole moment distribution of an ion. Hence, specific interactions seemed decisive even though a simple two ion interaction as a hydrogen bond did not dominate all other interactions with the

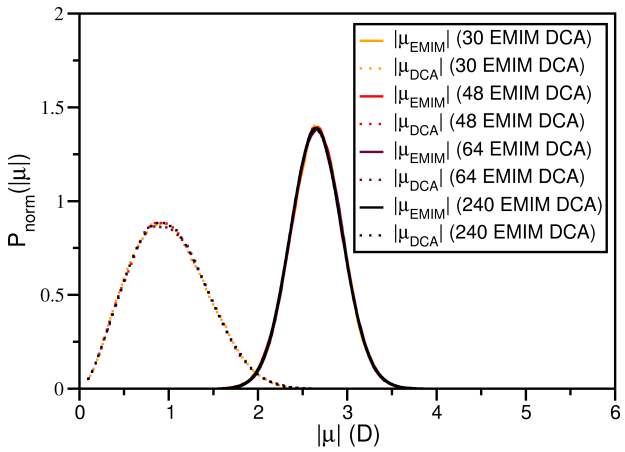

Figure 4.6: Dipole moment distributions based on rescaled Blöchl partial charges from classical simulations for EMIM DCA systems of different size ranging from 30 ion pairs to 240 ones at 400 K. [198]

close neighbors. The importance of the whole close environment was also visible in the great difference of the dipole moment distribution of EMIM DCA in the liquid and the gas phase (see Figure 4.4). The dipole moments of the gas phase ion pair were much higher which was connected to the strong occupancy of the C^2H hydrogen bond position (compare Chapter 3.3). Also, the variance between the highest and lowest absolute dipole moment was larger in the gas phase. While, in general, the large spread seemed intrinsic to ILs and their electronic properties, the actual dipole moment distributions were very sensitive to the specific ion's environment. The range of the effective interactions will be discussed next.

4.3.2 Locality

The dipole distributions of the large systems of at least 30 ion pairs and their thermodynamical equivalent systems of eight ion pairs were the same in all cases as shown in Figure 4.5. For MMIM Cl, this was already found in literature. [107,119] Eight ion pair systems seemed about the smallest that might still capture liquid like behavior. Their box size of about $(1.3\ \mathrm{nm})^3$ was so small that any ion was only surrounded by its first neighbors. Ions further away were already periodic images. As the dipole distributions were not altered in these very small systems, an ion seemed to be influenced only by its immediate neighbors and to not experience perturbations from the long range behavior of the liquid. The high locality would strongly support the idea of ions rattling in a long-living ion cage. [8,13,15,33,37,53,55,74,107,219] In the literature, [72,220,221] the counter ions in the first shell were reported to overcompensate the charge of an ion, showing overscreening. [72,220,221] That implied that ions further away did not interact directly with the central ion, but rather with the

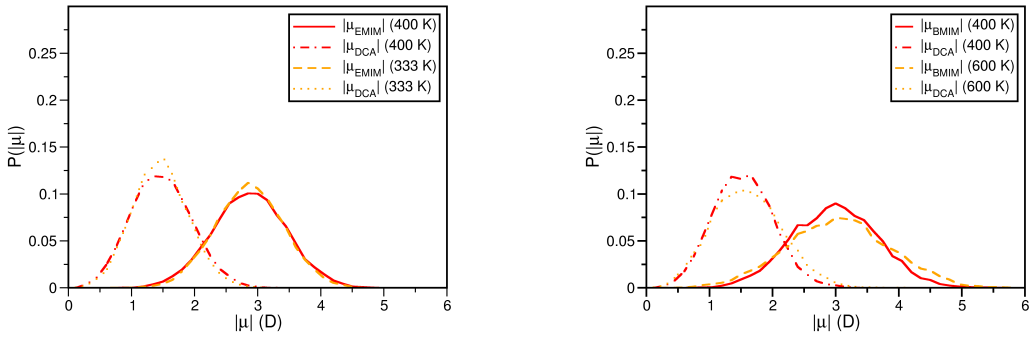

(a) EMIM DCA (b) BMIM DCA

Figure 4.7: Dipole moment distributions in (a) 30 EMIM DCA at two temperatures 400 K (red) and 333 K (orange) and (b) 30 BMIM DCA at two temperatures 400 K (red) and 600 K (orange).

overscreened charge. Locality would be high as was found.
However, the system sizes of about 30 ion pairs themselves might show strong system size effects and miss decisive configurations. Indeed, the box lengths were below the distance at which the RDFs went to unity. So, short simulations of larger systems of 48 ion pairs EMIM SCN and 64 ion pairs EMIM DCA, which did not suffer from this limitation, were conducted. The obtained dipole moment distributions were in good agreement with the of the smaller systems (see Figure 4.5). To further ensure the significance of the AIMD based results, ten uncorrelated configurations of 64 EMIM DCA were chosen in 1 ns intervals from the last 10 ns of a classical MD trajectory of 40 ns. In such a long simulation, processes not present in few ps can be sampled. The dipole moment distribution found after wavefunction optimization on these configurations agreed with the one found in the AIMD simulations. Again, this implied that the time and size of the AIMD studies were sufficient to sample all decisive configurations for the molecular electrostatic properties. Significantly larger system sizes can only be studied by classical MD. There as well, the dipole moment distributions obtained based on partial charges were independent of the system size in a range from 30 ion pairs to 240 ones (see Figure 4.6). Hence, there was strong evidence for the high locality of molecular electrostatic properties which will be further strengthened in Chapter 4.4.
Furthermore, it was found that short simulation times provided a sufficiently exhaustive representation of the electrostatic properties for any of the studied ILs and, thus, the molecular electrostatic properties were also local in time. A simulation time of only 3 ps sampled a dipole moment distribution similar to the one obtained from much longer runs as shown for EMIM DCA in Figure 4.8. Indeed, it was reported that 50 % of the entire relaxation happened on a subpicosecond time scale. [14, 107] At these times, the anion relaxed and fluctuated around the cation showing ion cage dynamics. As the molecular electrostatic properties were local in space, they should fluctuate on exactly this fast time scale. Hence, the locality in space might bring the locality in time.
Moreover, the dipole moment distribution did not depend on changes in temperature

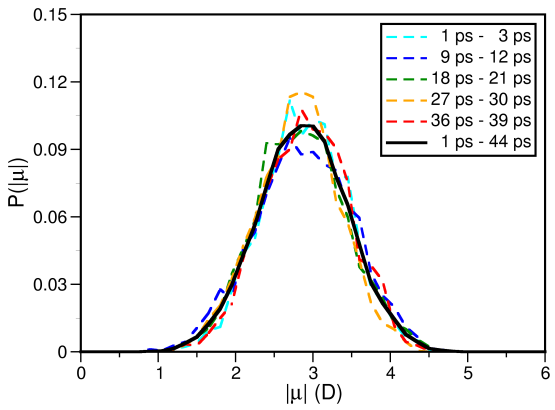

Figure 4.8: Dipole moment distributions in 30 EMIM DCA at 400 K averaged over the whole simulation (black thick) and over 3 ps intervals (colored thin).

within a range of 333 K to 400 K or 400 K to 600 K. The dipole moment distributions of liquid phase EMIM DCA at 333 K were only slightly narrower than those at 400 K (see Figure 4.7 (a)). This seemed to be due to less energetic vibrations associated with smaller mean bond lengths. The dipole moment distributions of BMIM DCA at 600 K were broader in agreement with the more energetic vibrations related to larger mean bond lengths. Hence, the electronic structure appeared to be rather insensitive to the temperature change. As a result, on one hand, CPMD calculations can be performed at higher temperature in order to explore faster a larger portion of the phase space. On the other hand, force fields might be transferable with respect to the thermodynamic state point.
In conclusion, the molecular electrostatic properties of ions in the liquid phase emerged to be rather local in space and time. At least for the ILs studied here, it seemed appropriate to carry out AIMD simulations that are restricted to a small number of ion pairs and a short time in order to obtain partial charges. Moreover, these simulations can be done at higher temperature and, thus, sample faster the phase space without a significant change in the observed electrostatic properties, at least for the systems studied herein. All three specifications, the small size, short time and high temperature, enable a relatively effortless study of the molecular electrostatic properties on the *ab-initio* scale.

4.4 Correlations

To further test the notion of locality, the ranges of correlations of two types of electrostatic interactions, monopole dipole and dipole dipole, were studied. Simple interionic radial distribution functions would not capture the electrostatic effects as they are dominated by excluded volume interactions as discussed in Chapter 4.2. For the monopole dipole correlation, the angular distribution between the dipole of an ion and the vector from the ion's center of reference to another ion's center of charge (COC)

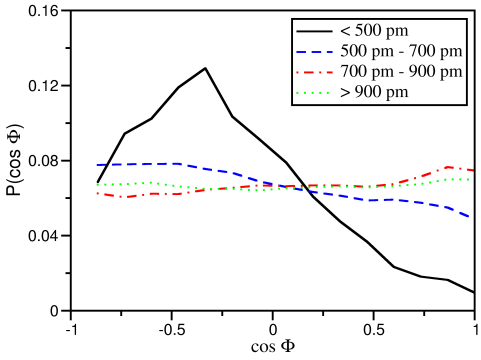

(a) monopole dipole

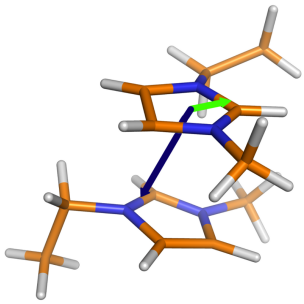

(b) $\vec{r}_{\mathrm{COC\cdots COC}}$ vs. $\vec{\mu}$

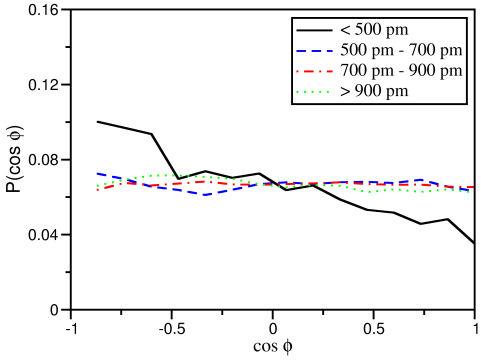

(c) dipole dipole

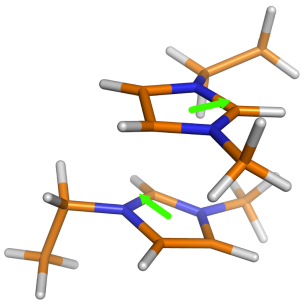

(d) $\vec{\mu}$ vs. $\vec{\mu}$

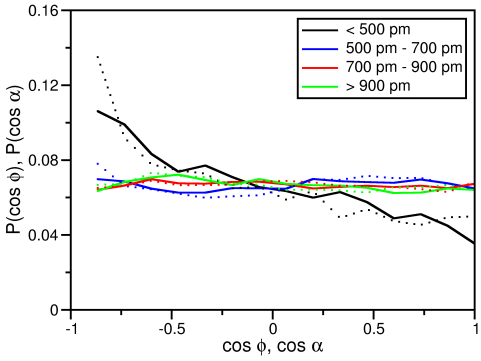

(e) $\vec{\mu}_{\mathrm{ring}}$ (straight), $\vec{r}_{\mathrm{COR\text{-}C^2}}$ (dotted)

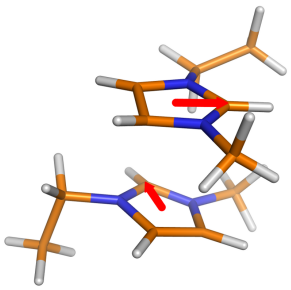

(f) $\vec{r}_{\mathrm{COR\text{-}C^2}}$ vs. $\vec{r}_{\mathrm{COR\text{-}C^2}}$

Figure 4.9: Angular probability distribution of (a) cos Φ (monopole dipole), (c) cos ϕ (dipole dipole) and (d) cos φ (μ_{ring}-μ_{ring}) (straight) and cos α ($\vec{r}_{\mathrm{COR\text{-}C^2}}$-$\vec{r}_{\mathrm{COR\text{-}C^2}}$) (dotted) of cations separated by distances below 500 pm (black), from 500 pm to 700 pm (blue), 700 pm to 900 pm (red), or above 900 pm (green) in the 30 EMIM DCA system at 400 K. In (b), (d), and (f), the vectors are illustrated.

was considered, *e.g.* taking one cation per time as reference:

$$\cos\Phi = \frac{\vec{\mu}_{\text{cat}}^{\,\text{ref}} \cdot \vec{r}_{\text{cat}}^{\,\text{shell}_i}}{|\vec{\mu}_{\text{cat}}^{\,\text{ref}}| \cdot |\vec{r}_{\text{cat}}^{\,\text{shell}_i}|} \,. \tag{4.3}$$

$\vec{\mu}_{\text{cat}}^{\,\text{ref}}$ is the dipole of the reference cation while $\vec{r}_{\text{cat}}^{\,\text{shell}_i}$ is the vector from the COR of the reference ion to the COC of cations in the $i-th$ radial bin ($i = 1$: below 500 pm, $i = 2$: 500 pm to 700 pm, $i = 3$: 700 pm to 900 pm, $i = 4$: above 900 pm). All possible distributions were calculated: $\vec{\mu}_{\text{an}}$-$\vec{r}_{\text{an}}$, $\vec{\mu}_{\text{an}}$- $\vec{r}_{\text{cat}}$, $\vec{\mu}_{\text{cat}}$-$\vec{r}_{\text{an}}$, and $\vec{\mu}_{\text{cat}}$-$\vec{r}_{\text{cat}}$. Analogous, all possible dipole dipole angular distributions as $\vec{\mu}_{\text{an}}$-$\vec{\mu}_{\text{an}}$, $\vec{\mu}_{\text{cat}}$- $\vec{\mu}_{\text{an}}$, and $\vec{\mu}_{\text{cat}}$-$\vec{\mu}_{\text{cat}}$ were studied as in Ref. [121], *e.g.*:

$$\cos\phi = \frac{\vec{\mu}_{\text{cat}}^{\,\text{ref}} \cdot \vec{\mu}_{\text{cat}}^{\,\text{shell}_i}}{|\vec{\mu}_{\text{cat}}^{\,\text{ref}}| \cdot |\vec{\mu}_{\text{cat}}^{\,\text{shell}_i}|} \tag{4.4}$$

in which $\vec{\mu}_{\text{cat}}^{\,\text{shell}_i}$ is the dipole of cations in the $i-th$ radial bin.
As examples, $\vec{\mu}_{\text{cat}}$-$\vec{r}_{\text{cat}}$ and $\vec{\mu}_{\text{cat}}$-$\vec{\mu}_{\text{cat}}$ of the 30 EMIM DCA system are given in Figure 4.9 (a) and (c). Basically, a correlation of the dipole of a cation to both the direction to the COC and the dipole of cations was observed only in the very immediate neighborhood while no preferential alignment was displayed beyond this short range. All other distributions gave the same qualitative picture for any studied IL, also the non-imidazolium based MMAN. For the cation anion and the anion anion dipole dipole angular distributions, only a negligible preferential order was observed even in the first radial bin while the correlations of the dipoles and the COC directions decayed slower. In any case at distances above 800 pm, there was no preferential alignment in any of the distributions. A distance of 800 pm matched approximately the molecular size of the imidazolium ion. Hence, any correlation decayed within one molecular length.
The observed behavior at distances below 500 pm seemed not closely connected to electrostatic interactions, but was influenced more by packing. If the cations' centers of ring were close together, for instance, less than 400 pm, then the cations have to be in a stacked conformation. Such spacial ordering of the cationic imidazolium rings can be described easily by the angle between the vector $\vec{r}_{\text{COR-C}^2}$ of two cations. The polarization of a cation by other ions changes mainly the charge distribution in the imidazolium ring. The correlations of the dipole moments of only the imidazolium ring should show the possible mutual polarization more clearly as the correlations of the dipole moments of the whole cation as these were influenced by the orientation of the sidechain (see Chapter 4.3.1, Figure 4.2 (d) and Figure A.1). Thus, in order to tell the difference between mutual polarization and packing, the angular distributions of the angles between $\vec{r}_{\text{COR-C}^2}^{\,\text{cat 1}}$ and $\vec{r}_{\text{COR-C}^2}^{\,\text{cat 2}}$ (dotted) and between $\vec{\mu}_{\text{ring}}^{\,\text{cat 1}}$ and $\vec{\mu}_{\text{ring}}^{\,\text{cat 2}}$ (straight) were compared in Figure 4.9 (e). For small distances between the cations, there was a difference between the two angular distributions. The cations were more likely to align anti parallel than parallel for both angles. If the cations polarized each other mutually and their ring electrons localized according to this, their dipole moments should tend to be more anti parallel than their spacial orientations. However, that was not evident in Figure 4.9 (e). This might either hint to other important impacts on the dipole moment or to too few statistics. As the angular distribution

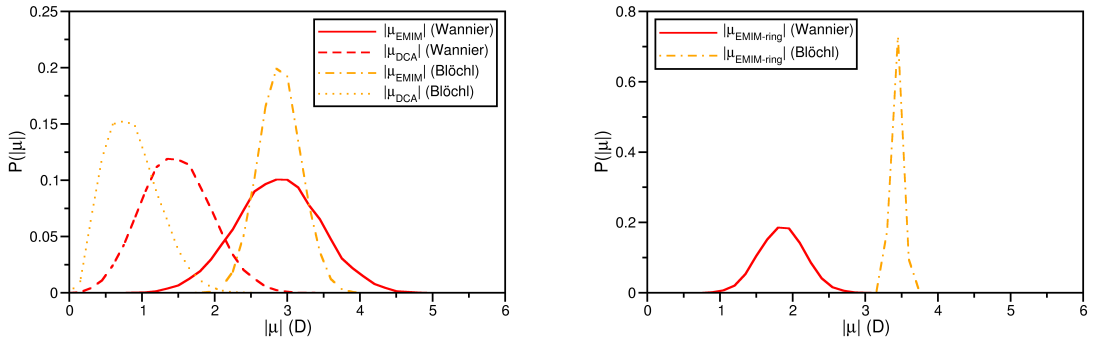

(a) μ (b) μ_{ring}

Figure 4.10: Dipole moment distribution obtained with rescaled Blöchl partial charges (orange) compared to the Wannier center based dipole moment distributions (red) of 30 EMIM DCA (400 K): (a) for the whole ions and (b) for only the imidazolium ring.

at distances below 500 pm was very different for the studied ILs and an uniform distribution was found in the larger classical MD simulation, an insufficient sampling was likely for these very small distances. The diffusion in ILs is very slow and, so, the angular distribution at distances below 500 pm seemed not significant. However, for larger distances, the ions showed neither steric more electronic preferred conformations consistently in all studied systems. Thus, the missing order in the dipole moment might be linked to the missing order in the cation arrangement. Hence, the electrostatic interactions did not dominate the IL structure at distances above one molecular size and an effective long range correlation was not found.

4.5 Polarization

In general, the molecular dipole moment can change due to two mechanisms: electronic polarization and atomic motion. Electronic polarization, which is also denoted as atomic or distortion polarization, means that the electronic structure is deformed by present electric fields and the charge distribution is altered. Independently of the presence of electric fields, the motions of atoms, *e.g.* vibrations, influence the dipole moment without changing the charge distribution. Hence, the dipole moment variation due to atomic motion can be described in a classical MD simulation with a force field having fixed partial charges. In contrast, simulations based on non-polarizable force fields cannot reproduce electronic polarization. Thus, the proportion of electronic polarization in the strong dipole moment fluctuations should be evaluated in order to estimate if polarizable force fields might be necessary for a correct description of the electrostatic properties of the ions in an IL.

The comparison of dipole moment distributions based on Wannier centers and on a partial charge set allows to rate the impact of electronic polarization. For the simplest case of an anion as the monoatomic chloride, a classical point charge representation

has always a zero dipole moment while the quantum based approaches found a non-zero dipole moment for chloride in clusters [84] as well as in the liquid phase (see *e.g.* Figure 4.2 (a)). Thus, it may be important to include polarization in the classical force field to reproduce the correct electrostatic properties for the chloride anion. More relevant is the case of the larger ions. For these, a broad dipole moment distribution might be caused mostly by internal vibrational degrees of freedom and, therefore, by atomic motion only. If this is the case, dipole moments based on point charges should reproduce reasonably well the Wannier center based dipole moment distribution of the quantum chemical calculations. If there is no possibility to reproduce the dipole moment distribution by a set of partial charges, it means that the quantum scale plays a key role in determining molecular electrostatic properties.
Indeed, the broad dipole moment distributions of imidazolium ions were found to be to about 50 % of electronic origin as the width of the dipole moment distributions based on rescaled Blöchl partial charges (see Chapter 2.3.3) was about 50 % less as shown in Figure 4.10. The rescaled Blöchl charges were used to calculate the dipole moments of the configurations from the AIMD simulation for which the dipole moments were calculated by the Wannier center analysis, *i.e.* the same ion configurations were sampled. The cation dipole moment distribution based on the rescaled Blöchl charges had the same mean value even though being less spread (see Figure 4.10 (a)). For anions, the dipole moments based on Wannier centers were on average higher than the one of the Blöchl charges. Thus, the fixed Blöchl partial charge set failed in reproducing the *ab-initio* based dipole moment distributions. But there might be a different set of partial charges which could describe the correct width of the dipole moment distribution and the correct ion net charge.
This can be decided by studying highly polarizable molecular molecular parts like the imidazolium ring. The aromatic imidazolium ring is not only the most polarizable part of the imidazolium cation, also it does not have many vibrational degrees of freedom which could cause broad dipole moment distributions in partial charge systems. Nevertheless, in the case of dipole moments based on Wannier centers, the imidazolium ring was characterized by considerable fluctuation of the corresponding dipole moment (see Figure 4.10 (b)). This could not be reproduced by partial charges. It might be possible to assign partial charges in a way that the dipole moment distribution of the whole cation is as broad as the one based on Wannier centers. But the width of the dipole moment distribution of the imidazolium ring itself can not be reproduced by any partial charge set which shows that electronic polarization played a key role. This implies that polarizable models would be needed to model this effect at classical level. [55, 57, 64–66, 69, 72, 222]
In summary, electronic polarization was shown to be decisive for the electrostatic properties of ions in the liquid phase. However, the electrostatic properties were found to be rather local as discussed in Chapter 4.3.2 and [72, 223]. As a consequence, the explicit inclusion of polarization in the force field and the detailed reproduction of the local quantum behavior might not be necessary for large scale properties. Bulk and long time properties, as density fluctuations or diffusion behavior, might require only an effective model describing the average electrostatic situation found at quantum level. However, the so far discussed dipole moment distribution proved only the existence of polarization, but the mechanism was not revealed. Nevertheless, it might be interesting to further study how polarization arose on a molecular level.

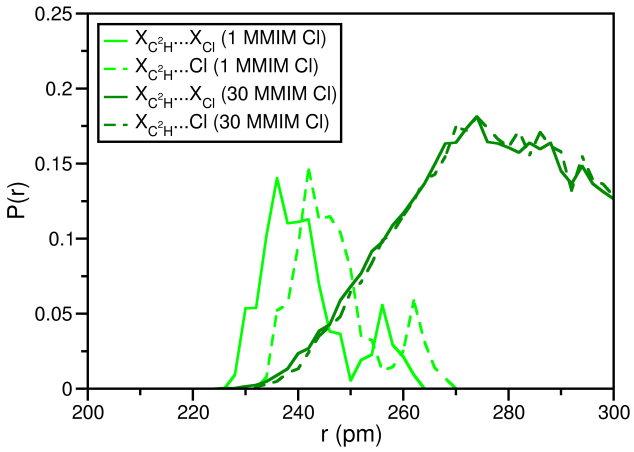

Figure 4.11: Probability distribution of the distance between the Wannier centers of the cation C^2H bond and the chloride atom (dashed) and the distance between the Wannier centers of the cation C^2H bond and the geometric center of the four chloride Wannier centers (straight) in the bulk liquid (dark green) and for one ion pair in the gas phase (light green). For the liquid, the probability distribution was multiplied by 200 for an easier comparison. The simulation box size was about $(2000\ \text{pm})^3$.

For instance, there could be ion conformations which were especially decisive for an ion's polarization. In Chapter 4.3.1 (see Figure 4.3), hydrogen bonding was shown to be such a conformation. In this work, several approaches were tested in order to shed light onto the polarization mechanism. Overall, the results were rather hard to interpret as polarization seemed to be an intrinsically many-body process. In order to shown what was done, two examples are presented next.
Another way to visualize the influence of polarization is to compare the probability distributions of the distance between Wannier centers to other Wannier centers and the distance between Wannier centers and atoms. An example in which the deviations between such distributions can only be explained by polarization is shown for MMIM Cl in Figure 4.11. The difference between the C_2H Wannier center – Cl Wannier center distance and C_2H Wannier center – Cl atom distance probability distributions was small for the liquid phase (dark green lines in Figure 4.11). Only, the probability of Wannier center – Wannier center distances below 260 pm was higher at than for the Wannier center – atom distance. This corresponds to the expected polarization effects for hydrogen bonds [187] in which electron density is shifted from the Cl ion towards the C^2H hydrogen. Additionally, the light green lines in figure 4.11 give the same probability distribution for a monomer in the gas phase at 200 K in which the anion was in a similar position relative to the cation as in the bulk for distances below 260 pm. The minimal distances between Wannier centers observed in the gas phase monomer were significantly lower than the ones in the liquid phase as, in the liquid phase, any ion interacted with several others and, thus, the directionality of the effective interactions was lost. Also, the Wannier center – Wannier center

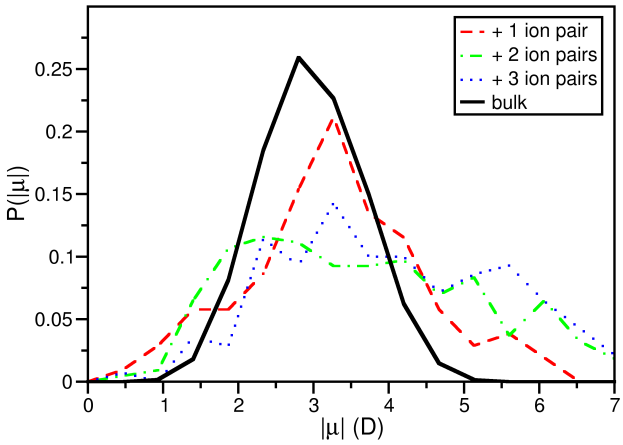

Figure 4.12: Distribution of the central cation's dipole moment in all possible one ion pair combinations (red), two ion pairs ones (green), and three ion pairs ones (blue) compared to the general cation dipole moment distribution in bulk MMIM Cl (black). The chosen timestep is 747 and the central cation is cation 6. Ions with minimal atom-atom distances to the central cation below 400 pm are considered for the one ion pair configurations, below 320 pm for two ion pairs, and below 310 pm for three ion pairs.

distance was much shorter than the Wannier center – atom distance due to the strong mutual polarization of just two ions in the gas phase.

To further understand the molecular mechanism of polarization, it would be interesting to know which neighbor ions have the largest influence on the polarization and, hence, the dipole moment of an ion or how large clusters have to be in order to reproduce the correct dipole moment of a central ion. This would give further insight into the range of locality of the electrostatic properties. One approach was to study larger clusters of ions in their ground state structure. [94] However, in these, the ions might adapt conformations not representative of the liquid phase as the intermolecular distances might be smaller (compare Chapter 3). Also, the electrostatic properties of ions at the surface of these clusters should differ from the ones of ions in a continuous phase. Indeed, the dipole moment distribution found in clusters as large as eight ion pairs differed from the one of the liquid phase as much as the of two ion pair clusters. [94] Still, the electrostatic properties of two ion pairs were considerable more similar to the ones in liquid phase than the ones of isolated ions or one ion pairs. [84, 94] In order to avoid the above mentioned obstacles, clusters were studied in the coordinates taken from snapshots of the liquid phase AIMD simulation and only the dipole moment of the central ion was considered. The dipole moment of this central ion could be pictured as the sum of dipole moments which the ion would have if it interacted only with some of the neighbor ions. If all possible combinations of ions were taken into account, the superposition of all corresponding dipole moments might be the dipole moment observed in the liquid phase. For one example, the results obtained following this idea are given in Figure 4.12. The number of considered

ion combinations was increased by increasing a cut-off distance $r_{\text{most distant ion}}$. In this way, only ions having minimal intermolecular atom atom distances below $r_{\text{most distant ion}}$ were used to generate ion pair combinations around the central ion. The dipole moment distribution of the central ion surrounded by only one ion pair was broader than that of cations in the liquid phase (see Figure 4.12). In the cluster, the central ion was characterized by dipole moments not found in the liquid phase. If the size of the cluster was increased and two or three ion pairs surrounded the central cation, the dipole moment distributions became even broader. Thus, the central ion's dipole moment distribution was much more spread in the clusters than in the liquid phase. For three ion pairs, very high dipole moments not present in the liquid phase were even more likely than for one ion pair clusters. Thus, the expectation that larger clusters reproduce the central ion's dipole moment better was not confirmed probably due to cluster surface effects. If more ion pairs were considered, the results might improve. Disregarding other concerns, the study of clusters larger than a central ion and three ion pairs was not possible within this approach as the number of combinations to be considered increased too fast. However, the relationship between an ion's dipole moment and its environment was not simple and these cluster based studies seemed to have hardly potential to be instructive.

4.6 Dipole moments in mixtures

It is important to know how the electronic structure changes in mixtures as force fields should be applied not only to neat liquids, but to mixtures. For this, a systematic understanding of how the electrostatic molecular properties change and how the force field parameters might need to be adjusted is highly beneficial. It was found that the agreement between classical MD and experiments of water IL mixtures was higher if the dipole moment of water was decreased with respect to force fields developed for neat water. [224] Experimentally, it was observed that the dielectric properties of water protic IL mixture resembled the properties of neat ILs. [225] This is consistent with the MDEC theory. [210, 211] However, a more molecular based understanding would be helpful and, therefore, the dipole moments of the molecules in a mixture of 48 MMAN ion pairs and four water molecules were analyzed and compared to the neat liquids.

The dipole moment distributions of the IL ions remained as in the neat IL (see Figure 4.13 (a)). This might be due to the excess of IL ions. However, also ions hydrogen bonded to a water molecule were characterized by dipole moment distributions only slightly changed. The cation was more polarized whereas the mean dipole moment of the anion was slightly decreased. The influence of water on the cation was stronger which was consistent with the stronger hydrogen bond formed between cations and water compared to anions and water. [125] The small impact on the dipole moment distributions might be due to the fact that even in neat MMAN, most ions were involved in at least one hydrogen bond at another ion. [33]

Compared to neat water, the dipole moment distribution of water was shifted to a significantly lower mean value (see Figure 4.13 (b)). Thus, water was effectively depolarized. This was in agreement with the in average lower number of hydrogen bonds

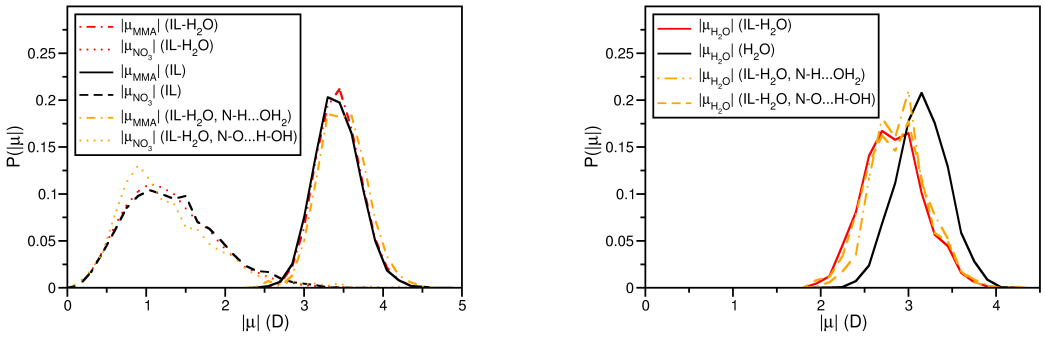

(a) ions (b) water

Figure 4.13: Dipole moment distributions of (a) MMAN in neat MMAN (black), in a water MMAN mixture (red) and of MMA and NO_3 ions forming a hydrogen bond to water in the water MMAN mixture (orange). In (b), the dipole moment distributions of water in neat water (black), in the water MMAN mixture (red) as well as water forming either a hydrogen bond to MMA or to NO_3 in the water MMAN mixture (orange) are given. The chosen hydrogen bond cutoffs were a distance $r_{C^2\cdots N_{cyano}}$ below 350 pm and an angle $\alpha_{H-C^2\cdots N_{cyano}}$ below 30 °.

each water was involved in, 1.85 compared to 3.22 in neat water. [125] Overall, the effect of many ions gave less overall polarization than the more or less tetrahedral structure of uncharged water molecules. Probably, the directionality of the interaction was more decisive than the amount of charge. [125] Furthermore in ILs, the charges were screened and many polarization effects might superimpose. If water was hydrogen bonded to at least one IL ion, the mean dipole moment of water was increased slightly more when bonded to a cation than to an anion (see Figure 4.13 (b)). This might again be linked to the stronger cation water hydrogen bond. [125] Hence, if hydrogen bonds were present, they contributed to the polarization of the water. But in average, there were less hydrogen bonds and, thus, the water dipole moment was lower. This perfectly explained the experimental and simulation observations discussed above.

Whereas water is one of the most common impurities in ILs, other gases or solutes offer great potential for applications. For instance, ILs were reported to show potential for fuel gas desulfurization [226, 227], natural gas sweetening, [99, 228] and reversible sulfur dioxide absorption. [229–233] These are important techniques to lower the sulfur dioxide emission by fossil fuel combustion. Sulfur oxides, a main source of atmospheric pollution, cause both environmental and human health damages due to the formation of acid rain or smog. Nowadays, the fuel gas desulfurization is the most common approach. There, the sulfur content of the fuel is lowered before the fuel is combusted and the sulfur dioxide emission is decreased. Meanwhile, sulfur dioxide is also important in chemical industry as *e.g.* the educt in sulfuric acid production, in the production of other chemicals or drugs or as preservative in food. As a consequence, recycling of sulfur dioxide produced in fossil fuel combustion is an interesting

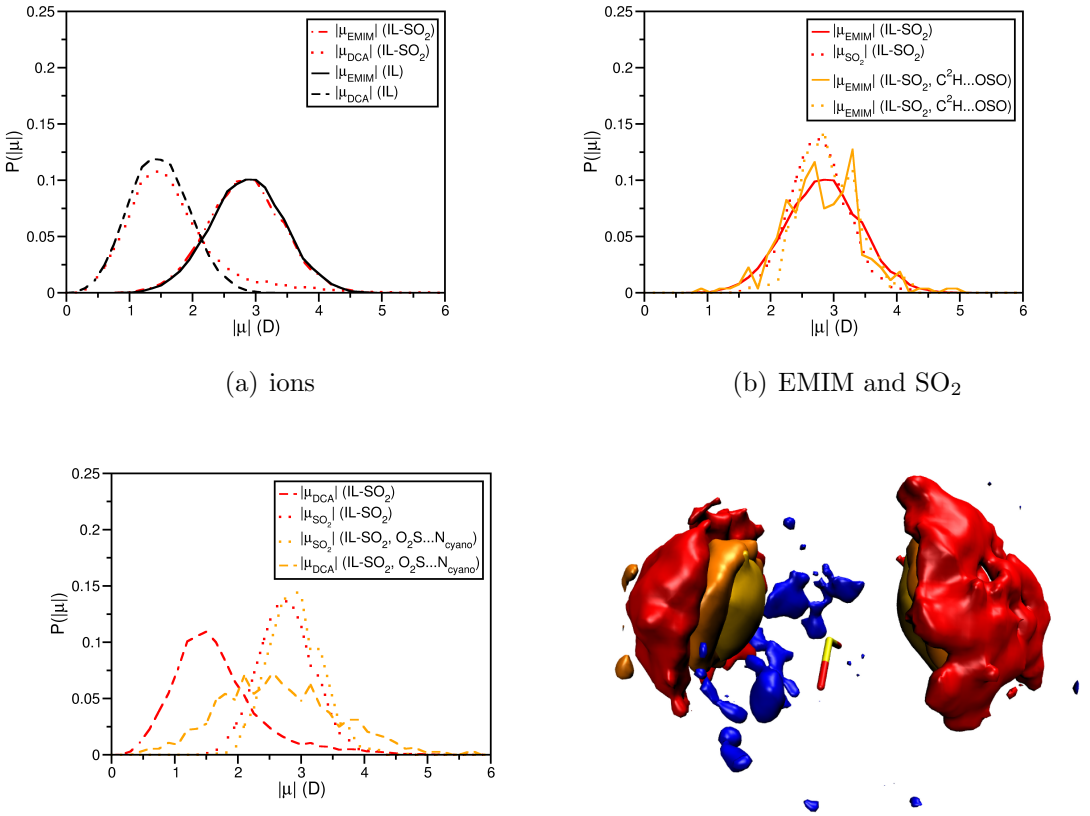

(a) ions

(b) EMIM and SO_2

(c) DCA and SO_2

(d) SDF of ions around SO_2

Figure 4.14: Dipole moment distributions (a) of EMIM DCA in neat EMIM DCA (black) and in a SO_2 EMIM DCA mixture (red), (b) of all EMIM and SO_2 (red) and only those EMIM and SO_2 forming a hydrogen bond (orange) in the SO_2 EMIM DCA mixture as well as (c) of all DCA and SO_2 (red) and only those DCA and SO_2 forming an intermolecular bond (orange) in the SO_2 EMIM DCA mixture.
The cutoff criteria for the cation SO_2 hydrogen bond were a distance $r_{C^2\cdots O}$ below 350 pm and an angle $\alpha_{H\text{-}C^2\cdots O}$ below 30 °. For the SO_2 anion contact, the following criteria were used: $r_{S\cdots N_{cyano}} < 300$ pm and $90\,° < \alpha_{O\text{-}S\cdots N_{cyano}} < 105\,°$
In (d), the spacial distribution functions of EMIM and DCA around the SO_2 molecule are plotted at an isosurface of 100 nm^{-3}. Blue denotes the C^2H hydrogen of the cation, yellow the cyano nitrogen atoms of the DCA anion, orange the anion's carbons, and red the amide nitrogen atom (for illustration see Figure 3.2).

subject. From a theoretical point of view, the comparison of water IL and SO_2 IL mixtures can be instructive as water and SO_2 have a similar structure, but the charge distribution is converse. Therefore, SO_2 cannot act as hydrogen bond donor, only as acceptor. In this way, it might be possible to distinguish pure packing effects from electronic interactions. Similar as for water, the SO_2 solubility in ILs is rather high at a mol ratio of around two SO_2 per ion pair. The solution of such large amounts of SO_2

in an IL changes the viscosity, conductivity, and density significantly [229, 233] as the long range interactions are disrupted. [234] The non-ideality which was observed in the solution behavior was said to be dominated by entropic effects. [235] Furthermore, non-task specific ILs are still discussed to either only physically absorb [229, 230, 233] or also chemically absorb [236] SO_2. On *ab-initio* level, there were several studies of ground state structures and a specific directional intermolecular bond between the anion and the sulfur atom was found. [237, 238] This opens the question if such an interaction is also present and decisive in the liquid phase at finite temperature and an AIMD study was conducted to give first insight.

Indeed, the electrostatic properties of the IL were changed as, especially, the anion dipole moment distribution was altered due to a specific interaction with the sulfur atom. As shown in Figure 4.14 (a), the dipole moment distribution of the cation was insensitive to the presence of SO_2 whereas the dipole moment of the anions was more likely to have high values. Meanwhile, only few cations were involved in a C^2H hydrogen bond to SO_2 and the dipole moment distribution of these was not significantly different from the distribution of all cations' dipole moments (see Figure 4.14 (b)). The mean dipole moment of SO_2 forming a hydrogen bond to a cation was slightly increased. A stronger effect was seen due to the specific interaction of the SO_2 to the anion (see Figure 4.14 (c)). The mean dipole moment of the SO_2 interacting with an anion was slightly increased. For an anion interacted with SO_2, the dipole moment distribution was extremely broad covering a range from about 0.5 D to 6 D and the mean dipole moment was increased by approximately 1 D compared to the one of all anions. Thus, the specific interaction with the sulfur atom of SO_2 led to the occurrence of high anion dipole moments not observed in neat EMIM DCA.

Also, the spacial distribution functions clearly demonstrate that there was a preferred SO_2 anion arrangement via an intermolecular nitrogen sulfur bond whereas the cations were loosely spread around SO_2 (see Figure 4.14 (d)). In general, the anions were proposed to play the key role in determining gas solubility for imidazolium based ILs. [238–240] For instance, the anion was found to interact more closely with water in water MMIM Cl mixtures studied by classical MD [241, 242] as it formed hydrogen bonds with water. The SO_2 anion arrangement observed here resembled the one reported for ground state structures of small anion SO_2 clusters. [237, 238] For instance, also strong sulfur oxygen [237] or sulfur fluoride interactions [238] were observed in ground state structures. This complex formation of SO_2 and the anion might hint to a chemical absorption mechanism as proposed in [236]. However, it depends on the strength of this intermolecular bond if the absorption will be identified as physical or chemical absorption.

For the characterization of this nitrogen sulfur bond, six ground state structure of one EMIM DCA ion pair with one SO_2 molecule were studied by MP2/def2-TZVPP level of theory. In these ground state structures, the anion and SO_2 adopted always a similar geometry as in the liquid phase having an angle $\alpha_{\text{O-S}\cdots\text{N}_{\text{cyano}}}$ of 95 ° to 98 ° and a distance $r_{\text{S}\cdots\text{N}_{\text{cyano}}}$ of 244 pm to 261 pm. These distances were well below the sum of the Van der Waals radii of 335 pm. For one of these ground state conformations, the NBO and the SEN analysis were carried out (see Chapters 2.3.5 and 2.3.4). Between the interacting anion nitrogen atom and the sulfur atom, a SEN of 0.13 e was found. For comparison, a typical hydrogen bond between uncharged molecules with such a SEN has an interaction energy of about −45 kJ/mol. [168] The three CH

anion hydrogen bonds found in **hb**-EMIM DCA (see Chapter 3) had SEN of about 0.026 e. Hence, the anion and SO_2 were connected by a considerable intermolecular bond. According to the NBO analysis, electron density was transferred between the anion and SO_2 and both the cyano bond as well as the SO bonds were weakened. In an natural orbital picture, the bonding orbital σ_{CN} of the cyano CN bond and the antibonding orbitals σ^*_{SO} of the two SO bonds interacted with an NBO interaction energy of about 18 kJ/mol. Additionally, a lone electron pair of the sulfur n_S interacted with one antibonding orbital σ^*_{CN} of the cyano CN bond with an NBO interaction energy of 9.4 kJ/mol. These NBO interaction energies were in the range found for the hydrogen bonds in **hb**-EMIM DCA.
In order to further elucidate the impact of this bonding on the properties of the mixture, a larger simulation should be done as well as simulations of mixtures at various concentrations. However, the presence of SO_2 had significant influence on the molecular electrostatic properties of the IL which was different from the impact of water on MMAN. Thus, the study of solute IL mixture appears promising and might help to further elucidate the decisive principles for the molecular electrostatic properties.

4.7 Conclusion

The electrostatic properties were rather similar for all ILs studied as the monopoles were reduced and monopoles as well as dipole moments fluctuated strongly. Meanwhile, the electrostatic properties were found to be local on the molecular size and few ps time scale. That led to the conclusion that the Coulomb interactions gave rise to common characteristics. Electronic polarization was shown to be decisive for the molecular electrostatic properties. For instance, hydrogen bonds could be shown to affect the mean dipole moment, but leave the width of the dipole moment distribution unaltered. Thus, this two ion interaction did not dominate the electrostatic properties of the ions which were still determined by the whole local environment.
If further components as water or sulfur dioxide were introduced, the electrostatic properties of some species changed whereas those of others remained as in the neat liquids. In the water MMAN mixture, only the dipole moment distribution of water was altered significantly whereas the dipole moment distribution of DCA in a SO_2 EMIM DCA mixture was greatly influenced by the presence of SO_2. Thus, the electrostatic properties of ions in the liquid phase were highly sensitive to the species present and their specific interactions.
After the focus on Coulomb interactions in this chapter, the influence of the other two main interactions, hydrogen bonding and dispersion, will be discussed in Chapter 5.

Chapter 5

Liquid phase: local interactions and distinct properties

The strong Coulomb interactions were found to be decisive for several common properties of ILs as for instance the large fluctuations in the molecular electronic structure and the significant screening. However, the properties of each IL are unique and the reason for this might be associated with weaker interactions as dispersion or hydrogen bonding or with the shape of the ions. For instance, the directionality of hydrogen bonding can cause a three dimensional network. Also, hydrogen bonds were discussed to decrease the viscosity. [30] Thus, the comparison of ILs with anions of various basicity might shed light onto the role of the cation anion interaction for the structure (see Chapter 5.2). Dispersion was proposed to cause microsegregation in ILs with lipophilic clusters of the alkyl sidechains of the imidazolium cations. [39, 50] BMIM based ILs have longer sidechains than EMIM ILs and should show a more pronounced microsegregation as will be discussed in Chapter 5.3. Differences in mutual orientations and interaction strengths reflect themselves in IR or Raman spectra. As these are computationally expensive to obtain from AIMD simulations, the power spectra, which summarize all fast motions of the ILs, are discussed as alternative in Chapter 5.4.

5.1 Computational details

The data in this chapter is based on the same AIMD simulations as specified in Chapter 4.1, *i.e.* 30 MMIM Cl, 32 EMIM SCN, 30 EMIM DCA, 30 BMIM Cl, 30 BMIM SCN, and 30 BMIM DCA. The MMIM Cl system was simulated at 425 K, the others at 400 K. Furthermore, the simulation data of 30 BMIM DCA at 600 K is used for comparison. The spacial distribution functions (SDF) and the power spectra were calculated with TRAVIS. [184]

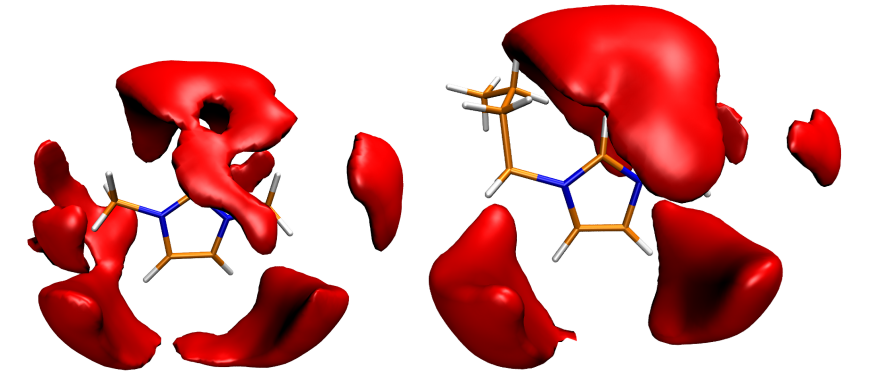

(a) MMIM Cl

(b) BMIM Cl

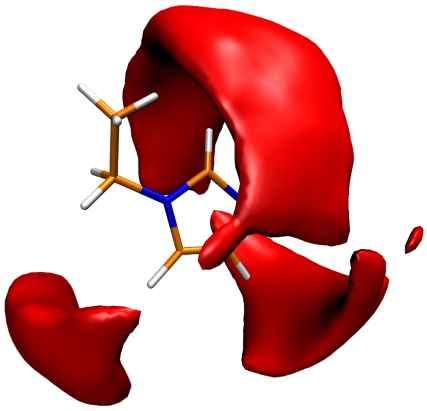

(c) EMIM SCN

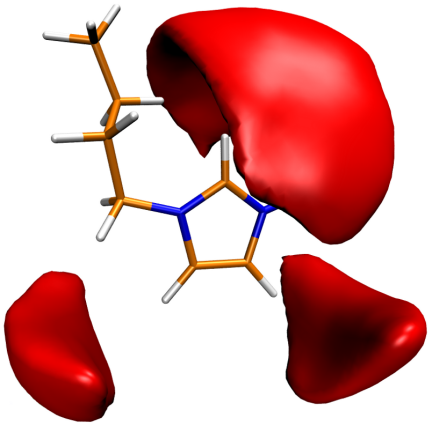

(d) BMIM SCN

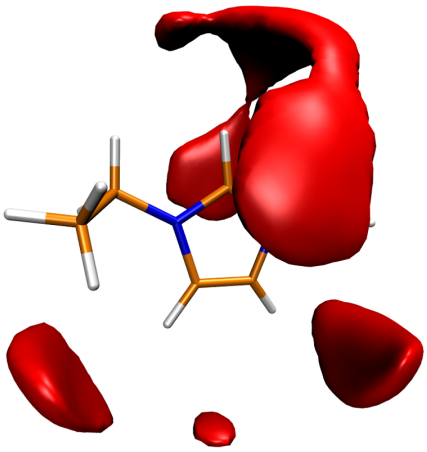

(e) EMIM DCA

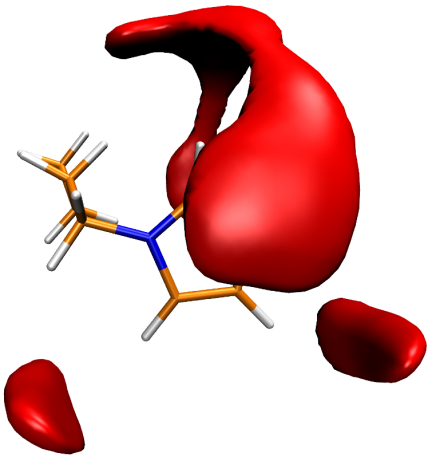

(f) BMIM DCA

Figure 5.1: Isosurface of the spacial distribution function of the anion around the cation for (a) 30 MMIM Cl, (b) 30 BMIM Cl, (c) 32 EMIM SCN, (d) 30 EMIM SCN, (e) 30 EMIM DCA, and (f) 30 BMIM DCA at an isovalue of 100 nm^{-3}, except for (a) MMIM Cl for which it is given at an isovalue of 150 nm^{-3}. The reference plane is defined by the N-C^2-N group of the imidazolium ring.

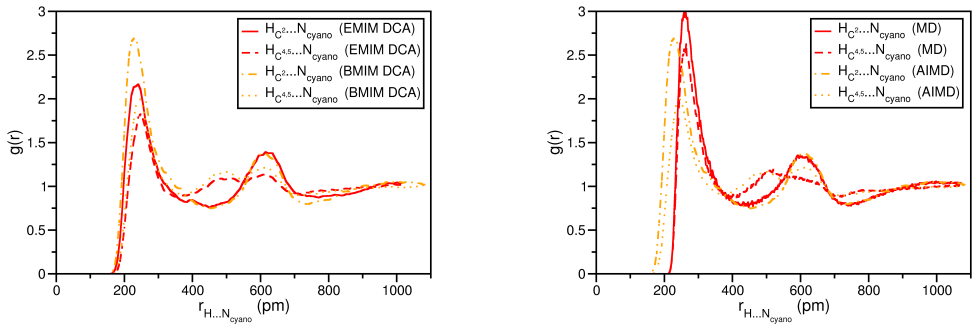

(a) EMIM DCA and BMIM DCA (b) AIMD and MD based

Figure 5.2: Radial distribution function of the anion around the cation for (a) 30 EMIM DCA and 30 BMIM DCA and for (b) 30 BMIM DCA based on AIMD and MD data. The simulation box size was about (2000 pm)^3.

5.2 Hydrogen bonds

In the liquid phase, the anion was most likely to be in a hydrogen bond position to the cation as can be deduced from the spacial distribution functions in Figure 5.1. This is in agreement with the finding that hydrogen bonding was more decisive than dispersion for the mutual orientation of an ion pair in gas phase at 400 K as discussed in Chapter 3.3. In contrast to the gas phase EMIM DCA ion pair (see Figure 3.3), an anion in the liquid phase formed hydrogen bonds to the C^4H and C^5H hydrogens as well instead of only binding to the most acidic C^2H hydrogen (compare also Figure 3.2). Such a difference between the gas and liquid phase was already observed in Monte Carlo simulations of 1,3-dimethylimidazolium bis(trifluoromethylsulfonyl)amide and 1-hexyl-3-methylimidazolium bis(trifluoromethyl-sulfonyl)amide. [193] It might be linked to the three dimensional arrangement in the liquid phase as each ion interacted with several counter ions.

Each anion showed a specific order around the cation. For MMIM Cl and BMIM Cl, the Cl anion was found in front of the methyl group with a small probability (see Figure 5.1 (a) and (b)). In such a position, the bulkier anions SCN and DCA were not registered (see Figure 5.1 (c) to (f)). In EMIM SCN, BMIM SCN, EMIM DCA, and BMIM DCA, the anion occupied the three hydrogen bond positions to the imidazolium ring cations. In general, the anions were most spread close to the C^2H position. But especially there, the spacial distribution functions showed a characteristic shape depending on the anion. Whereas the distribution functions in this area were rather similar for Cl and SCN containing ILs (see Figure 5.1 (a) to (d)), a special shape was detected for EMIM DCA and BMIM DCA (see Figure 5.1 (e) and (f)). The DCA anion was more likely to be stacked above the imidazolium ring than the other ions. This might be also due to the rather long rod-like shape of the DCA allowing for being with one cyano nitrogen close to C^2H and with the other part of the anion on top of the imidazolium ring. These on-top positions were not occupied in the gas phase (compare Figure 3.3), but the SDF in front of the C^2H atom was similar, having two maxima slightly displaced from the C^2H bond direction. Such a two maxima structure

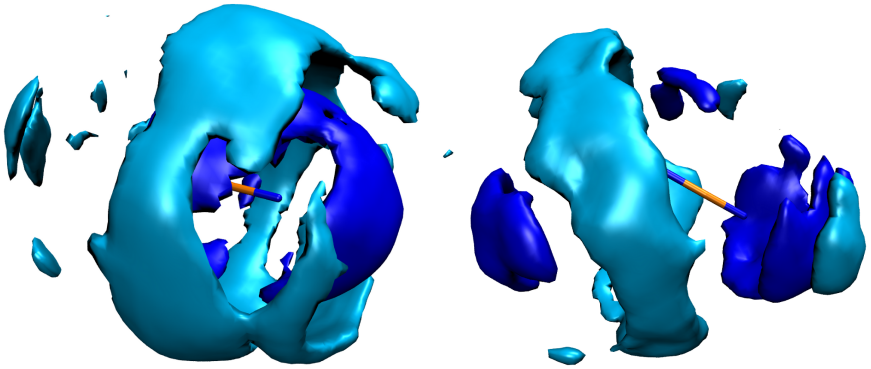

(a) EMIM SCN (b) EMIM DCA

Figure 5.3: Isosurfaces of the spacial distribution functions of the cation atoms around the anion for (a) 32 EMIM SCN and (b) 30 EMIM DCA at isovalues of 75 nm^{-3}. The C^2H hydrogen distribution is shown in dark blue, the $C^{2'}$ carbon one in light blue. The reference plane is defined by the S, C, and N atoms for SCN and by three nitrogen atoms for DCA.

was not found for Cl or SCN based ILs (see Figure 5.1 (a) to (d)). Also, for DCA containing ILs, the anion was likely to be found in a position close to both the C^4H and C^5H hydrogen (see Figure 5.1 (e)). This position had a SDF value of about 80 for BMIM DCA and, thus, the position was occupied, but is not shown in Figure 5.1 (f). Possibly, this special maxima was a consequence of the anion's shape, too.

The sidechain length of the cation had only a minor impact on the spacial distribution of anions around the cations. If the anion spacial distribution function of MMIM Cl was drawn at an isovalue of 100 nm^{-3}, the anion was likely to be at any place around the cation. Hence, MMIM Cl was less structured than all other studied ILs. MMIM Cl has the shortest sidechains and, thus, microsegregation is highly unlikely. Moreover, the cation is symmetric and, possibly, less specific positions are formed. For BMIM SCN, the stacked conformation was less likely than for EMIM SCN, the anion was slightly more located in front of the ring. Also, the spacial distribution function showed a concentration on a smaller area at the other two positions. Similar differences were observed between the SDFs of EMIM DCA and BMIM DCA. Thus, in BMIM based ILs, the anion was more focused on distinct positions. This can also be seen from the RDF of the hydrogen bonds in EMIM DCA and BMIM DCA in Figure 5.2 (a). Whereas the positions of the probability maxima were the same for EMIM DCA and BMIM DCA, the maxima were connected to a higher probability for BMIM DCA. This higher degree of structuring would be in agreement with stronger microsegregation in BMIM based ILs (see also Chapter 5.3).

While the anions had preferred orientations with respect to the cations, the distribution of the cations around the anions displayed some rotational symmetry for SCN and DCA (see Figure 5.3). Especially for DCA, the acidic side C^2H of the cation was close to the basic cyano nitrogens. The $C^{2'}$ carbon of the ethyl change was most likely to be adjacent to the amide nitrogen. This spacial ordering was a sign of hydrogen bonding conformations. For the EMIM ILs, this structuring is more distinct for the end carbon of the sidechain than for BMIM ILs while it was similar for the C^2H hy-

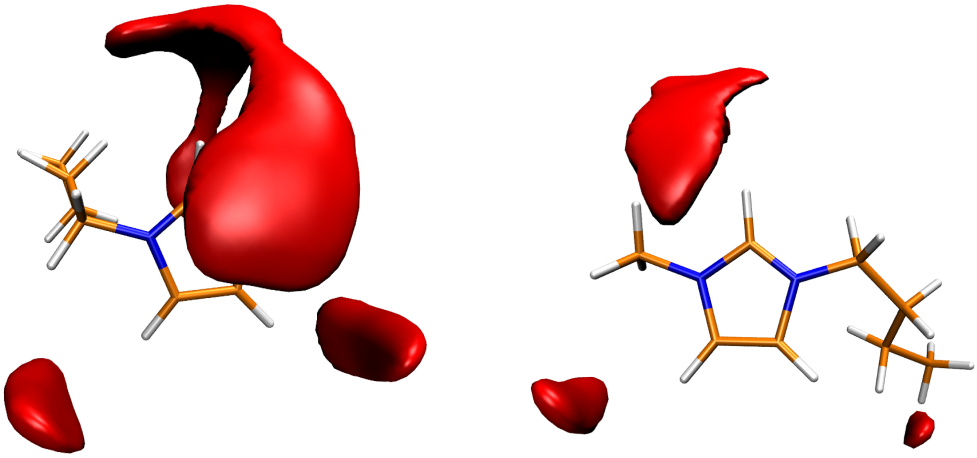

(a) 400 K (b) 600 K

Figure 5.4: Isosurface of the spacial distribution function of the anion around the cation for 30 BMIM DCA at (a) 400 K and (b) 600 K at an isovalue of 100 nm^{-3}. The reference plane is defined by the N-C^2-N group of the imidazolium ring.

drogen (compare Figures 5.3 and A.2). That might be a sign of an increased distance between the sidechain and the anion and, hence, of microsegregation. However, a three dimensional ordering beyond the first cation anion contact was not found. This was already demonstrated by the angular correlations in Chapter 4.4 (see Figure 4.9). Thus, while hydrogen bonds caused a certain short range order, a farther reaching network did not build up.
Also in these bulk phase systems, an effect of temperature was observed. 30 BMIM DCA ion pairs were simulated at 600 K and the same density as for the 400 K system. Actually, it was found that the ions were less ordered as the SDF of the anions around the cations had lower maxima and the isosurface at a value of 100 nm^{-3} was smaller (see Figure 5.4). Furthermore, the shape of the isosurface changed. The stacked conformation, which DCA tended to adapt at 400 K, was less likely for 600 K whereas the three hydrogen bond positions were occupied still similarly. Hence, with increasing temperature, the influence of dispersion decreased as observed for ion pairs (see Chapter 3.3). In general, the structures obtained seemed to characterize indeed AIMD equilibrium state structures as they deviated significantly from the MD structures which the initial configuration of the AIMD simulation obeyed (see Figure 5.2 (b)). Regarding the rather short simulations times of mostly about 15 ps, this was not obvious. But, in the AIMD simulations, the first maxima were at distances about 30 pm smaller than in the MD simulations and had a slightly lower probability as observed already. [38] Also, the RDF of the C^4H and C^5H hydrogens was more structured in the range from 400 pm to 700 pm for the AIMD data. Thus, there were marked systematic differences in the RDFs which were similar for all studied ILs. In order to improve force fields, the RDFs could be fitted to obtain the AIMD based RDFs which include electronic structure effects. [84, 243]

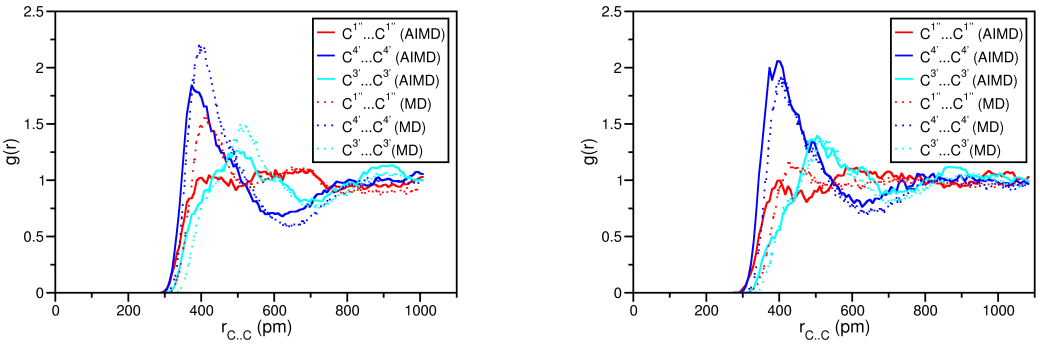

(a) BMIM Cl (b) BMIM DCA

Figure 5.5: Radial distribution functions of the sidechain carbon atoms for (a) 30 BMIM Cl and (b) 30 BMIM DCA based on AIMD and MD data (for nomenclature see Figure 1.3). The simulation box size was about $(2000\ \mathrm{pm})^3$.

5.3 Dispersion

Imidazolium cations with long alkyl sidechains consist of a hydrophilic charged part, the imidazolium ring, and a lipophilic uncharged part, the sidechain. Whereas the imidazolium ring will tend to interact strongly *via* Coulomb forces or hydrogen bonding, the bonding of the sidechain is expected to be dominated by dispersion. In fact, it was found that the anions were close to the imidazolium ring (see *e.g.* Chapters 3 and 5.2). In order to maximize the total attractive interactions, domains should be formed and the sidechain should be close to other sidechains while the imidazolium ring and the anion build a polar environment. Indeed, such an ordering behavior was found in experiments [9,11,13,50,244–248] and simulations. [17,23,39] BMIM ILs did show such behavior, EMIM ILs not. However, until now, the phenomenon was only studied with classical simulation techniques, but not in an AIMD simulation. As in AIMD, the electronic effects are described directly, a different picture might emerge.

In the AIMD based simulation, a sidechain clustering was found, too. The very small simulation volumes of about $(2\ \mathrm{nm})^3$ were sufficient to allow for such ordering. Even for the short simulation time, there was a difference between the RDFs based on MD and AIMD simulations (see Figure 5.5). For BMIM DCA, the $C^{4'}$ carbons of butyl sidechains of different cations tended to be closer together than in the MD simulation while a less distinct order was found for BMIM Cl as the first maximum of the RDF was lower. Probably, the MD RDFs depended significantly on the force field and the strength of the interionic interactions and, thus, no systematic trend between AIMD and MD RDFs was found. However, DFT has also general deficiencies in describing dispersion (see Chapters 1.3 and 2.2) and the data of the BMIM ILs was based on AIMD simulations with an empirical dispersion correction whose performance was only tested for gas phase ion clusters. Hence, the description of the dispersive sidechain contact might be connected to an unknown bias.

The distribution of the outermost carbon of a cation's sidechain around the sidechain

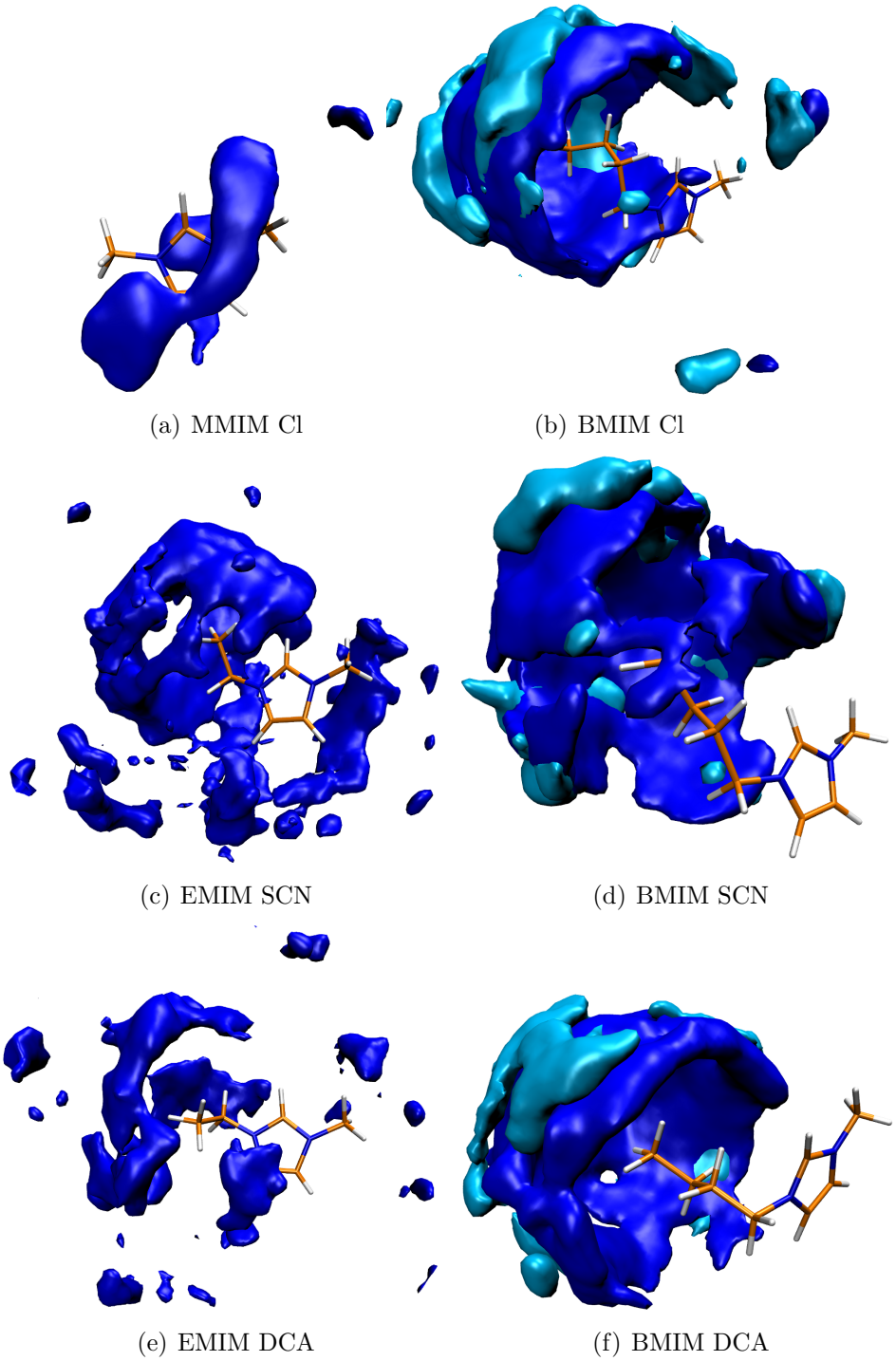

(a) MMIM Cl (b) BMIM Cl

(c) EMIM SCN (d) BMIM SCN

(e) EMIM DCA (f) BMIM DCA

Figure 5.6: Isosurface of the spacial distribution function of the sidechain carbon atoms for (a) 30 MMIM Cl, (b) 30 BMIM Cl, (c) 32 EMIM SCN, (d) 30 EMIM SCN, (e) 30 EMIM DCA, and (f) 30 BMIM DCA. Dark blue denotes the sidechain end carbon atom (at an isovalue of 45 nm^{-3}, except for MMIM Cl with an isovalue of 100 nm^{-3}) and light blue the $C^{3'}$ carbon atom (at an isovalue of 45 nm^{-3}) for BMIM based ILs (for nomenclature see Figure 1.3).

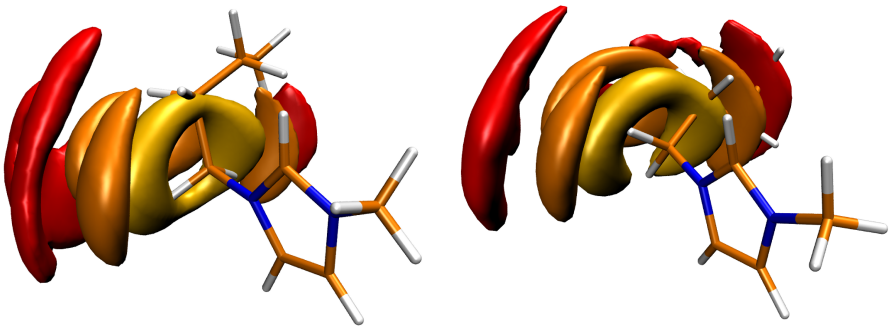

(a) BMIM Cl (b) BMIM DCA

Figure 5.7: Isosurface of the intramolecular spacial distribution functions of the sidechain carbon atoms for (a) 30 BMIM Cl and (b) 30 BMIM DCA. Yellow denotes the $C^{2'}$ carbon atom (at an isovalue of 400 nm^{-3}), orange the $C^{3'}$ carbon atom (at an isovalue of 200 nm^{-3}), and red the $C^{4'}$ carbon atom (at an isovalue of 100 nm^{-3}). The reference plane is defined by the N-C^2-N group of the imidazolium ring (for nomenclature see Figure 1.3).

of another cation differed strongly between imidazolium ILs with short and long sidechains as shown in Figure 5.6. For the BMIM ILs, the $C^{4'}$ carbon was significantly more likely to be around the sidechain than around the ring (see Figure 5.6 (b), (d), and (f) as well as for nomenclature see Figure 1.3). For the EMIM ILs (see Figure 5.6 (c) and (e)), the $C^{2'}$ carbon has a certain probability to be close to the sidechain, but also to be close to the ring. For MMIM Cl (see Figure 5.6 (a)), the methyl group was most likely close to the ring, possibly involved in an H-π interaction. If the isosurface was plotted at the same value for MMIM Cl than for the other ILs, the methyl group would be distributed homogeneously in space. Hence, an increasing degree of ordering appeared by increasing the sidechain length. Accordingly, the influence of dispersion and the connected clustering became significant for BMIM based ILs as found in experiments. [50]

Subtle differences in the segregation appeared depending on the IL's anion (see Figure 5.6). For instance, the segregation in BMIM Cl was less distinct than in BMIM DCA, differently from the trend found in MD (see Figure 5.2). Also, the rotation of the butyl sidechain was different in BMIM Cl and BMIM DCA (compare Figure 5.7). In general, the sidechain tended to point either in front or to the back of the imidazolium ring. Whereas in BMIM Cl, the $C^{2'}$ carbon of the sidechain was at any angle with an SDF isovalue of at least 400 nm^{-3} (see Figure 5.7 (a)), the $C^{2'}$ carbon was not so likely to be in plane with the imidazolium ring for BMIM DCA (see Figure 5.7 (b)). Thus, the rotation of the butyl sidechain around the $C^{1'}$ carbon seemed hindered for BMIM DCA. BMIM SCN and BMIM DCA ILs showed a similar sidechain rotation and segregation (compare Figure 5.7 (b) and A.3). In the two known crystalline phases, the butyl sidechain of BMIM Cl tended to point either in front or to the back of the imidazolium ring [118, 249] as also found to be the most likely conformations in the liquid phase here (see Figure 5.7 (a)). Regarding the SDF of the $C^{3'}$ carbon in BMIM Cl, a gauche-anti conformation of the butyl chain seemed more likely than the anti-anti conformation, but both conformations were adapted

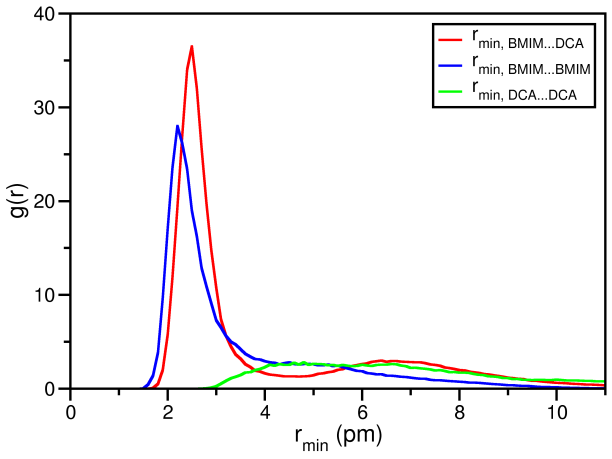

Figure 5.8: Radial distribution functions of the minimal interionic atom-atom distance between cations and cations (blue), cations and anions (red), and anions and anions (green) for 30 BMIM DCA. The simulation box size was $(2174\ \text{pm})^3$.

by the butyl sidechain. In an MP2 study of the ground state of an BMIM Cl ion pair, [97] the gauche-anti conformation was found be more stable. However, it was not yet established if the crystal structure containing BMIM Cl in gauche-anti conformation or the crystal structure with the anti-anti conformation of the sidechain was more stable. [118]

Hence, dispersion was decisive for the interactions of the sidechains and the order of the liquid phase even though the interionic RDFs based on reference centers as the center of mass (COM) did propose that the ions were ordered by charge (compare *e.g.* Figure 4.1 and *e.g.* Refs. [8, 53, 62, 107, 219, 250]). However, such reference center based RDFs might be misleading due to the bulky shape of the ions. If instead, as in Figure 5.8, the minimal interionic atom-atom distances were considered, the intermolecular distance between all atoms of both ions were taken into account. Then, the maxima of the cation cation and cation anion RDFs were at 220 pm and 250 pm, respectively, and the minimal cation cation distance was even smaller than the cation anion one. Thus, one may conclude that cations were surrounded both by cations and anions in equal extent. Anions were surrounded solely by cations because the minimal anion anion distance was about 260 pm. Consequently, the RDFs based on the minimal atom atom distances gave a different picture compared to the reference center based ones. The reason was that the cation was significantly bulkier than the anion. Both ions were not spherical, the BMIM cation was highly asymmetric. The sidechain interacted closely with other cations' sidechains while the imidazolium ring was surrounded by anions. The COM was relatively close to the imidazolium ring. Thus, the orientation of the ions had a large impact on the distance between the COM. To account for the orientation dependence, Voronoi decomposition was proposed to identify the first neighbors. [251, 252] This formalism allowed for a detailed insight into the local dynamics of the first shell. Regarding this, the interpretation

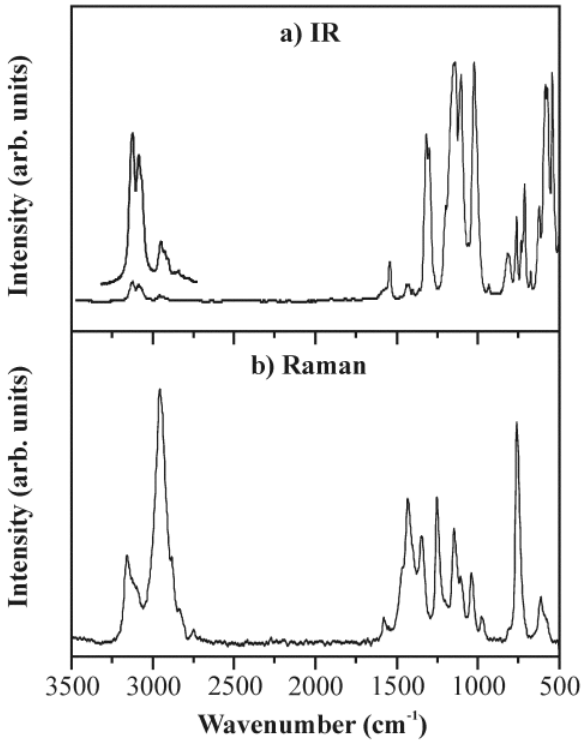

Figure 5.9: (a) IR spectrum and (b) Raman spectrum of 1-ethyl-3-methylimidazolium ethylsulfate taken from Ref. [253].

of RDF based on general reference centers has to be done carefully and it may be advantageous to focus on SDF or on specific atom atom interionic distances.

5.4 Short time dynamics: power spectra

IR spectra or Raman spectra offer insight in the short time dynamics of ILs. [35, 45, 173, 190, 194, 249, 253–256] For illustration, the IR and Raman spectra of 1-ethyl-3-methylimidazolium ethylsulfate [253] are given in Figure 5.9. For the interpretation, the experimental signals were often compared to results of *ab-initio* based vibration frequencies of single ions or ion clusters in their ground state [35, 45, 97, 173, 186, 190, 194, 249, 253, 256, 257] and also to some classical simulations. [34, 234] In general, only few IR spectra have been calculated based on AIMD simulations due to the prohibitive computational costs. [258–261] Though it was shown that relatively short simulation times were sufficient to obtain an IR spectra reproducing the experimental one, [260, 261] the total dipole moment has to be calculated rather frequently to evaluate the selection rules. In an IR active vibration excitation, the mode must involve a change in the dipole moment. In contrast, a Raman active transition is connected to a non-zero polarizability derivative with respect to the normal coordinate. This polarization changes are also expensive to evaluate in an AIMD simulation. Thus, whereas IR and Raman spectra cover the same frequency range, the selection rules

are different and the observed signals vary (see Figure 5.9). As a rule of thumb, symmetric vibrations can be detected by Raman spectroscopy, but not by IR spectroscopy. The intensities of the signals are connected to the transition rates which are given by Fermi's golden rule.
The power spectra (or power spectral density) is the Fourier transform of the velocity autocorrelation function [172] if applying the Wiener-Khinchin theorem [262,263] and assuming a wide-sense stationary random process. Here, power means the squared value of the signal. In order to obtain the power spectra, the velocity autocorrelation function is determined for each atom in the three directions x, y, and z. Due to the short simulation times, all timesteps are considered as reference times for the autocorrelation. Subsequently, the sum of all these autocorrelation functions is determined and the Fourier transform of this is calculated. In order to increase the quality of the spectra, a Hanning window function [264] is applied as filter in the time domain, the time domain signal is evenly symmetrized about the origin in the Fourier transformation, and zero padding is done. [264] If the power spectra is calculated, the selection rules for IR and Raman active signals are disregarded and also the signal intensities do not have to be similar to the ones in the corresponding IR and Raman spectra. However, the wavenumbers of the signals are the same. While all present vibrational-rotational movements of the systems are captured by the power spectra, only some of them are IR or Raman active. Hence, whereas power spectra cannot predict IR or Raman spectra, the origin of the obtained signals is the same. In this way, power spectra can help to interpret the signals found in experimental IR or Raman spectra. In this way, power spectra based on AIMD simulation offer a unique tool in the study of the fast dynamics in ILs. They can describe the vibrations in liquid phase which are an result of the cooperativity of many molecules' interactions. Such coupled modes of larger clusters or polarization effects can hardly be captured by the vibrational frequencies of single ions or small ion pairs in their ground state structure. Furthermore, the calculation of a power spectra does not affect the computational cost of the AIMD simulation. It can be easily done with a program as TRAVIS [184] as described above. A power spectra of deuteriated MMIM Cl was already calculated based on an AIMD simulation and the influence of hydrogen bonding on the C^2D deuterium was shown. [34] In general, the quality of the power spectra would increase on larger system sizes and longer simulation times accessible only with classical MD. But, in most classical simulations, the CH bond lengths are constrained in order to allow for a larger time step. As a consequence, power spectra obtained on such MD simulations should not give meaningful results at least for high wavenumbers at which the hydrogen vibrations occur.

Due to approximations used in the CPMD method, the obtained wavenumbers needed to be corrected. Both the fictitious mass and the BLYP functional contribute to the slowing down of the dynamics. An hypothetical fictitious electron mass of 450 a.u. was proposed to include both effects. [260] Thus, the wavenumbers have to be corrected by $\omega_{\text{corrected}} = \omega\sqrt{1 + \frac{\delta M}{M}}$. [259] Obviously, the masses M and δM depend on the atoms actually involved in a certain vibration. As a consequence, the wavefunction correction should be specific for each vibration. However, the assignment of the involved molecule parts is not *a-priori* possible and the corrections will have rather similar values. Accordingly, it is well-established to choose a gen-

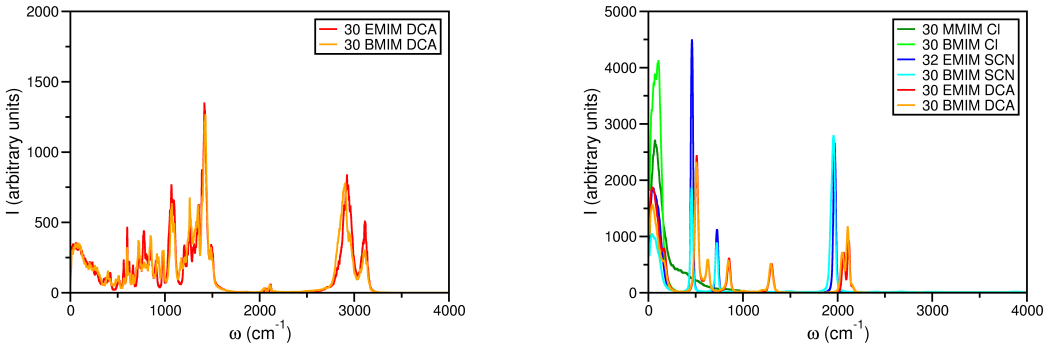

(a) EMIM DCA and BMIM DCA (b) Anion component spectra

Figure 5.10: Power spectra of (a) EMIM DCA and BMIM DCA and (b) part power spectra of the anions in all studied ILs.

eral correction factor. [260, 261, 265] For an imidazolium cation, the mass including the fictitious mass correction is about 1.100 times the value of the real mass, so the wavenumber correction factor is 1.049. Analogously, the wavenumber correction for DCA is a factor of 1.042, for SCN 1.030, and for Cl 1.024. As a universal correction factor was needed within this work, it was chosen arbitrarily to be 1.045 which gave results rather consistent with experimental data (see below). [190, 253, 255, 256] For water spectra in literature, higher correction factors of 1.115 [260], 1.117 [261] or 1.414 [265] were proposed after fitting to the experimental data.

In general, the wavenumbers of the signals in the power spectra (as shown for instance in Figure 5.10) were in good agreement to experimental IR and Raman spectra [35,173,190,249,253–256,266] in contrast to the signal intensities. For instance, the ring CH bond stretch vibrations were reported to be at around 3050 cm^{-1} to 3200 cm^{-1} in BMIM Cl [249, 254, 266] which was consistent with the range from 3040 cm^{-1} to 3150 cm^{-1} found here (see Figures 5.11 (a) and A.5 (a)). The same range was observed for different imidazolium based ILs in experiments. [190, 249, 253, 255, 256, 266] All signals in the power spectra could be matched to experimentally observed signals. However, there were some signals which were found in any experimental IR spectra, but not in the power spectra calculated here. These were bands at about 1580 cm^{-1}, 1390 cm^{-1}, 1170 cm^{-1}, and 1030 cm^{-1}. The vibrations with wavenumbers of about 1580 cm^{-1} and 1170 cm^{-1} were interpreted as imidazolium ring bending modes. [190, 253] The reason why these bands were missing in the power spectra is not yet understood. Maybe, the dipole moment of these modes changes drastically whereas the atoms move little. In general, the power spectra bands were rather broad and the resolution below the one of experimental IR spectra. The short simulation times and the small system sizes did not allow for higher resolution.

The anion vibrations (see Figure 5.10 (b)) were at wavenumbers similar to experimental IR spectra. For the monoatomic chloride, no other vibration was detected except the signal in the region around 100 cm^{-1}. For SCN, the three bands at 460 cm^{-1}, 730 cm^{-1}, and 1960 cm^{-1} were slightly below the experimentally observed signals of solid sodium thiocyanate at wavenumbers of 497 cm^{-1}, 755 cm^{-1}, and 2075 cm^{-1}. [267]

Similarly, the signals of DCA were found at slightly too low wavenumbers compared to solid sodium dicyanamide, [268] for instance 2110 cm^{-1} instead of 2230 cm^{-1} or 625 cm^{-1} instead of 664 cm^{-1}. Apart from this shift, all signals expected for the DCA anion were present in the power spectra. At very low wavenumbers, the bending mode of the DCA anion was detected at about 160 cm^{-1} to 170 cm^{-1} as in experiments. [35] The systematic underestimation of the vibration wavenumbers could be balanced by a larger correction factor. Yet, there might be some physical reason for the shift as the ions in an IL are in a different environment than in a salt crystal. In general, in all anion part power spectra as given in Figure 5.10 (b), there was a broad band around 100 cm^{-1}. Hence, all anions took part in some intermolecular vibrations [35] which are discussed below. Obviously, such a band will not appear in IR spectra of simple solid sodium salts. Qualitatively, the anion part power spectra agreed with the expectations.
At a first glance, the spectra of imidazolium based ILs with longer and shorter sidechains were rather similar (see Figure 5.10 (a)) and different anions did not change the spectra drastically (see Figures 5.11 (a), 5.12 (a), and A.4). Still, especially the wavenumbers of the aromatic ring CH bond stretching vibrations displayed a certain shift as well as the wavenumber of the intensity maximum at values below 100 cm^{-1}. Furthermore, there were signals only observed for EMIM ILs or BMIM ILs. These differences are discussed below in order to demonstrate the possibilities of power spectra in interpreting spectral data.

The aromatic CH bond stretching vibrations showed a significant red shift for the ILs with stronger hydrogen bonds (see Figure 5.11 (a) and (c)). This red shift is well known as a characteristic of hydrogen bonding. [187] Qualitatively, the CH bond is weakened by the hydrogen bond as electron density from the hydrogen bond acceptor atom is transferred into the antibonding CH σ^* orbital. As a consequence, the bond length of the CH bond increases while the force constant and, thus, the wavenumber of the stretching vibration decrease. This red shift was obtained for the aromatic CH bond vibration in the range of 3060 cm^{-1} to 3150 cm^{-1}, but not for the aliphatic CH bond vibrations around 2800 cm^{-1} to 3000 cm^{-1} (see Figure 5.11 (a)). The assignment into aliphatic and aromatic CH bond vibration became obvious if only the part power spectra of the single CH bonds were compared (see Figure 5.11 (b)) and met the expectations. [269] This is a further confirmation that the anions interacted mainly with the aromatic imidazolium ring hydrogens as discussed in Chapter 5.2. In general, the signal of Cl based ILs was the one most red-shifted to lower wavenumbers pointing to the strongest hydrogen bonds (see Figure 5.11 (c)). The signals of SCN based ILs were still slightly stronger red-shifted than the ones of DCA based ILs. Thus, the shifts reflected the same order in hydrogen bond strength as reported in literature. [40] Furthermore, the part power spectrum of the C^2H vibration depended only weakly on the sidechain length (see Figure 5.11 (c)). The difference between the C^2H bond power spectra of MMIM Cl and BMIM Cl might be due to the different DFT functionals used. In general, the similarity in the spectra of EMIM and BMIM ILs supported the finding (see Chapter 5.2) that anions were distributed similarly around the cation and, thus, close to the imidazolium ring in all imidazolium based ILs. As discussed for experimental IR spectra, [173, 194] the C^2H vibration occurred at slightly lower wavenumbers than the C^4H or C^5H vibrations (see Figure 5.11 (d)). This effect was also observed in the first and so far only other AIMD based power spectrum on an IL

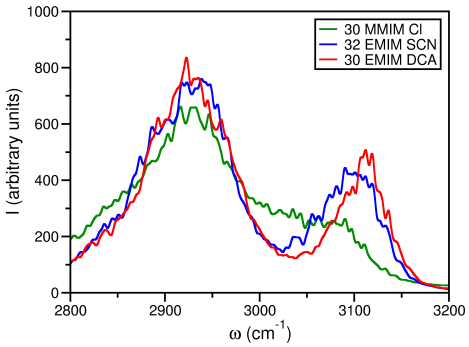

(a) EMIM ILs

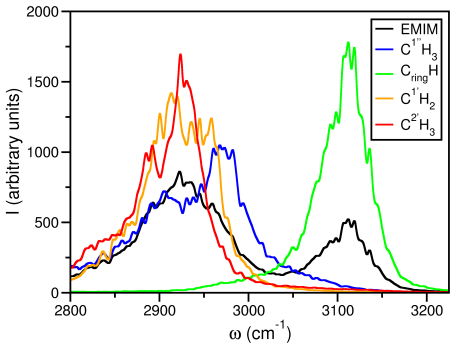

(b) components of EMIM DCA

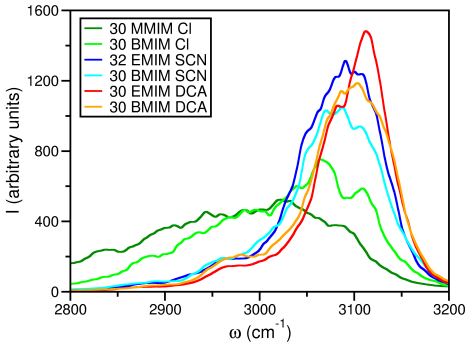

(c) C^{2}H vibrations

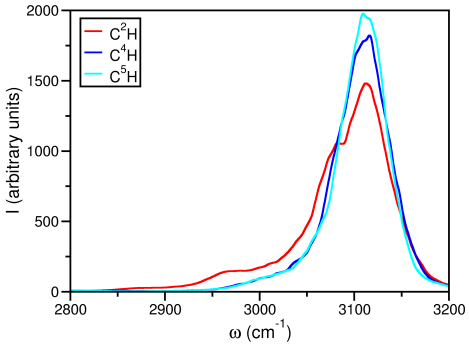

(d) C^{ring}H vibrations of EMIM DCA

Figure 5.11: Power spectra at high wavenumbers between 2800 cm^{-1} to 3200 cm^{-1}. In (a), the power spectra of MMIM Cl, EMIM SCN, and EMIM DCA are shown, in (b) the part power spectra of the different groups in EMIM DCA, in (c) the part power spectra of the C^{2}H bond for all studied ILs, and in (d) the part power spectra of the three ring CH bonds, C^{2}H, C^{4}H, and C^{5}H, for EMIM DCA (for nomenclature see Figure 1.3).

which still suffered from very few statistics. [34] Hence, crucial experimental trends could be reproduced.
In the range of 300 cm^{-1} to 1500 cm^{-1}, there were several signals which were detected either for EMIM ILs or for BMIM ILs as was expected due to the different sidechains (see Figure 5.10). The example with the highest intensity was found at about 775 cm^{-1} only for EMIM ILs (see Figure 5.12 (a)). Indeed, only the ethyl sidechain groups contributed to this as can be seen from the part power spectra of the different groups of the EMIM (see Figure 5.12 (b)). At around 730 cm^{-1}, both EMIM and BMIM ILs gave a signal (see Figure 5.12 (a)) also found in experiments. [249, 253, 256] For EMIM DCA, this signal was purely connected to some imidazolium ring vibrations (see Figure 5.12 (b)). For BMIM DCA, there were also contributions of the butyl chain at this wavenumber range (see Figure A.6). Hence, the similarity of the signals in the power spectra did not necessarily imply that they had the same origin. Indeed, for BMIM based ILs, the signal at around 730 cm^{-1} and a signal at 625 cm^{-1} were pro-

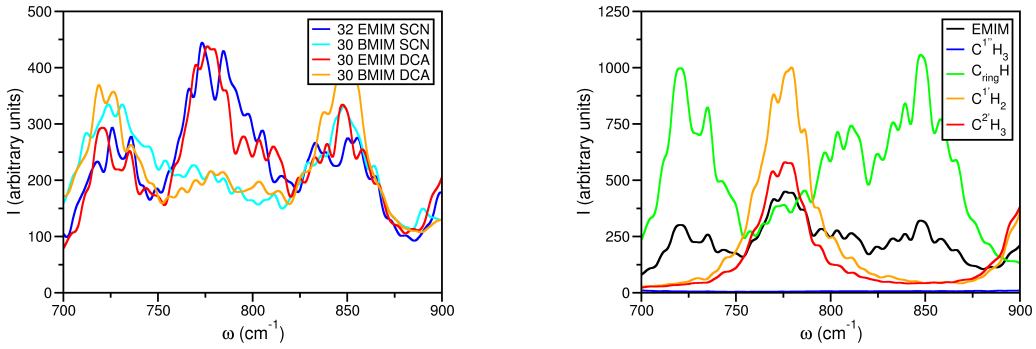

(a) EMIM ILs vs. BMIM ILs

(b) components of EMIM DCA

Figure 5.12: Power spectra in the range from 700 cm^{-1} to 900 cm^{-1} of (a) EMIM SCN, BMIM SCN, EMIM DCA, and BMIM DCA and (b) part power spectra of different groups in EMIM DCA (for nomenclature see Figure 1.3).

posed to be associated with the anti-anti conformation of the butyl sidechain. [186,249] The other, the gauche-anti, conformation of the butyl sidechain often found in ground state structures [97, 186] was reported to be associated with signals at 600 cm^{-1} and 700 cm^{-1}. [186, 249] Whereas all BMIM ILs power spectra had bands at 730 cm^{-1} and 600 cm^{-1}, there were no distinct signals observed at 625 cm^{-1} or 700 cm^{-1} (see Figure A.5 (b)). Thus, no clear conclusion could be drawn on the relative probabilities of the butyl chain conformations.

At low wavenumbers, intermolecular vibrations, having small force constants, can be detected and the wavenumber of the intensity maximum in the range of 50 cm^{-1} to 200 cm^{-1} was proposed to correlate with the hydrogen bond strength. [35, 41, 42, 45] Experimentally, the intensity maximum was at 117.6 cm^{-1} for EMIM SCN and 113.5 cm^{-1} for EMIM DCA. [35] As shown in Figure 5.13, intensity was rather constant at broad maxima and, thus, the assignment of a wavenumber ambiguous. But, the order could be characterized as follows: for MMIM Cl around 100 cm^{-1}, for EMIM SCN about 80 cm^{-1} and for EMIM DCA 60 cm^{-1}. Hence, for the ILs with short sidechains, the experimental trend was reproduced. It was proposed to show a correlation to the hydrogen bond strengths. [35, 41] In general, a higher wavenumber could imply a stronger intermolecular interaction. As all parts of the ions vibrate at these frequencies, the AIMD based powerspectra did not allow for a more detailed assignment of the shift. However, the maxima occurred at different wavenumbers than in experiment. This might be due to the uncertainty of the wavenumbers and the assignment of the maximum or to the different selection rules. In IR, Tetrahertz or Raman spectra, only certain vibrations are detected. That might lead to a different shape of the signal as the single vibrations have changed intensities and, thus, the superposition is altered, too. Hence, the maximum of this broad absorption might be shifted. Although, a vibration with a wavenumber of 65 cm^{-1} has a periodic time of 0.5 ps. As the simulation times were mostly in the range of 10 ps to 20 ps, the statistics at low wavenumbers was poor and the uncertainty of the power spectra

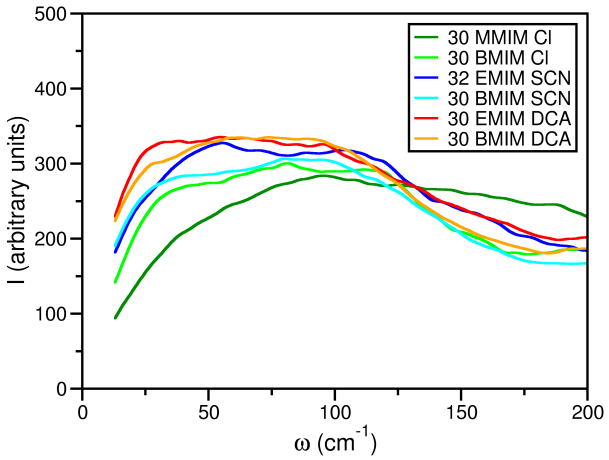

Figure 5.13: Smoothed power spectra in the range from 0 cm^{-1} to 200 cm^{-1} of all studied ILs. The shown data points are averaged over 50 original data points.

intensities should be high. For BMIM ILs, the differences between the intensity maxima were lower: BMIM Cl 90 cm^{-1}, BMIM SCN 80 cm^{-1}, and BMIM DCA 70 cm^{-1}. As the maxima were very broad, there was no significant shift. Unfortunately, no experimental data for the BMIM ILs in this wavenumber regime has been published so far. Thus, it is not possible to judge if these differences between ILs with short and long sidechains are consistent with experiments. In general, all groups of the ions including the complete cation sidechains contributed to the low wavenumbers signal in the power spectra. Hence, the influence of hydrogen bonding might be overlaid.

In summary, power spectra based on AIMD simulations of the liquid phase reproduced decisive features found also in experiments, but the simulations were computationally rather demanding. Possibly, similar information could be gained from gas phase ion pair simulations or even the ground state structure of an ion. Often in literature, the experimental spectra are interpreted with the help of IR spectra based on the ground state structure. [35, 45, 97, 173, 186, 190, 194, 249, 253, 256, 257] In any case, IR spectra based on the ground state structure of a single ion pair cannot capture cooperative effects or the vibrations of larger clusters. Although, the frequencies are mostly calculated under the assumption of harmonic vibrations which is only a rough approximation. In AIMD dynamics, the anharmonicity of the bond vibration is described in principle. As discussed in Chapter 3.3, the ion pair conformation at 400 K was significantly different from the ground state structure. These differences should be reflected in the power spectra of the three states as it is discussed next.

Indeed, the spectra found for the three states were different. Thus, wavenumbers obtained for the ground state structure of one ion pair at 0 K differed most from the two power spectra. In particular, around 3000 cm^{-1}, the wavenumbers were too high, even though the wavenumbers were not corrected by the factor 1.045 That might be due to the neglect of anharmonicity. [258] The power spectra of one ion pair in the gas phase at 400 K and 30 ion pairs in the liquid phase at 400 K were rather identical

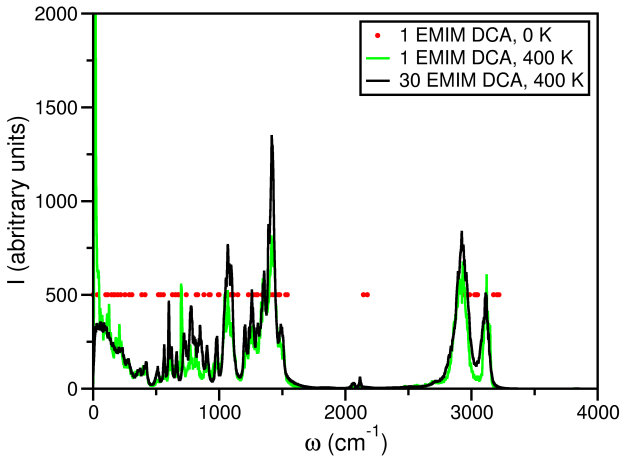

Figure 5.14: Power spectra of a single EMIM DCA ion pair in gas phase at 400 K and of 30 EMIM DCA ion pairs in liquid phase at 400 K as well as the (uncorrected) wavenumbers obtained for a single EMIM DCA ion pair at 0 K.

at high wavenumbers. But in the range of 500 cm^{-1} to 1000 cm^{-1}, the signal structure was qualitatively different. At these wavenumbers, vibrations less localized than at high wavenumbers were observed and seemed to be more dependent on the ion's environment. Also, the intensity maximum at around 60 cm^{-1} could not be found in the one ion pair's power spectra as the free rotation of the whole ion pair was possible in the gas phase. Actually, this rotation gave the most intense signal in the power spectra of the gas phase ion pair. For the bulk phase, the power spectra intensity approached 0 at 0 cm^{-1}. In this aspect, the power spectra of AIMD simulations of the liquid phase gave information not accessible by ground state structure based calculations and in agreement with experimental spectra. Similar to the findings for the electrostatic properties, the power spectra of eight ion pair simulations were nearly identical to the power spectra of the 30 or more ion pair simulations. This strengthened the notion of locality also for the short time dynamics. At such short time scales, the diffusion was still so low that the ions moved only roughly one molecular length. The proposed ion cages [8, 13, 15, 33, 37, 53, 55, 74, 107, 219] would still be stable. That might explain why the power spectra were not system size dependent.

5.5 Conclusion

Indeed, hydrogen bonds and dispersion were found to influence the structure and dynamics of ILs. The effect of different anions led to differences in the spacial ordering. For BMIM ILs, the formation of sidechain clusters was detected and, thus, the influence of dispersion was demonstrated. In general, the power spectra based on AIMD simulations of the liquid phase were in good agreement with experimental IR or Raman spectra. Hence, the power spectra could provide a new standard term of com-

parison with experiments without necessarily spending the additional computational effort to obtain IR spectra. They might provide a first insight in electronic effects as, for instance, the hydrogen bond strength was correlated to observed wavenumbers shifts in the power spectra.

Chapter 6

Conclusions and Perspectives

6.1 Balance of interactions

The various systems and states studied allowed for some general conclusions: In the liquid phase as well as in the gas phase or in the ground state, the Coulomb interactions were always dominant and hydrogen bonding was present. Only, in the ground state structures, the mutual orientation of anion and cation was more influenced by dispersion than by hydrogen bonding. In the bulk phase, Coulomb interactions led to a short-range charge order and preferred orientations such that the ions' centers of charge were as close as possible to each other. Also, the molecular electrostatic properties showed general characteristics which will be discussed in the following.
First, the ionic net charges were found to be reduced (see Chapters 3 and 4 and also Refs. [38, 44, 74, 83, 84, 96, 102, 107]) due to two main reasons: charge transfer and polarization. The quantum based methods for assigning partial charges include the two aspects in a different extent. The Blöchl protocol used for the bulk phases captures polarization effects and charge transfer whereas other methods which assign the electron density to atoms as the NPA approach characterize the charge transfer. Indeed, the Blöchl ion net charges of the bulk phase (see Chapter 4) were significantly lower than the NPA ion charges of isolated ion pairs (see Chapter 3). For direct comparison, the Blöchl charges were also calculated for MMIM Cl ion pairs [38, 83, 84] and found to be at around 0.7 e instead of about 0.8 e as in Bader analysis [84] or slightly above 0.8 as in NPA (see Chapter 3, Table 3.1). In contrast, the Wannier analysis which was conducted also for the bulk phase did not allow the discussion of reduced charges as the Wannier centers, the centers of charge of Wannier orbitals, remained localized in the original molecule. However, in strong hydrogen bonds, the Wannier orbitals were delocalized onto two molecules what could be interpreted as a partial charge transport. In this way, the Wannier orbitals themselves reproduced intermolecular charge transfer found by other methods as Bader or NPA. For the statistical evaluation of dipole moments, the Wannier centers were considered and these were only shifted by the possible delocalization of the Wannier orbitals. As a consequence, the molecules appeared strongly polarized. In this sense, the broad dipole moment distribution found was the product of a polarization which included charge transfer effects.
In summary, the *ab-initio* studies proposed that charge transfer was common in all

phases of ILs. Furthermore, there was experimental evidence for the charge transfer in the liquid phase [44, 46, 122, 215]. For crystalline MMIM methylsulfate, a reduced cation net charge of 0.74 e was found by high resolution X-ray diffraction and a Bader analysis. [270] Hence in ionic liquids, both charge transfer and polarization were detected on the *ab-initio* scale which seemed important for the description of ILs in *e.g.* electrochemical applications or force field development.
More than the ion net charges, the dipole moment gave an insight onto the electronic structures of the ions as it depended on the charge distribution. In principle, also atomistic partial charge distributions, electronic orbitals, or polarization tensors could be considered. However, the dipole moment describes the molecular charge distribution as a single vector and enables a convenient statistical analysis. Indeed, the large width of the distributions found in Chapter 4 for several ILs and also before for MMIM Cl [94, 120, 121] showed that the molecular electrostatic properties varied strongly as was also seen in the large standard deviations of the ion net charges and each single atomic partial charge obtained by the Blöchl analysis. About 50 % of the width of these dipole moment distributions can be attributed to electronic polarization including charge transfer, the other 50 % to vibrational and rotational degrees of freedom (see Chapter 4.5 and Ref. [120]). The dipole moment distributions found in the liquid phase were intrinsic to the liquid phase and seemed to capture the subtle cooperative effects of the liquid phase as the dipole moment distribution of an isolated ion pair in the gas phase was rather different from the one of the liquid phase. Until now, an AIMD study is the most convenient way to give insight into these processes in the bulk phase.
However, the electrostatic properties of ions in the liquid phase were shown to be very local (see Chapter 4.3.2 and Refs. [83, 119, 121]) as *e.g.* the dipole moment distributions were independent of the system size. The interplay of high fluctuations and locality was consistent with the picture of ion cages. In this picture, an ion and its closest neighbors stay together for a rather long time period of several ps. A specific conformation of the central ion and of one of these neighbors ions, such as a hydrogen bond, has a much shorter lifetime. Indeed, about 50 % of the dynamics are due to this mutual sub-ps equilibration of counter ions. [14,107] For such relaxation, the ions' centers of mass do not have to move far, rotations of ion parts account for a lot of the configuration sampling. As the electronic structure equilibrates instantaneously to the atomic positions, it is mostly dominated by the relaxation processes of the ions in ion cages. Thus, the locality in time found for the molecular electrostatic properties seemed connected to the locality in space. Furthermore, the high fluctuations together with the locality are consistent with the experimental observation that ILs behaved as super-dissociating solvents for solute salts. [271] This so-called "true ionic liquid effect" [271] means that the dissociation of a solute salt in an IL has no activation barrier, *i.e.* $E_A = 0$. This changes the reaction order of chemical reactions in which charged states are involved. [271] The high polarity, the strong sensitivity to the closest neighbors, might explain why ILs mix well with polar solutes as water, SO_2, or CO_2. The electronic structure of the ions and, possibly, also the liquid structure adapt in such a way that the interaction between the ions and the solutes is optimal. Even though Coulomb interaction had a dominant influence, a long range order was not observed. That might be partially due to the strong electrostatic screening, but also to the influence of other interactions, steric constraints, and entropy. Due to the

high locality, box size dependencies of the electrostatic properties were not obtained. Hydrogen bonding was shown to be present in all cases and to impact the structural ordering as well as the electronic structure of the ions (see Chapters 3, 4, and 5). Even though intuitively, an enforcement and higher rigidity of the liquid structure would be expected, directional hydrogen bonds were suggested to lower the viscosity due to the preformation of ion pairs. [41, 42] The interaction between the preformed ion pairs was proposed to be reduced and, as a consequence, the intermolecular interactions in the liquid. By these intermolecular bonds, a certain short-range order was introduced, but a long-range order was not found. Any long-range order would be disturbed by the irregular shape of the ions which are rather bulky. The ions cannot pack tightly and periodic as in simple salts. A regular orientation of the ions is hindered by the many possible intramolecular and intermolecular conformations. As a consequence, crystallization is hindered and many ILs can be undercooled easily. [272] Hence, the entropy effect is more decisive than for simple salts. Further for BMIM ILs, the amphilic character of the cation with polar and apolar parts led to a segregation. [9, 50] The polar, charged imidazolium ring and the anion were strongly interacting *via* Coulomb and hydrogen bonding. The sidechain could not participate in such strong interactions and, thus, separated into domains in which they interacted *via* dispersion with each other. In this way, the sum of all interactions was maximized.

6.2 Implication to classical force field development

In all *ab-initio* studies (see Chapters 3 and 4 and Refs. [38, 44, 74, 83, 96, 102, 107]), a reduction of the ion net charge was found and this should be included in the force field development. On the one hand, reduced ion net charges were an implicit description of the mean polarization effect. On the other hand, they were the result of charge transfer for which strong evidence was found both in experiments and *ab-initio* calculations. Hence, in order to describe the true molecular electrostatic properties of the ions, it seemed a necessary condition that the ion charge should be reduced also in polarizable force fields to at least the amount of present charge transfer. In the setup of any force field, the two causes of charge reduction should be kept apart to achieve a physical meaningful parametrization. For this purpose, *ab-initio* prestudies with appropriate charge assignment methods might be rather helpful.
In general, the incorporation of AIMD simulations in the multiscale modeling was found to be useful and computationally affordable. First, the molecular electrostatic properties as well as spacial orientation of ions in the liquid phase were shown to differ qualitatively from these of the isolated ions, ion pairs, or small clusters in their ground state structures (compare Chapters 3, 4, and 5). Hence, to parametrize the correct properties, an *ab-initio* study of the bulk was mandatory. Second, the molecular electrostatic properties as the ion net charges or the dipole moment distribution were demonstrated to be largely insensitive to system size as well as simulation times (see Chapter 4.3.2). Thus, comparatively small and short simulations were sufficient to extract the relevant information. Furthermore, the molecular electrostatic properties seemed rather insensitive to temperature changes. That might hint at the validity of force field parameters for a whole temperature range. In experiments and classical

Table 6.1: Density ρ, self diffusion constants of the cations D^+ and of the anions D^- as well as he conductivity σ obtained by simulations with the parameters of **CLaP**, **BLFF**, and **BTFF** at $T = 425\,\mathrm{K}$.
The conducitivity was calculated with either the Nernst-Einstein (NE) equation or the Einstein-Helfand (EH) one. The estimated errors are given in parentheses (taken from Ref. [84]

		$D\,/\,10^{-5}(\,\mathrm{cm^2\ s^{-1}})$		$\sigma\,/(\,\mathrm{Sm^{-1}})$	
	$\rho\,/(\,\mathrm{kg\ m^{-3}})$	D^+	D^-	NE	EH
CLaP	1114.1(4.5)	0.02(0.00)	0.01(0.00)	0.5(0.0)	0.5(0.0)
BLFF	949.7(6.1)	1.39(0.10)	1.46(0.10)	21.4(1.0)	14.8(0.9)
BTFF	1123.3(4.7)	0.48(0.03)	0.62(0.04)	10.0(0.5)	9.7(0.6)
exp. [273]	1123.4	*n. a.*		10.7	

MD simulations, the temperature is mostly around room temperature whereas it is about 400 K in most AIMD studies to enable a faster sampling of the phase space. The tests on the temperature dependence encouraged the hypothesis that electrostatic properties derived at 400 K will resemble those at room temperature. In summary, for reliable data, small systems can be studied at elevated temperature for short times in AIMD which yields the multiscale approach computationally efficient and routinely applicable.

The multiscale approach was demonstrated on MMIM Cl and the AIMD simulation results were incorporated in the design of an improved force field based on the standard **CLaP** one introduced by Canongia Lopes and Padua. [54, 274, 275] Mainly, the partial charges were chosen to be the one of the Blöchl analysis. If all other parameters were left unchanged, the new force field **BLFF** led to a much lower density and an increased conductivity compared to the original **CLaP** one (see Table 6.1). [84] The conductivity was significantly above the experimental value. The liquid structure found resembled more the one obtained by AIMD simulations than the one based on the original force field as the radial distribution functions had lower maxima, hinting at a higher disorder. Hence, the reduced net charges seemed to cause a weaker ionic interaction and, as a consequence, a lower density and a less pronounced liquid structure. Also, as the ions interacted less strongly, they could move more freely and the conductivity was increased. By adapting only the partial charges and, thus, the Coulomb interactions, the balance of the intermolecular interactions in the force field was disturbed. This is why the accuracy of the resulting force field **BLFF** was not higher than that of the original **CLaP** one. Thus, in order to capture the interactions' balance found in the *ab-initio* study, the Lennard-Jones parameters were reparametrized iteratively [243] for the force field **BTFF**. Therefore, it was reproduce radial distribution functions obtained by the AIMD simulations. Notably, it was found that the radial distribution functions of hydrogen bonded atom pairs were necessary for a reliable parametrization **BTFF**. In this manner, a correct description of the effect of hydrogen bonding seemed decisive. For convenience, also the experimentally measured mass densities at three temperatures, needed anyway to setup the AIMD simulations, were employed as targets for **BTFF** and the only experimental input used throughout this multiscale study. The new force field **BTFF** gave not only static properties correctly, but also dynamic properties were predicted reasonably as

the electric conductivity obtained deviated less than 10 % from the experimental value (see Table 6.1). Hence, the refined force field **BTFF** based on Blöchl partial charges and optimized Lennard-Jones parameters was an improvement with regard to the original force field **CLaP**. Therefore, a dynamic property, the electric conductivity, was described correctly with a non-polarizable force field. Thus, for neat MMIM Cl, it seemed sufficient to include mean electrostatic properties to simulate bulk properties. For mixtures or at interfaces, an explicit description of polarization might be necessary. [56, 192] For instance, water was found to be depolarized close to ionic liquid molecules (see Chapter 4.6 and Refs. [124, 125]) and SO_2 had a large impact on the electrostatic properties of at least the DCA anion in EMIM DCA (see Chapter 4.6). In both cases, the intermolecular bonds seemed associated with a certain amount of charge transfer. In this regard, the question is risen if a polarizable force field can describe such intermolecular electronic interactions correctly. AIMD studies might give important reference data for the testing of the power of polarizable force fields. Additionally, they offer a powerful tool to the fundamental understanding of molecular electrostatic properties and possible intermolecular bonds in neat ionic liquids as well as mixtures.

6.3 Outlook

Whereas the principle power of the multiscale approach was demonstrated for MMIM Cl, further studies on its generality and on the transferability of obtained force field parameters are needed. The multiscale approach can be routinely applied to any IL as a clear scheme has been established. Recently, the procedure was adopted by another group. [276] Further systematic studies seem necessary to evaluate the transferability of parameters and to identify possible trends in the partial charges or in other electrostatic properties if *e.g.* the sidechain length or the anion is altered. Also, a more detailed evaluation of the improved force field is needed for many different properties which are experimentally accessible. For instance, the dielectric spectra would be of high interest as the interpretation of those from experiment is only possible in an indirect way. Regarding dielectric spectra which are studied widely, [11–13] the question could be addressed if polarizable force fields are necessary to reproduce those [277] or if a well chosen non-polarizable force field is sufficient.
Furthermore, the comparison to more accurate post HF calculations might give further insight, especially in the balance of charge transfer and polarization which are both due to electron correlation effects. In this aspect, the post HF study of ion pairs or clusters surrounded by point charges might be elucidative. By this, the locality assumption could be tested further. Also, the use of hybrid functionals or different electron density partitioning schemes as the Bader approach might complete the knowledge of molecular electrostatic properties.
Beside these conceptional issues, the AIMD based study of IL mixtures with small gas solutes might help to understand experimental data better. Such systems are studied widely as there are many promising applications. To allow for some systematic comparison, the four polar solutes H_2S, SO_2, H_2O, and CO_2 might be an appropriate choice. While all molecules consist of three atoms, only CO_2 is linear. Furthermore,

they are expected to interact differently with the ILs' ions. CO_2 and SO_2 have a different charge distribution than H_2S and H_2O. For SO_2, a specific sulfur nitrogen interaction was found in the preliminary study of the EMIM DCA SO_2 mixture (see Chapter 4.6). In H_2S, the sulfur has a negative charge unlike in SO_2 and, thus, might not form such bonds. H_2S and H_2O should behave very similarly, but H_2S is a much weaker hydrogen bond donor and acceptor. Still, the solubility of H_2S was found be high and a specific intermolecular interaction was proposed. [99] In this way, the study of IL mixtures with these four solutes may allow some further insight into the balance of the molecular interactions. When dispersive interactions shall be tested, apolar solutes as ether or propane might be suitable probes. [241] Experimentally, butane was reported to dissolve in the apolar domains consisting of long alkyl sidechains. [50] However, the DFT deficiencies in describing dispersion might hinder a reliable description of such adducts.

Appendix A

Supplementary Material

A.1 Gas phase: a reference state

Table A.1: Total single point energy $E_{\mathrm{tot,MP2}}$ in Hartree.

	$E_{\mathrm{tot,MP2}}$		$E_{\mathrm{tot,MP2}}$
hb-MMIM Cl	−764.5139	**hb**-BMIM Cl	−882.1884
st-MMIM Cl	−764.5150	**st**-BMIM Cl	−882.1880
1-EMIM SCN	−834.4351	1-BMIM SCN	−912.8827
2-EMIM SCN	−834.4337	2-BMIM SCN	−912.8797
hb-EMIM DCA	−584.0387	**hb**-BMIM DCA	−662.4934
st-EMIM DCA	−584.0446	**st**-BMIM DCA	−662.4916
		BMIM BF_4	−424.0459
		hb-BMIM 5AT	−734.9674
		st-BMIM 5AT	−734.9790
		hb-BMIM 4NI	−851.8827
		st-BMIM 4NI	−851.8930

A.2 Liquid phase: electrostatics and common properties

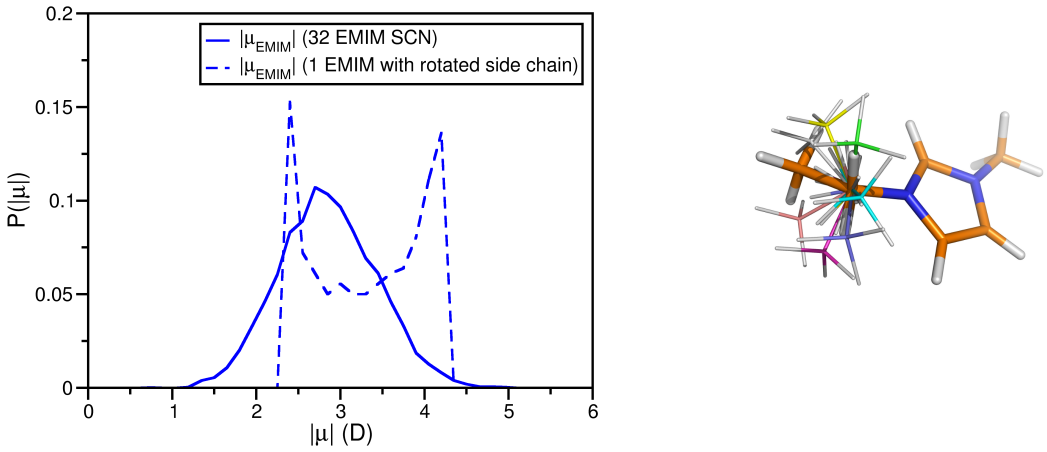

Figure A.1: Dipole moment distribution of the EMIM cation in a 30 EMIM SCN system (straight) and of one EMIM cation in a conformation found in the liquid phase. For this conformation, the positions of all other atoms and Wannier center was kept while rotating the ethyl sidechain by 360 °. In this way, the polarization of the molecule's bonds remained unaltered and the purely configurational effect on the dipole moment can be estimated.

Table A.2: Mean value and standard deviation of the dipole moment (under the assumption that the distribution are normal distributions). The values depend strongly on the chosen reference point and can only be taken qualitatively. All results discussed in Chapter 4 were found for any of the three reference points COG, COM, and COR.

IL	cation	anion
MMIM Cl	2.74 ± 0.55	0.56 ± 0.24
EMIM Cl	2.83 ± 0.67	0.56 ± 0.23
BMIM Cl	2.94 ± 0.81	0.59 ± 0.25
EMIM SCN	2.83 ± 0.60	0.81 ± 0.38
BMIM SCN	2.99 ± 0.64	0.88 ± 0.43
EMIM DCA	2.80 ± 0.58	1.40 ± 0.48
BMIM DCA	2.91 ± 0.68	1.46 ± 0.47

A.3 Liquid phase: local interactions and distinct properties

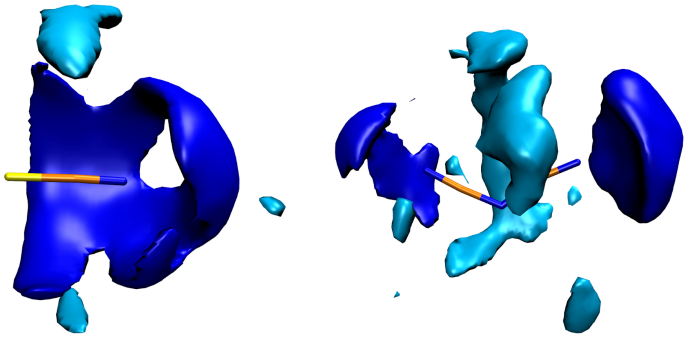

(a) BMIM SCN (b) BMIM DCA

Figure A.2: Isosurfaces of the spacial distribution functions of the cation atoms around the anion for (a) 30 BMIM SCN and (b) 30 BMIM DCA. The C^2H hydrogen distribution is shown in dark blue at an isovalue of 75 nm^{-3}, the $C^{2'}$ carbon one in light blue at an isovalue of 55 nm^{-3}. The reference plane is defined by the S, C, and N atoms for SCN and by three nitrogen atoms for DCA.

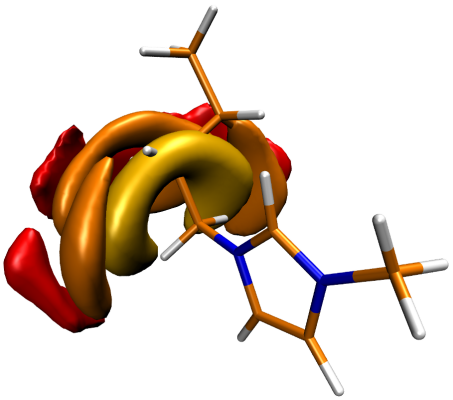

Figure A.3: Isosurface of the intramolecular spacial distribution functions of the sidechain carbon atoms for 30 BMIM SCN. Yellow denotes the $C^{2'}$ carbon atom (at an isovalue of 400 nm^{-3}), orange the $C^{3'}$ carbon atom (at an isovalue of 200 nm^{-3}), and red the $C^{4'}$ carbon atom (at an isovalue of 100 nm^{-3}). The reference plane is defined by the N-C^2-N group of the imidazolium ring (for nomenclature see Figure 1.3).

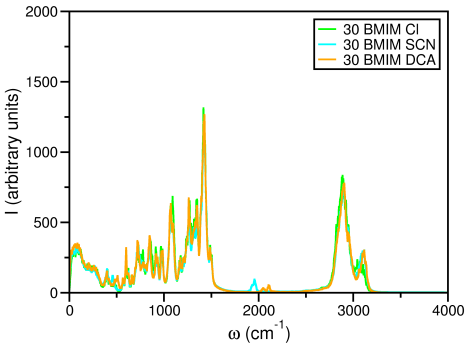

Figure A.4: Power spectra of 30 BMIM Cl, 30 BMIM SCN, and 30 BMIM DCA.

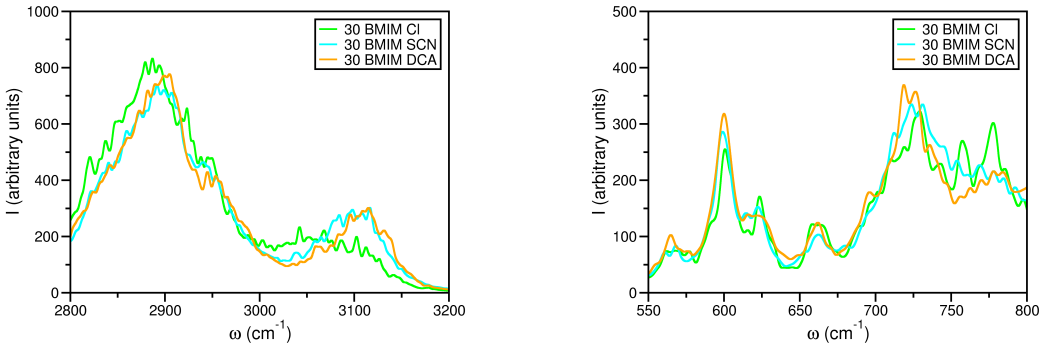

(a) 2800 cm^{-1} to 3200 cm^{-1} (b) 550 cm^{-1} to 800 cm^{-1}

Figure A.5: Power spectra of 30 BMIM Cl, 30 BMIM SCN, and 30 BMIM DCA at (a) high wavenumbers between 2800 cm^{-1} and 3200 cm^{-1} and (b) in the range between 550 cm^{-1} and 800 cm^{-1}.

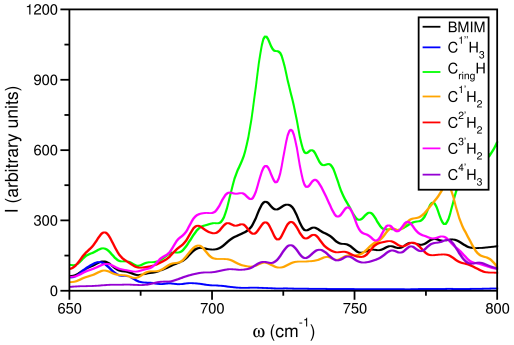

Figure A.6: Part power spectra of different groups in 30 BMIM DCA (for nomenclature see Figure 1.3) in the range between 650 cm^{-1} and 800 cm^{-1}.

Appendix B

List of abbreviations

AIMD	*ab-initio* molecular dynamics
$AlCl_3$	aluminim chloride
5AT	5-aminotetrazolate
a.u.	atomic unit
aug-cc-pVDZ	augmented correlation-consistent polarized valence double zeta function
BF_4	tetrafluoroborate
BHandHLYP	Becke half and half Lee Yang Parr (50 % HF exchange and 50 % LDA exchange)
BLYP	Becke Lee Yang Parr
BLYP-D	BLYP with Grimme dispersion correction
B3LYP	Becke three parameter Lee Yang Parr
BP86	Becke Perdew (functional from 1986)
$BP86_{DCACP}$	BP86 combined with potentials of the DCACP type
BMIM	1-butyl-3-methylimidazolium
BSSE	basis set superposition error
CC	coupled cluster
CCSD	coupled cluster with single and double excitations
CCSD(T)	CCSD with perturbative treatment of triple excitation
CCSD(T)-F12	CCSD(T) with an explicit electron correlation depending on $e^{-\alpha r_{el1\cdots el2}}$
CHELPG	charges from electrostatic potentials using a grid based method
Cl	chloride
CO_2	carbon dioxide
CPMD	Car–Parrinello molecular dynamics
COC	center of charge
COG	center of geometry
COM	center of mass
COR	geometric center of the imidazolium ring
DCA	dicyanamide
DCACP	dispersion-corrected atom-centered potential
DFT	density functional theory

e.g.	for example (latin: exempli gratiā)
EMIM	1-ethyl-3-methylimidazolium
EPR	electron paramagnetic resonance
GGA	generalized gradient approximation
hb	hydrogen bonded
HF	Hartree-Fock
H_2O	water
H_2S	hydrogen sulfide
i.e.	that is (latin: id est)
IL	ionic liquid
IR	infrared
LDA	local density approximation
MC	Monte Carlo
MD	molecular dynamics
MDEC	molecular dynamics electronic continuum
MMA	monomethylammonium
MMAN	monomethylammonium nitrate
MMIM	1,3-dimethylimidazolium
MO	molecular orbital
MP2	second order Møller-Plesset perturbation theory
4NI	4-nitroimidazolate
NMR	nuclear magnetic resonance
NBO	natural bond orbital
No.	number (latin: numero)
NO_3	nitrate
NPA	natural population analysis
PBE	Perdew Burke Ernzerhof
post HF	post Hartree-Fock
RDF	radial distribution function
Ref.	reference
RESP	restrained electrostatic potential
RI	resolution of identity
SAPT	symmetry-adapted perturbation theory
SAXS	small angle X-ray scattering
SCN	thiocyanate
SDF	spacial distribution function
SEN	shared electron number
SO_2	sulfur dioxide
st	stacked
TZVP	valence triple-ζ basis set with a polarization function
TZVPP	valence triple-ζ basis set with polarization functions
UV-vis	ultraviolett-visible

Bibliography

[1] Pádua, A. A. H.; Costa Gomes, M. F.; Canongia Lopes, J. N. *Acc. Chem. Res.* **2007,** *40,* 1087–1096.

[2] Plechkova, N. V.; Seddon, K. R. *Chem. Soc. Rev.* **2008,** *37,* 123–150.

[3] Wasserscheid, P.; Welton, T., Eds.; *Ionic Liquids in Synthesis;* Wiley-VCH: 2007.

[4] Hallett, J. P.; Welton, T. *Chem. Rev.* **2011,** *111,* 3508–3576.

[5] Werner, S.; Haumann, M.; Wasserscheid, P. *Annu. Rev. Chem. Biomol. Eng.* **2010,** *1,* 203–230.

[6] Armand, M.; Endres, F.; MacFarlane, D. R.; Ohno, H.; Scrosati, B. *Nat. Mater.* **2009,** *8,* 621–629.

[7] Pinkert, A.; Marsh, K. N.; Pang, S.; Staiger, M. P. *Chem. Rev.* **2009,** *109,* 6712–6728.

[8] Del Pópolo, M. G.; Voth, G. A. *J. Phys. Chem. B* **2004,** *108,* 1744–1752.

[9] Pogodina, N. V.; Nowak, M.; Läuger, J.; Klein, C. O.; Wilhelm, M.; Friedrich, C. *J. Rheol.* **2011,** *55,* 241–241.

[10] Pogodina, N. V.; Metwalli, E.; Müller-Buschbaum, P.; Wendler, K.; Lungwitz, R.; Spange, S.; Shamshina, J. L.; Rogers, R. D.; Friedrich, C. *J. Phys. Chem. Lett.* **2011,** *2,* 2571–2576.

[11] Turton, D. A.; Sonnleitner, T.; Ortner, A.; Walther, M.; Hefter, G.; Seddon, K. R.; Stana, S.; Plechkova, N. V.; Buchner, R.; Wynne, K. *Faraday Discuss.* **2012,** *154,* 145–153.

[12] Stoppa, A.; Hunger, J.; Buchner, R.; Hefter, G.; Thoman, A.; Helm, A. *J. Phys. Chem. B* **2008,** *112,* 4854–4858.

[13] Turton, D. A.; Hunger, J.; Stoppa, A.; Hefter, G.; Thoman, A.; Walther, M.; Buchner, R.; Wynne, K. *J. Am. Chem. Soc.* **2009,** *131,* 11140–11146.

[14] Shim, Y.; Duan, J.; Choi, M. Y.; Kim, H. J. *J. Chem. Phys.* **2003,** *119,* 6411.

[15] Bhargava, B. L.; Balasubramanian, S. *J. Chem. Phys.* **2005,** *123,* 144505.

[16] Schröder, C.; Hunger, J.; Stoppa, A.; Buchner, R.; Steinhauser, O. *J. Chem. Phys.* **2008,** *129,* 184501.

[17] Tsuzuki, S.; Shinoda, W.; Saito, H.; Mikami, M.; Tokuda, H.; Watanabe, M. *J. Phys. Chem. B* **2009,** *113,* 10641–10649.

[18] Zhao, W.; Leroy, F.; Heggen, B.; Zahn, S.; Kirchner, B.; Balasubramanian, S.; Müller-Plathe, F. *J. Am. Chem. Soc.* **2009,** *131,* 15825–15833.

[19] Sarangi, S. S.; Zhao, W.; Müller-Plathe, F.; Balasubramanian, S. *ChemPhysChem* **2010,** *11,* 2001–2010.

[20] Hunt, P. A. *Mol. Simul.* **2006,** *32,* 1–1.

[21] Maginn, E. J. *Acc. Chem. Res.* **2007,** *40,* 1200–1207.

[22] Wang, Y.; Pan, H.; Li, H.; Wang, C. *J. Phys. Chem. B* **2007,** *111,* 10461–10467.

[23] Wang, Y.; Jiang, W.; Yan, T.; Voth, G. A. *Acc. Chem. Res.* **2007,** *40,* 1193–1199.

[24] Bhargava, B. L.; Balasubramanian, S.; Klein, M. L. *Chem. Commun.* **2008,** 3339–3351.

[25] Kirchner, B. *Top. Curr. Chem.* **2009,** *290,* 213–262.

[26] Ballone, P.; Pinilla, C.; Kohanoff, J.; Del Pópolo, M. G. *J. Phys. Chem. B* **2007,** *111,* 4938–4950.

[27] Spohr, H. V.; Patey, G. N. *J. Chem. Phys.* **2009,** *130,* 104506.

[28] Spohr, H. V.; Patey, G. N. *J. Chem. Phys.* **2010,** *132,* 154504.

[29] Spohr, H. V.; Patey, G. N. *J. Chem. Phys.* **2010,** *132,* 234510.

[30] Zahn, S.; Bruns, G.; Thar, J.; Kirchner, B. *Phys. Chem. Chem. Phys.* **2008,** *10,* 6921–6924.

[31] Zahn, S.; Uhlig, F.; Thar, J.; Spickermann, C.; Kirchner, B. *Angew. Chem., Int. Ed.* **2008,** *47,* 3639–3641.

[32] Lehmann, S. B. C.; Roatsch, M.; Schöppke, M.; Kirchner, B. *Phys. Chem. Chem. Phys.* **2010,** *12,* 7473–7486.

[33] Zahn, S.; Thar, J.; Kirchner, B. *J. Chem. Phys.* **2010,** *132,* 124506.

[34] Bhargava, B.; Balasubramanian, S. *Chem. Phys. Lett.* **2006,** *417,* 486–491.

[35] Fumino, K.; Wulf, A.; Ludwig, R. *Angew. Chem., Int. Ed.* **2008,** *47,* 3830–3834.

[36] Qiao, B.; Krekeler, C.; Berger, R.; Delle Site, L.; Holm, C. *J. Phys. Chem. B* **2008,** *112,* 1743–1751.

[37] Thar, J.; Brehm, M.; Seitsonen, A. P.; Kirchner, B. *J. Phys. Chem. B* **2009,** *113,* 15129–15132.

[38] Dommert, F.; Schmidt, J.; Krekeler, C.; Zhao, Y. Y.; Berger, R.; Delle Site, L.; Holm, C. *J. Mol. Liq.* **2010,** *152,* 2–8.

[39] Costa Gomes, M. F.; Canongia Lopes, J. N.; Pádua, A. *Top. Curr. Chem.* **2009,** *290,* 161–183.

[40] Stark, A. *Top. Curr. Chem.* **2009,** *290,* 41–81.

[41] Roth, C.; Peppel, T.; Fumino, K.; Köckerling, M.; Ludwig, R. *Angew. Chem., Int. Ed.* **2010,** *49,* 10221–10224.

[42] Peppel, T.; Roth, C.; Fumino, K.; Paschek, D.; Köckerling, M.; Ludwig, R. *Angew. Chem., Int. Ed.* **2011,** *50,* 6661–6665.

[43] Tokuda, H.; Hayamizu, K.; Ishii, K.; Susan, M. A. B. H.; Watanabe, M. *J. Phys. Chem. B* **2005,** *109,* 6103–6110.

[44] Cremer, T.; Kolbeck, C.; Lovelock, K. R. J.; Paape, N.; Wölfel, R.; Schulz, P. S.; Wasserscheid, P.; Weber, H.; Thar, J.; Kirchner, B.; Maier, F.; Steinrück, H.-P. *Chem. Eur. J.* **2010,** *16,* 9018–9033.

[45] Wulf, A.; Fumino, K.; Ludwig, R. *Angew. Chem., Int. Ed.* **2010,** *49,* 449–453.

[46] Men, S.; Lovelock, K. R. J.; Licence, P. *Phys. Chem. Chem. Phys.* **2011,** *13,* 15244–15255.

[47] Perkin, S.; Crowhurst, L.; Niedermeyer, H.; Welton, T.; Smith, A. M.; Gosvami, N. N. *Chem. Commun.* **2011,** *47,* 6572–6572.

[48] Tsuzuki, S.; Tokuda, H.; Mikami, M. *Phys. Chem. Chem. Phys.* **2007,** *9,* 4780–4780.

[49] Leys, J.; Rajesh, R. N.; Menon, P. C.; Glorieux, C.; Longuemart, S.; Nockemann, P.; Pellens, M.; Binnemans, K. *J. Chem. Phys.* **2010,** *133,* 034503.

[50] Costa Gomes, M. F.; Pison, L.; Pensado, A. S.; Pádua, A. A. H. *Faraday Disc.* **2012,** *154,* 41–52.

[51] Schröder, C.; Haberler, M.; Steinhauser, O. *J. Chem. Phys.* **2008,** *128,* 1817–1821.

[52] Weingärtner, H.; Sasisanker, P.; Daguenet, C.; Dyson, P. J.; Krossing, I.; Slattery, J. M.; Schubert, T. *J. Phys. Chem. B* **2007,** *111,* 4775–4780.

[53] Morrow, T. I.; Maginn, E. J. *J. Phys. Chem. B* **2002,** *106,* 12807–12813.

[54] Canongia Lopes, J. N.; Deschamps, J.; Pádua, A. A. H. *J. Phys. Chem. B* **2004,** *108,* 2038–2047.

[55] Yan, T.; Burnham, C. J.; Del Pópolo, M. G.; Voth, G. A. *J. Phys. Chem. B* **2004,** *108,* 11877–11881.

[56] Yan, T.; Li, S.; Jiang, W.; Gao, X.; Xiang, B.; Voth, G. A. *J. Phys. Chem. B* **2006,** *110,* 1800–1806.

[57] Bagno, A.; D'Amico, F.; Saielli, G. *J. Mol. Liq.* **2007,** *131-132,* 17–23.

[58] Bhargava, B. L.; Balasubramanian, S. *J. Chem. Phys.* **2007,** *127,* 114510.

[59] Köddermann, T.; Paschek, D.; Ludwig, R. *ChemPhysChem* **2007,** *8,* 2464–2470.

[60] Lynden-Bell, R. M.; Del Pópolo, M. G.; Youngs, T. G. A.; Kohanoff, J.; Hanke, C. G.; Harper, J. B.; Pinilla, C. C. *Acc. Chem. Res.* **2007,** *40,* 1138–1145.

[61] Zhao, W.; Eslami, H.; Cavalcanti, W. L.; Müller-Plathe, F. *Z. Phys. Chem.* **2007,** *221,* 1647-1662.

[62] Schröder, C.; Steinhauser, O. *J. Chem. Phys.* **2008,** *128,* 224503–224507.

[63] Youngs, T. G. A.; Hardacre, C. *ChemPhysChem* **2008,** *9,* 1548–1558.

[64] Borodin, O. *J. Phys. Chem. B* **2009,** *113,* 12353–12357.

[65] Chang, T. M.; Dang, L. X. *J. Phys. Chem. A* **2009,** *113,* 2127–2135.

[66] Lopes, P.; Roux, B.; MacKerell, A. *Theor. Chem. Acc.* **2009,** *124,* 11–28.

[67] Lynden-Bell, R. M.; Youngs, T. G. A. *J. Phys.: Condens. Matter* **2009,** *21,* 424120.

[68] Aoun, B.; Gonzalez, M. A.; Ollivier, J.; Russina, M.; Izaola, Z.; Price, D. L.; Saboungi, M.-L. *J. Phys. Chem. Lett.* **2010,** *1,* 2503–2507.

[69] Bedrov, D.; Borodin, O.; Li, Z.; Smith, G. D. *J. Phys. Chem. B* **2010,** *114,* 4984–4997.

[70] Kerlé, D.; Ludwig, R.; Geiger, A.; Paschek, D. *J. Phys. Chem. B* **2009,** *113,* 12727–12735.

[71] Liu, Z.; Chen, T.; Bell, A. T.; Smit, B. *J. Phys. Chem. B* **2010,** *114,* 10692–10692.

[72] Lynden-Bell, R. M. *Phys. Chem. Chem. Phys.* **2010,** *12,* 1733–1740.

[73] Mallik, B. S.; Siepmann, J. I. *J. Phys. Chem. B* **2010,** *114,* 12577–12584.

[74] Kohagen, M.; Brehm, M.; Thar, J.; Zhao, W.; Müller-Plathe, F.; Kirchner, B. *J. Phys. Chem. B* **2011,** *115,* 693-702.

[75] Dommert, F.; Schmidt, J.; Qiao, B.; Zhao, Y.; Krekeler, C.; Delle Site, L.; Berger, R.; Holm, C. *J. Chem. Phys.* **2008,** *129,* 224501.

[76] Reed, A. E.; Curtiss, L. A.; Weinhold, F. *Chem. Rev.* **1988,** *88,* 899–926.

[77] Weinhold, F.; Landis, C. R. *Chem. Educ. Res. Pract. Eur.* **2001,** *2,* 91–104.

[78] Breneman, C. M.; Wiberg, K. B. *J. Comput. Chem.* **1990,** *11,* 361-373.

[79] Davidson, E. R. *J. Chem. Phys.* **1967,** *46,* 3320–3324.

[80] Hermansson, K.; Knuts, S.; Lindgren, J. *J. Chem. Phys.* **1991,** *95,* 7486–7486.

[81] Eggenberger, R.; Gerber, S.; Huber, H.; Searles, D.; Welker, M. *J. Chem. Phys.* **1992,** *97,* 5898–5898.

[82] Chirlian, L. E.; Francl, M. M. *J. Comp. Chem.* **1987,** *8,* 894–905.

[83] Schmidt, J.; Krekeler, C.; Dommert, F.; Zhao, Y.; Berger, R.; Delle Site, L.; Holm, C. *J. Phys. Chem. B* **2010,** *114,* 6150–6155.

[84] Wendler, K.; Dommert, F.; Zhao, Y. Y.; Berger, R.; Holm, C.; Delle Site, L. *Faraday Discuss.* **2012,** *154,* 111–132.

[85] Krekeler, C.; Hess, B.; Delle Site, L. *J. Chem. Phys.* **2006,** *125,* 054305.

[86] Krekeler, C.; Delle Site, L. *J. Phys.: Condens. Matter* **2007,** *19,* 192101.

[87] Krekeler, C.; Delle Site, L. *J. Chem. Phys.* **2008,** *128,* 134515.

[88] Zhao, Y. Y.; Berger, R. *unpublished work* **2009-2010,** .

[89] Werner, H.-J. *et al.* "MOLPRO, version 2010.1, a package of ab initio programs", 2008.

[90] Zahn, S.; Kirchner, B. *J. Phys. Chem. A* **2008,** *112,* 8430–8435.

[91] Ahlrichs, R.; Bär, M.; Häser, M.; Horn, H.; Kölmel, C. *Chem. Phys. Lett.* **1989,** *162,* 165–169.

[92] *CPMD;* Copyright IBM Corp 1990-2008. Copyright MPI für Festkörperforschung Stuttgart 1997-2001.: http://www.cpmd.org/,.

[93] Cohen, A. J.; Mori-Sanchez, P.; Yang, W. *Science* **2008,** *321,* 792–794.

[94] Krekeler, C.; Schmidt, J.; Zhao, Y. Y.; Qiao, B. F.; Berger, R.; Holm, C.; Delle Site, L. *J. Chem. Phys.* **2008,** *129,* 174503.

[95] Emel'yanenko, V. N.; Verevkin, S. P.; Heintz, A. *J. Am. Chem. Soc.* **2007,** *129,* 3930–3937.

[96] Hunt, P. A.; Kirchner, B.; Welton, T. *Chem.–Eur. J.* **2006,** *12,* 6762–6775.

[97] Hunt, P. A.; Gould, I. R. *J. Phys. Chem. A* **2006,** *110,* 2269–2282.

[98] Nockemann, P.; Thijs, B.; Driesen, K.; Janssen, C. R.; Van Hecke, K.; Van Meervelt, L.; Kossmann, S.; Kirchner, B.; Binnemans, K. *J. Phys. Chem. B* **2007,** *111,* 5254–5263.

[99] Pomelli, C. S.; Chiappe, C.; Vidis, A.; Laurenczy, G.; Dyson, P. J. *J. Phys. Chem. B* **2007,** *111,* 13014–13019.

[100] Wang, Y.; Li, H.; Han, S. *J. Chem. Phys.* **2005,** *123,* 174501.

[101] Wang, Y.; Li, H.; Han, S. *J. Phys. Chem. B* **2006,** *110,* 24646–24651.

[102] Kossmann, S.; Thar, J.; Kirchner, B.; Hunt, P. A.; Welton, T. *J. Chem. Phys.* **2006,** *124,* 174506.

[103] Bhargava, B.; Balasubramanian, S. *Chem. Phys. Lett.* **2007,** *444,* 242–246.

[104] Izgorodina, E. I.; Bernard, U. L.; MacFarlane, D. R. *J. Phys. Chem. A* **2009,** *113,* 7064–7072.

[105] Tsuzuki, S.; Tokuda, H.; Hayamizu, K.; Watanabe, M. *J. Phys. Chem. B* **2005,** *109,* 16474–16481.

[106] Kim, K.; Jordan, K. D. *J. Phys. Chem.* **1994,** *98,* 10089–10094.

[107] Buhl, M.; Chaumont, A.; Schurhammer, R.; Wipff, G. *J. Phys. Chem. B* **2005,** *109,* 18591–18599.

[108] Del Pópolo, M. G.; Pinilla, C.; Ballone, P. *J. Chem. Phys.* **2007,** *126,* 144705.

[109] Bernard, U. L.; Izgorodina, E. I.; MacFarlane, D. R. *J. Phys. Chem. C* **2011,** *114,* 20472–20478.

[110] Becke, A. D. *Phys. Rev. A* **1988,** *38,* 3098–3098.

[111] Lee, C.; Yang, W.; Parr, R. G. *Phys. Rev. B* **1988,** *37,* 785–789.

[112] Grimme, S. *J. Comput. Chem.* **2004,** *25,* 1463–1473.

[113] Grimme, S. *J. Comput. Chem.* **2006,** *27,* 1787–1799.

[114] Grimme, S.; Antony, J.; Ehrlich, S.; Krieg, H. *J. Chem. Phys.* **2010,** *132,* 154104.

[115] Perdew, J. P. *Phys. Rev. B* **1986,** *33,* 8822–8822.

[116] Lin, I.-C.; Coutinho-Neto, M. D.; Felsenheimer, C.; von Lilienfeld, O. A.; Tavernelli, I.; Röthlisberger, U. *Phys. Rev. B* **2007,** *75,* 205131–205131.

[117] Lin, I.-C.; Röthlisberger, U. *Phys. Chem. Chem. Phys.* **2008,** *10,* 2730–2730.

[118] Kohanoff, J.; Pinilla, C.; Youngs, T. G. A.; Artacho, E.; Soler, J. M. *J. Chem. Phys.* **2011,** *135,* 154505.

[119] Del Pópolo, M. G.; Lynden-Bell, R. M.; Kohanoff, J. *J. Phys. Chem. B* **2005,** *109,* 5895–5902.

[120] Prado, C. E. R.; Del Pópolo, M. G.; Youngs, T. G. A.; Kohanoff, J.; Lynden-Bell, R. M. *Mol. Phys.* **2006,** *104,* 2477–2483.

[121] Krekeler, C.; Dommert, F.; Schmidt, J.; Zhao, Y. Y.; Holm, C.; Berger, R.; Delle Site, L. *Phys. Chem. Chem. Phys.* **2010,** *12,* 1817–1821.

[122] Bagno, A.; D'Amico, F.; Saielli, G. *ChemPhysChem* **2007,** *8,* 873–881.

[123] Ghatee, M. H.; Ansari, Y. *J. Chem. Phys.* **2007,** *126,* 154502.

[124] Spickermann, C.; Thar, J.; Lehmann, S. B. C.; Zahn, S.; Hunger, J.; Buchner, R.; Hunt, P. A.; Welton, T.; Kirchner, B. *J. Chem. Phys.* **2008,** *129,* 104505.

[125] Zahn, S.; Wendler, K.; Delle Site, L.; Kirchner, B. *Phys. Chem. Chem. Phys.* **2011,** *13,* 15083–15093.

[126] Kirchner, B.; Seitsonen, A. P. *Inorg. Chem.* **2007,** *46,* 2751–2754.

[127] Born, M.; Oppenheimer, R. *Annalen der Physik* **1927,** *389,* 457–484.

[128] Levine, I. N. *Quantum Chemistry;* Prentice Hall: 1999.

[129] Parr, R. G.; Yang, W.; Weitao, Y. *Density-functinal theory of atoms and molecules;* Oxford University Press: 1994.

[130] Koch, W.; Holthausen, M. C. *A chemist's guide to density functional theory;* Wiley-VCH: 2001.

[131] Young, D. *Computational Chemistry - a practical guide for Applying Techniques to Real World Problems;* Wiley-VCH: 2001.

[132] Cook, D. B. *Handbook of Computational Quantum Chemistry;* Oxford University Press: 1998.

[133] Helgaker, T.; Jorgensen, P.; Olsen, J. *Molecular Electronic-Structure Theory;* John Wiley & Sons: 2000.

[134] Gauss, J. *Encyclopedia of Computational Chemistry (Coupled-cluster theory);* John Wiley & Sons: 1998.

[135] Hohenberg, P.; Kohn, W. *Phys. Rev* **1964,** *136,* B864-B871.

[136] Levy, M. *Phys. Rev. A* **1982,** *26,* 1200–1208.

[137] Lieb, E. *Int. J. Quantum Chem.* **1983,** *24,* 243–277.

[138] Cohen, M. H.; Wasserman, A. *Phys. Rev. A* **2005,** *71,* 032515–032515.

[139] Kohn, W.; Sham, L. J. *Phys. Rev.* **1965,** *140,* A1133–A1138.

[140] Ceperley, D. M.; Alder, B. J. *Phys. Rev. Lett.* **1980,** *45,* 566–569.

[141] Becke, A. D. *J. Chem. Phys.* **1993,** *98,* 1372–1372.

[142] Perdew, J. P.; Burke, K.; Ernzerhof, M. *Phys. Rev. Lett.* **1996,** *77,* 3865–3865.

[143] Perdew, J. P.; Zunger, A. *Phys. Rev. B* **1981,** *23,* 5048–5079.

[144] von Lilienfeld, O. A.; Tavernelli, I.; Röthlisberger, U.; Sebastiani, D. *Phys. Rev. Lett.* **2004,** *93,* 153004–153004.

[145] CPMD-consortium,, Ed.; *CPMD - Manual for version 3.13.2;* 2008.

[146] Wannier, G. H. *Phys. Rev.* **1937,** *52,* 191–197.

[147] Kohn, W. *Phys. Rev.* **1959,** *115,* 809–821.

[148] des Cloizeaux, J. *Phys. Rev.* **1963,** *129,* 554–566.

[149] Marzari, N.; Vanderbilt, D. *Phys. Rev. B* **1997,** *56,* 12847–12847.

[150] Marzari, N.; Souza, I.; Vanderbilt, D. *Psi-K Scient. Highlight of the Month* **2003,** *57,* 129–168.

[151] Silvestrelli, P. L.; Parrinello, M. *Phys. Rev. Lett.* **1999,** *82,* 3308–3311.

[152] Bader, R. *Atoms in Molecules: A Quantum Theory;* Oxford University Press: 1990.

[153] Sanville, E.; Kenny, S. D.; Smith, R.; Henkelman, G. *J. Comput. Chem.* **2007,** *28,* 899–908.

[154] Delle Site, L. *Mol. Simul.* **2001,** *26,* 217–235.

[155] Blöchl, P. E. *J. Chem. Phys.* **1995,** *103,* 7422.

[156] Mulliken, R. S. *J. Chem. Phys.* **1955,** *23,* 1833–1840.

[157] Foster, J. P.; Weinhold, F. *J. Am. Chem. Soc.* **1980,** *102,* 7211–7218.

[158] Reed, A. E.; Weinhold, F. *J. Chem. Phys.* **1983,** *78,* 4066–4073.

[159] Weinhold, F., Ed.; *NBO 5.0 Program Manual;* University of Wisconsin: 1996.

[160] Roby, K. R. *Mol. Phys.* **1974,** *27,* 81–104.

[161] Heinzmann, R.; Ahlrichs, R. *Theor. Chim. Acta* **1976,** *42,* 33–45.

[162] Ehrhardt, C.; Ahlrichs, R. *Theor. Chim. Acta* **1985,** *68,* 231–245.

[163] Reiher, M.; Sellmann, D.; Hess, B. A. *Theor. Chem. Acc.* **2001,** *106,* 379-392.

[164] Reiher, M.; Kirchner, B. *J. Phys. Chem. A* **2003,** *107,* 4141–4146.

[165] Thar, J. "Investigations of Hydrogen Bonds in Supermolecular Host-Guest Complexes", Master's thesis, Friedrich-Wilhelms-University Bonn, 2005.

[166] Thar, J.; Kirchner, B. *J. Phys. Chem. A* **2006,** *110,* 4229-4237.

[167] Kirchner, B.; Spickermann, C.; Reckien, W.; Schaley, C. A. *J. Am. Chem. Soc.* **2010,** *132,* 484–494.

[168] Wendler, K.; Thar, J.; Zahn, S.; Kirchner, B. *J. Phys. Chem. A* **2010,** *114,* 9529–9536.

[169] Car, R.; Parrinello, M. *Phys. Rev. Lett.* **1985,** *55,* 2471.

[170] Nosé, S. *J. Chem. Phys.* **1984,** *81,* 511.

[171] Hoover, W. G. *Phys. Rev. A* **1985,** *31,* 1695–1695.

[172] Frenkel, D.; Smit, B. *Understanding Molecular Simulation, Second Edition: From Algorithms to Applications;* Academic Press: 2001.

[173] Fumino, K.; Wulf, A.; Ludwig, R. *Angew. Chem., Int. Ed.* **2008,** *47,* 8731–8734.

[174] Fumino, K.; Wulf, A.; Ludwig, R. *Angew. Chem., Int. Ed.* **2009,** *48,* 3184–3186.

[175] Angenendt, K.; Johansson, P. *J. Phys. Chem. C* **2010,** *114,* 20577–20582.

[176] *TURBOMOLE V6.2 2010;* a development of University of Karlsruhe and Forschungszentrum Karlsruhe GmbH, 1989-2007, TURBOMOLE GmbH, since 2007; available from http://www.turbomole.com.:.

[177] Weigend, F.; Häser, M. *Theor. Chem. Acc.* **1997,** *97,* 331–340.

[178] Weigend, F.; Häser, M.; Patzelt, H.; Ahlrichs, R. *Chem. Phys. Lett.* **1998,** *294,* 143–152.

[179] Hättig, C. *J. Chem. Phys.* **2003,** *118,* 7751–7761.

[180] Schäfer, A.; Huber, C.; Ahlrichs, R. *J. Chem Phys.* **1994,** *100,* 5829–5835.

[181] Weigend, F.; Ahlrichs, R. *Phys. Chem. Chem. Phys.* **2005,** *7,* 3297–3305.

[182] Boys, S. F.; Bernardi, F. *Mol. Phys.* **1970,** *19,* 553-566.

[183] Laaksonen, L. *J. Mol. Graphics* **1992,** *10,* 33–34.

[184] Brehm, M.; Kirchner, B. *J. Chem. Inf. Model.* **2011,** *51,* 2007–2023.

[185] Bernard, U. L.; Izgorodina, E. I.; MacFarlane, D. R. *J. Phys. Chem. C* **2010,** *114,* 20472–20478.

[186] Hunt, P. A. *J. Phys. Chem. B* **2007,** *111,* 4844–4853.

[187] Steiner, T. *Angew. Chem., Int. Ed.* **2002,** *41,* 48–76.

[188] Rowland, R. S.; Taylor, R. *J. Phys. Chem.* **1996,** *100,* 7384–7391.

[189] Bondi, A. *J. Phys. Chem.* **1964,** *68,* 441–451.

[190] Paulechka, Y. U.; Kabo, G. J.; Blokhin, A. V.; Vydrov, O. A.; Magee, J. W.; Frenkel, M. *J. Chem. Eng. Data* **2003,** *48,* 457–462.

[191] Valderrama, J. O.; Robles, P. A. *Industrial & Engineering Chemistry Research* **2007,** *46,* 1338–1344.

[192] Maginn, E. J. *J. Phys.: Condens. Matter* **2009,** *21,* 373101–373101.

[193] Rai, N.; Maginn, E. J. *Faraday Disc.* **2012,** *154,* 53–69.

[194] Köddermann, T.; Wertz, C.; Heintz, A.; Ludwig, R. *ChemPhysChem* **2006,** *7,* 1944–1949.

[195] Del Pópolo, M. G.; Kohanoff, J.; Lynden-Bell, R. M.; Pinilla, C. *Acc. Chem. Res.* **2007,** *40,* 1156–1164.

[196] Borodin, O.; Smith, G. D. *J. Phys. Chem. B* **2006,** *110,* 11481–11490.

[197] Yan, T.; Wang, Y.; Knox, C. *J. Phys. Chem. B* **2010,** *114,* 6905–6921.

[198] Dommert, F.; Holm, C. *unpublished work* **2009–2011,** .

[199] Berghold, G.; Mundy, C. J.; Romero, A. H.; Hutter, J.; Parrinello, M. *Phys. Rev. B* **2000,** *61,* 10040–10040.

[200] Silvestrelli, P. L.; Bernasconi, M.; Parrinello, M. *Chem. Phys. Lett.* **1997,** *277,* 478–482.

[201] Silvestrelli, P. L.; Marzari, N.; Vanderbilt, D.; Parrinello, M. *Solid State Comm.* **1998,** *107,* 7–11.

[202] Kirchner, B.; Hutter, J. *J. Chem. Phys.* **2004,** *121,* 5133–5142.

[203] *CP2K;* 2000-2008 `http://cp2k.berlios.de`.

[204] VandeVondele, J.; Krack, M.; Mohamed, F.; Parrinello, M.; Chassaing, T.; Hutter, J. *Comput. Phys. Commun.* **2005,** *167,* 103–128.

[205] Goedecker, S.; Teter, M.; Hutter, J. *Phys. Rev. B* **1996,** *54,* 1703–1703.

[206] Hartwigsen, C.; Goedecker, S.; Hutter, J. *Phys. Rev. B* **1998,** *58,* 3641–3641.

[207] Frisch, M. J. *et al. Gaussian09, Revision B.01;* Gaussian, Inc.: Wallingford, CT, 2010.

[208] Sieffert, N.; Wipff, G. *J. Phys. Chem. B* **2006,** *110,* 13076–13085.

[209] Kubo, R.; Toda, M.; Hashitsume, N. *Statistical Physics II;* volume 31 of *Springer Series in Solid State Science* Springer-Verlag: 1978.

[210] Leontyev, I. V.; Stuchebrukhov, A. A. *J. Chem. Phys.* **2009,** *130,* 085102.

[211] Leontyev, I. V.; Stuchebrukhov, A. A. *J. Chem. Theo. Comp.* **2010,** *6,* 3153–3161.

[212] Fröba, A. P.; Kremer, H.; Leipertz, A. *J. Phys. Chem. B* **2008,** *112,* 12420–12430.

[213] Kuang, Q.; Zhang, J.; Wang, Z. *J. Phys. Chem. B* **2007,** *111,* 9858–9863.

[214] Freire, M. G.; Teles, A. R. R.; Rocha, M. A. A.; Schröder, B.; Neves, C. M. S. S.; Carvalho, P. J.; Evtuguin, D. V.; Santos, L. M. N. B. F.; Coutinho, J. A. P. *J. Chem. Eng. Data* **2011,** –.

[215] Hurisso, B. B.; Lovelock, K. R. J.; Licence, P. *Phys. Chem. Chem. Phys.* **2011,** *13,* 17737–17748.

[216] Kobrak, M. N. The Chemical Environment of Ionic Liquids: Links Between Liquid Structure, Dynamics, and Solvation. In *Adv. Chem. Phys.*; Rice, S. A., Ed.; 2008.

[217] Kobrak, M. N.; Sandalow, N. An Electrostatic Interpretation of Structure-Property Relationships in Ionic Liquids. In *Proceedings- Electrochemical Society*, Vol. 24; Mantz, R. A., Ed.; 2004.

[218] Kobrak, M. N.; Li, H. *Phys. Chem. Chem. Phys.* **2010,** *12,* 1922–1932.

[219] Méndez-Morales, T.; Carrete, J.; Cabeza, O.; Gallego, L. J.; Varela, L. M. *J. Phys. Chem. B* **2011,** *115,* 6995–7008.

[220] Kornyshev, A. A. *J. Phys. Chem. B* **2007,** *111,* 5545–5557.

[221] Fedorov, M. V.; Kornyshev, A. A. *J. Phys. Chem. B* **2008,** *112,* 11868–11872.

[222] Borodin, O. *J. Phys. Chem. B* **2009,** *113,* 11463–11478.

[223] Wendler, K.; Zahn, S.; Dommert, F.; Berger, R.; Holm, C.; Kirchner, B.; Delle Site, L. *J. Chem. Theor. Comput.* **2011,** *7,* 3040–3044.

[224] Kelkar, M. S.; Shi, W.; Maginn, E. J. *Ind. Eng. Chem. Res.* **2008,** *47,* 9115–9505.

[225] Huang, M.-M.; Weingärtner, H. *ChemPhysChem* **2008,** *9,* 2172–2173.

[226] Asumana, C.; Yu, G.; Li, X.; Zhao, J.; Liu, G.; Chen, X. *Green Chem.* **2010,** *12,* 2030–2030.

[227] Kulkarni, P. S.; Afonso, C. A. M. *Green Chem.* **2010,** *12,* 1139–1139.

[228] Karadas, F.; Atilhan, M.; Aparicio, S. *Energy & Fuels* **2010,** *24,* 5817–5828.

[229] Barrosse-Antle, L. E.; Hardacre, C.; Compton, R. G. *J. Phys. Chem. B* **2009,** *113,* 1007–1011.

[230] Huang, J.; Riisager, A.; Wasserscheid, P.; Fehrmann, R. *Chem. Commun.* **2006,** 4027–4027.

[231] Huang, J.; Riisager, A.; Berg, R. W.; Fehrmann, R. *J. Mol. Catal. A: Chem.* **2008,** *279,* 170–176.

[232] Lee, J. W.; Shin, J. Y.; Chun, Y. S.; Jang, H. B.; Song, C. E.; Lee, S.-g. *Acc. Chem. Res.* **2010,** *43,* 985–994.

[233] Ren, S.; Hou, Y.; Wu, W.; Liu, Q.; Xiao, Y.; Chen, X. *J. Phys. Chem. B* **2010,** *114,* 2175–2179.

[234] Siqueira, L. J. A.; Ando, R. A.; Bazito, F. F. C.; Torresi, R. M.; Santos, P. S.; Ribeiro, M. C. C. *J. Phys. Chem. B* **2008,** *112,* 6430–6435.

[235] Carvalho, P. J.; Coutinho, J. A. P. *Energy & Fuels* **2010,** *24,* 6662–6666.

[236] Shiflett, M. B.; Yokozeki, A. *Industrial & Engineering Chemistry Research* **2010,** *49,* 1370–1377.

[237] Wang, Y.; Wang, C.; Zhang, L.; Li, H. *Phys. Chem. Chem. Phys.* **2008,** *10,* 5976–5976.

[238] Prasad, B. R.; Senapati, S. *J. Phys. Chem. B* **2009,** *113,* 4739–4743.

[239] Kazarian, S. G.; Briscoe, B. J.; Welton, T. *Chem. Commun.* **2000,** 2047–2048.

[240] Shi, W.; Maginn, E. J. *J. Phys. Chem. B* **2008,** *112,* 16710–16720.

[241] Hanke, C. G.; Atamas, N. A.; Lynden-Bell, R. M. *Green Chem.* **2002,** *4,* 107–111.

[242] Hanke, C. G.; Lynden-Bell, R. M. *J. Phys. Chem. B* **2003,** *107,* 10873–10878.

[243] Dommert, F.; Wendler, K.; Delle Site, L.; Berger, R.; Holm, C. *submitted* **2011,** .

[244] Triolo, A.; Russina, O.; Bleif, H.-J.; Di Cola, E. *J. Phys. Chem. B* **2007,** *111,* 4641–4644.

[245] Xiao, D.; Rajian, J. R.; Cady, A.; Li, S.; Bartsch, R. A.; Quitevis, E. L. *J. Phys. Chem. B* **2007,** *111,* 4669–4677.

[246] Hunger, J.; Stoppa, A.; Schrdle, S.; Hefter, G.; Buchner, R. *ChemPhysChem* **2009,** *10,* 723–733.

[247] Kashyap, H. K.; Santos, C. S.; Annapureddy, H. V. R.; Murthy, N. S.; Margulis, C. J.; Jr, E. W. C. *Faraday Discuss.* **2012,** *154,* 133–143.

[248] Russina, O.; Triolo, A. *Faraday Discuss.* **2012,** *154,* 97–109.

[249] Chang, H.-C.; Jiang, J.-C.; Su, J.-C.; Chang, C.-Y.; Lin, S. H. *J. Phys. Chem. A* **2007,** *111,* 9201–9206.

[250] Nakano, H.; Yamamoto, T.; Kato, S. *J. Chem. Phys.* **2010,** *132,* 044106.

[251] Schröder, C.; Neumayr, G.; Steinhauser, O. *J. Chem. Phys.* **2009,** *130,* 194503.

[252] Neumayr, G.; Schröder, C.; Steinhauser, O. *J. Chem. Phys.* **2009,** *131,* 174509.

[253] Kiefer, J.; Fries, J.; Leipertz, A. *Appl. Spectrosc.* **2007,** *61,* 1306–1311.

[254] Tait, S.; Osteryoung, R. A. *Inorg. Chem.* **1984,** *23,* 4352–4360.

[255] Suarez, P.; Einloft, S.; Dullius, J.; de Souza, R.; Dupont, J. *J. Chim. Phys. Phys.-Chim. Biol.* **1998,** *95,* 14–14.

[256] Fujii, K.; Seki, S.; Fukuda, S.; Kanzaki, R.; Takamuku, T.; Umebayashi, Y.; Ishiguro, S.-i. *J. Phys. Chem. B* **2007,** *111,* 12829–12833.

[257] Dhumal, N. R. *Chem. Phys.* **2007,** *342,* 245–252.

[258] Kuo, I.-F. W.; Tobias, D. J. *J. Phys. Chem. A* **2002,** *106,* 10969–10976.

[259] Tangney, P.; Scandolo, S. *J. Chem. Phys.* **2002,** *116,* 14–24.

[260] Iftimie, R.; Tuckerman, M. E. *J. Chem. Phys.* **2005,** *122,* 214508–214508.

[261] Gaigeot, M. P.; Vuilleumier, R.; Sprik, M.; Borgis, D. *J. Chem. Theory Comput.* **2005,** *1,* 772–789.

[262] Wiener, N. *Acta Math.* **1930,** *55,* 117–258.

[263] Khinchin, A. *Mathematische Annalen* **1934,** *109,*.

[264] Butz, T. *Fourier Transformation for Pedestrians;* Springer Berlin Heidelberg: 2005.

[265] Sprik, M.; Hutter, J.; Parrinello, M. *J. Chem. Phys.* **1996,** *105,* 1142–1142.

[266] Koel, M. *Proc. Estonian Acad. Sci. Chem.* **2000,** *49,* 145–155.

[267] Bortnuchik, A. L.; Stepukhovich, A. D.; Rabinovich, I. S. *J. Appl. Spectrosc.* **1973,** *19,* 923–925.

[268] Lessing, J. G. V.; Fouché, K. F.; Retief, T. T. *J. Chem. Soc., Dalton Trans.* **1977,** 2024–2029.

[269] Hesse, M.; Meier, H.; Zeeh, B. *Spektroskopische Methoden in der organischen Chemie;* Thieme, Stuttgart: 2005.

[270] Beichel, W.; Yu, Y.; Dlubek, G.; Krause-Rehberg, R.; Trapp, N.; Krossing, I. *private communication* **2011,** .

[271] Hallett, J. P.; Liotta, C. L.; Ranieri, G.; Welton, T. *J. Org. Chem.* **2009,** *74,* 1864–1868.

[272] Freyland, W. *Coulombic Fluids: Bulk and Interfaces;* Springer: 2011.

[273] Fannin, A. A.; Floreani, D. A.; King, L. A.; Landers, J. S.; Piersma, B. J.; Stech, D. J.; Vaughn, R. L.; Wilkes, J. S.; L., W. J. *J. Phys. Chem.* **1984,** *88,* 2614–2621.

[274] Canongia Lopes, J. N.; Padua, A. A. H. *J. Phys. Chem. B* **2004,** *108,* 16893-16898.

[275] Canongia Lopes, J. N.; Padua, A. A. H. *J. Phys. Chem. B* **2006,** *110,* 19586-19592.

[276] Zhang, Y.; Maginn, E. J. *private communication* **2011,** .

[277] Schröder, C. *private communication* **2011,** .

Danksagung

An erster Stelle möchte ich herzlich meinem Betreuer Luigi Delle Site für sein großes Vertrauen, sein hohes Engagement und die besondere Förderung danken. Zudem gilt meinen betreuenden Professoren, Professor Kurt Kremer und Professor Jürgen Gauß, für ihre stete Unterstützung und ihre Anregungen großer Dank. Auch der Multiskalen-Gruppe um Professor Christian Holm, Florian Dommert und Professor Robert Berger danke ich für die vielen Diskussionen und die enge Zusammenarbeit. Die umfangreichen mit mir abgestimmten Auswertungen und Simulationen von Florian Dommert unterstützten den Fortschritt meiner Arbeit sehr.
Eine sehr produktive Kooperation fand mit Professor Barbara Kirchner und ihren Doktoranden Martin Brehm, Stefan Zahn, Jens Thar und Friedrich Malberg statt. Die thematische Nähe war eine ergiebige Quelle neuer Inspiration. Das von Martin Brehm entwickelte, hervorragende Programm TRAVIS ermöglichte mir die aufschlussreiche Untersuchung der Leistungsspektren und räumlichen Verteilungsfunktionen. Meine eigene Auswertungssoftware baut zudem auf einem Programm auf, das mir Jens Thar im Herbst 2009 zur Verfügung stellte. Es war mir eine große Freude, dass ich eine intensive Zusammenarbeit mit der Arbeitsgruppe Kirchner auch nach meinem Wechsel nach Mainz fortsetzen konnte.
Allgemein habe ich während der Promotion die SPP-Treffen schätzen gelernt und möchte den vielen Doktoranden, denen ich dort begegnete, und ganz besonders Daniela Kerlé und Yves Lingscheid für die gemeinsame Zeit danken.
Herzlicher Dank gilt der gesamten Arbeitsgruppe Kremer, die mir eine hervoragende Arbeitsumgebung bot. Ohne die vielen Gespräche, die enorme Hilfsbereitschaft sowie die Gemütlichkeit des K-Bar-Sofas wären die vergangenen Jahren nicht die selben gewesen. Ganz besonders danke ich Christoph Junghans für die Unterstützung bei der Eingewöhnung, Doris Kirsch für ihre Großzügigkeit und ihr Verständnis sowie Robert Klein für seine schnelle Hilfe bei aufgetretenen Computerproblemen. In den letzten zweieinhalb Jahren habe ich das Rhein-Main-Gebiet kennen und schätzen gelernt, so dass der Abschied nun schwer fällt.

Lebenslauf